LUND UNIVERSITY

InP/InAsP Quantum Discs-in-Nanowire Array Photodetectors: Design, Fabrication and Optical Performance

Jeddi, Hossein

2024

Document Version:
Publisher's PDF, also known as Version of record

Link to publication

Citation for published version (APA):
Jeddi, H. (2024). *InP/InAsP Quantum Discs-in-Nanowire Array Photodetectors: Design, Fabrication and Optical Performance*. Department of Physics, Lund University.

Total number of authors:
1

General rights
Unless other specific re-use rights are stated the following general rights apply:
Copyright and moral rights for the publications made accessible in the public portal are retained by the authors and/or other copyright owners and it is a condition of accessing publications that users recognise and abide by the legal requirements associated with these rights.
• Users may download and print one copy of any publication from the public portal for the purpose of private study or research.
• You may not further distribute the material or use it for any profit-making activity or commercial gain
• You may freely distribute the URL identifying the publication in the public portal

Read more about Creative commons licenses: https://creativecommons.org/licenses/

Take down policy
If you believe that this document breaches copyright please contact us providing details, and we will remove access to the work immediately and investigate your claim.

LUND UNIVERSITY

PO Box 117
221 00 Lund
+46 46-222 00 00

InP/InAsP Quantum Discs-in-Nanowire Array Photodetectors

Design, Fabrication and Optical Performance

HOSSEIN JEDDI
DEPARTMENT OF PHYSICS | FACULTY OF ENGINEERING | LUND UNIVERSITY

InP/InAsP Quantum Discs-in-Nanowire Array Photodetectors:
Design, Fabrication and Optical Performance

InP/InAsP Quantum Discs-in-Nanowire Array Photodetectors: Design, Fabrication and Optical Performance

Hossein Jeddi

Division of Solid State Physics
Department of Physics
Lund University

DOCTORAL DISSERTATION
by due permission of the Faculty of Engineering, Lund University, Sweden.
To be defended on 23rd of August, 2024 at 9:15 in Rydbergsalen,
for the degree of Doctor of Philosophy in Engineering.

Faculty Opponent
Dr. Eva Monroy
CEA, Grenoble, France

<table>
<tr><td>Organization
LUND UNIVERSITY</td><td>Document name
DOCTORAL DISSERTATION
Date of issue 23rd of August, 2024</td></tr>
<tr><td>Author: Hossein Jeddi</td><td>Sponsoring organization</td></tr>
<tr><td colspan="2">Title: InP/InAsP Quantum Discs-in-Nanowire Array Photodetectors: Design, Fabrication and Optical Performance</td></tr>
</table>

Abstract

This thesis focuses on design, processing and electro-optical investigations of two- and three-terminal photodetectors based on large arrays of around three million n^+-i-n^+ InP nanowires with embedded InAsP quantum heterostructures for broadband detection. The first part of the thesis work dealt with a general investigation of the room-temperature optoelectronic behavior of two-terminal photodetectors under broadband visible to near-infrared illumination, and in particular the response under selective 980 nm excitation of the 20 axially-embedded InAsP quantum discs in each of the nanowires. The photodetectors show a non-linear optical response, which we attribute to a novel photogating mechanism resulting from electrostatic feedback from trapped interface charges between the nanowire and SiO_x cap layer, similar to the gate action in a field-effect transistor. From detailed analyses of the complex charge carrier dynamics involving these traps in dark and under illumination was concluded that electrons are trapped in two interface acceptor states, located at 140 and 190 meV below the conduction band edge. The non-linear optical response was investigated at length by photocurrent measurements recorded over a wide power range. From these measurements were extracted responsivities of 250 A/W (gain 320) @ 20 nW and 0.20 A/W (gain 0.2) @ 20 mW with a detector bias of 3.5 V, in excellent agreement with the proposed two-trap model. Finally, a small signal optical AC analysis was made both experimentally and theoretically to investigate the influence of the interface traps on the detector bandwidth. While the traps limit the cut-off frequency to around 10 kHz, the maximum operating frequency of the detectors stretches into the MHz region.

In the second part of the thesis, we report on the detection of long-wavelength infrared radiation originating from intersubband transitions in the embedded quantum discs at low temperature. For this purpose, we developed a technique for depositing ultra-thin ITO top contact layers which not only improved the photon flux reaching the quantum discs, but also maintained electrical characteristics similar to those of the previously used thick ITO layers. Theoretical calculations of the optical transition matrix elements using an 8-band **k·p** simulation model along with solving drift-diffusion equations shed light on both interband and intersubband transitions. The calculations showed a possible intersubband transition around 135 meV (9.2 µm) between the ground state and first excited state in the conduction band of the discs in very good agreement with the observed experimental data. Conventionally, an out-of-plane electric field component is required for intersubband resonances in a planar quantum well. Interestingly, the intersubband signal in our photodetector was collected under normal incidence conditions which nominally only generates an in-plane electric field component. We attribute this unexpected intersubband signal to a scattering in the nanowire array which effectively creates an electric field component along the nanowires.

In the last part of the thesis, we focus on device processing and optoelectronic characterization of the first reported three-terminal phototransistors based on similar InP/InAsP nanowire/quantum discs heterostructures, now with a buried global gate-all-around contact around the i-segments of the nanowires comprising the quantum discs. Furthermore, an elaborate theoretical model of the phototransistors was developed in excellent agreement with the experimental results. In particular, we highlight a unique possibility to electrically tune the spectral sensitivity and bandwidth of the detector. The transparent ITO gate-all-around contact facilitates a radial control of the carrier concentration by more than two orders of magnitude in the nanowires and quantum discs. The transfer characteristics reveal two different transport regimes. In the subthreshold region, the photodetector operates in a diffusion mode with a distinct onset at the bandgap of InP. At larger gate biases, the phototransistor switches to a drift mode with a strong contribution from the InAsP quantum discs. Besides the unexpected spectral tunability, the detector exhibits a state-of-the art non-linear responsivity reaching 100 A/W (638 nm/20 µW) @ V_{GS}=1.0V/V_{DS}=0.5V, and a response time of the order of µs, limited by the experimental setup, in excellent agreement with the developed comprehensive real-device model.

<table>
<tr><td colspan="3">Key words: Nanowires, IR photodetector, phototransistor, QDiscs-in-Nanowire, long-wavelength infrared (LWIR), ultra-thin ITO contacts, photogating</td></tr>
<tr><td colspan="3">Classification system and/or index terms (if any)</td></tr>
<tr><td colspan="2">Supplementary bibliographical information</td><td>Language: English</td></tr>
<tr><td colspan="2">ISSN and key title</td><td>ISBN
978-91-8104-083-8 (print)
978-91-8104-084-5 (electronic)</td></tr>
<tr><td>Recipient’s notes</td><td>Number of pages 87
Security classification</td><td>Price</td></tr>
</table>

I, the undersigned, being the copyright owner of the abstract of the above-mentioned dissertation, hereby grant to all reference sources permission to publish and disseminate the abstract of the above-mentioned dissertation.

Signature … H. Jeddi … Date May 29, 2024

InP/InAsP Quantum Discs-in-Nanowire Array Photodetectors: Design, Fabrication and Optical Performance

Hossein Jeddi

Front cover:
Cross-sectional scanning electron micrograph of a fully processed, three-terminal, array photodetector. The indium phosphide nanowire is colored in red; the top contact (drain) and the gate contact are sputtered indium tin oxide, shown in green, and the SiO_x between the gate contact and the nanowire is shown in blue. The substrate is highly-doped indium phosphide which serves as the source.

Pages 1-87 © 2024, Hossein Jeddi.

Paper I © 2021, The Authors, Published by the Royal Society of Chemistry.
Paper II © 2023, The Authors, Published by the American Chemical society.
Paper III © 2024, The Authors, Published by IOP Publishing.

Division of Solid State Physics
Department of Physics
Faculty of Engineering
Lund University
SE-221 00 Lund
Sweden

ISBN 978-91-8104-083-8 (print)
ISBN 978-91-8104-084-5 (electronic)

Printed in Sweden by Media-Tryck, Lund University
Lund 2024

KLIMATKOMPENSERAT
PAPPER

ساعتی میزان آنی ساعتی موزون این
بعد از این میزان خود شو تا شوی موزون خویش
- مولانا

It's your road, and yours alone.
Others may walk it with you,
but no one can walk it for you.
-Rumi

Table of Contents

Abstract 11

Acknowledgments 13

Popular scientific summary 15

List of the papers 17

Abbreviations 19

1. Introduction 21

2. Background and motivation 23

2.1. Infrared radiation 23

2.2. Semiconductors 24

2.3. Nanostructures 27

2.3.1. Quantum wells 27

2.3.2. Nanowires 28

2.3.3. Quantum dots 29

2.4. Optical properties of semiconductors 29

2.4.1. Interband transitions in bulk semiconductors 29

2.4.2. Interband transitions in quantum wells 30

2.4.3. Intersubband transitions in quantum wells 31

2.5. Infrared photodetectors 31

2.5.1. p-n and p-i-n photodiodes 31

2.5.2. Photoconductors 34

2.5.3. HgCdTe detectors 35

2.5.4. Quantum well infrared photodetectors 35

2.5.5. Quantum dot infrared photodetectors 36

2.5.6. Type-II superlattice infrared photodetectors 36

2.5.7. Nanowire-based infrared photodetectors 37

2.6. Figures of merit of photodetectors 38

2.6.1. Responsivity 38

2.6.2. Quantum efficiency 38

2.6.3. Gain 38

2.6.4. Photogating 39

2.6.5. Response time and bandwidth 40

2.6.6. Noise equivalent power and detectivity 40

2.6.7. Dark current 40

3. Nanowire growth and device processing 41

3.1. Nanowire growth 41

3.2. Device processing 42

3.2.1. Two-terminal photoconductors 42

3.2.1.1. Deposition and etching of insulating oxide layers 44

3.2.1.2. Definition of device areas 45

3.2.1.3. Sputtering the top ITO contact 46

3.2.1.4. Definition and evaporation of bond pads 46

3.2.2. Three-terminal phototransistors 46

3.2.2.1. Deposition of insulating oxide layers 48

3.2.2.2. Sputtering the gate ITO layer 49
3.2.2.3. Definition of device areas 50
3.2.2.4. Sputtering the top ITO contact 51
3.2.2.5. Definition of the via holes 51
3.2.2.6. Definition and evaporation of bond pads 51

4. Characterization techniques 53

4.1. Probe station measurements 53

4.2. Fourier transform infrared photocurrent spectroscopy 53

4.3. I-V characterization 55

4.4. PC measurements by laser 55

5. Photogating effect in two-terminal photoconductors 57

5.1. I-V characteristics 57

5.2. Spectrally-resolved PC and responsivity 58

5.3. Power-dependent responsivity 58

5.4. Frequency response 60

6. LWIR response of two-terminal photodetectors 63

6.1. I-V characteristics 63

6.2. Spectrally-resolved responsivity 64

6.3. Electronic structure of embedded quantum discs 65

6.4. Characterization of ultra-thin ITO layers 67

7. Room-temperature GAA-phototransistors 69

7.1. I-V characterization 69

7.2. Spectrally-resolved, bias-tunable responsivity 69

7.3. Modeling results and transistor characteristics 70

7.4. Time-response measurements 72

7.5. Power-dependence 73

8. Summary and outlook 75

References 77

Appendix 85

Abstract

This thesis focuses on design, processing and electro-optical investigations of two- and three-terminal photodetectors based on large arrays of around three million n^+-i-n^+ InP nanowires with embedded InAsP quantum heterostructures for broadband detection. The first part of the thesis work dealt with a general investigation of the room-temperature optoelectronic behavior of two-terminal photodetectors under broadband visible to near-infrared illumination, and in particular the response under selective 980 nm excitation of the 20 axially-embedded InAsP quantum discs in each of the nanowires. The photodetectors show a non-linear optical response, which we attribute to a novel photogating mechanism resulting from electrostatic feedback from trapped interface charges between the nanowire and SiO_x cap layer, similar to the gate action in a field-effect transistor. From detailed analyses of the complex charge carrier dynamics involving these traps in dark and under illumination was concluded that electrons are trapped in two interface acceptor states, located at 140 and 190 meV below the conduction band edge. The non-linear optical response was investigated at length by photocurrent measurements recorded over a wide power range. From these measurements were extracted responsivities of 250 A/W (gain 320) @ 20 nW and 0.20 A/W (gain 0.2) @ 20 mW with a detector bias of 3.5 V, in excellent agreement with the proposed two-trap model. Finally, a small signal optical AC analysis was made both experimentally and theoretically to investigate the influence of the interface traps on the detector bandwidth. While the traps limit the cut-off frequency to around 10 kHz, the maximum operating frequency of the detectors stretches into the MHz region.

In the second part of the thesis, we report on the detection of long-wavelength infrared radiation originating from intersubband transitions in the embedded quantum discs at low temperature. For this purpose, we developed a technique for depositing ultra-thin ITO top contact layers which not only improved the photon flux reaching the quantum discs, but also maintained electrical characteristics similar to those of the previously used thick ITO layers. Theoretical calculations of the optical transition matrix elements using an 8-band **k·p** simulation model along with solving drift-diffusion equations shed light on both interband and intersubband transitions. The calculations showed a possible intersubband transition around 135 meV (9.2 µm) between the ground state and first excited state in the conduction band of the discs in very good agreement with the observed experimental data. Conventionally, an out-of-plane electric field component is required for intersubband resonances in a planar quantum well. Interestingly, the intersubband signal in our photodetector was collected under normal incidence conditions which nominally only generates an in-plane electric field component. We attribute this unexpected intersubband signal to a scattering in the nanowire array which effectively creates an electric field component along the nanowires.

In the last part of the thesis, we focus on device processing and optoelectronic characterization of the first reported three-terminal phototransistors based on similar InP/InAsP nanowire/quantum discs heterostructures, now with a buried global gate-all-around contact around the i-segments of the nanowires comprising the quantum discs. Furthermore, an elaborate theoretical model of the phototransistors was developed in excellent agreement with the experimental results. In particular, we highlight a unique possibility to electrically tune the spectral sensitivity and bandwidth of the detector. The transparent ITO gate-all-around contact facilitates a radial control of the carrier concentration by more than two orders of magnitude in the nanowires and quantum discs. The transfer characteristics reveal two different transport

regimes. In the subthreshold region, the photodetector operates in a diffusion mode with a distinct onset at the bandgap of InP. At larger gate biases, the phototransistor switches to a drift mode with a strong contribution from the InAsP quantum discs. Besides the unexpected spectral tunability, the detector exhibits a state-of-the art non-linear responsivity reaching 100 A/W (638 nm/20 μW) @ V_{GS}=1.0V/V_{DS}=0.5V, and a response time of the order of μs, limited by the experimental setup, in excellent agreement with the developed comprehensive real-device model.

Acknowledgments

The past five years of my life as a PhD student in Sweden have been a journey filled with ups and downs. Yet, in hindsight, embarking on this journey fills me with immense happiness, an achievement that would have been nearly impossible without the support and assistance of those around me. Therefore, I seize this opportunity to extend my deepest gratitude to those who have made this journey smoother for me.

Foremost, I express my sincere appreciation to my supervisor, Prof. Håkan Pettersson, whose guidance and support have been invaluable. His visits to the lab during measurements, impassioned discussions about the results, and unwavering patience during challenging times have not only kept me motivated but have also facilitated my daily learning and growth. Thank you, Håkan, for your support. I also extend my gratitude to my co-supervisor, Prof. Magnus Borgström, for his invaluable support and insightful discussions regarding nanowire growth and device processing throughout my thesis.

I have been fortunate to collaborate with exceptionally knowledgeable individuals. My heartfelt thanks to Amin for introducing me to the cleanroom, imparting his expertise in processing techniques, and always being available to offer assistance over the past five years. Additionally, I am grateful to Reza for his invaluable support with simulations and engaging discussions throughout my PhD journey. I extend my thanks to Kristi, Yue, and Lukas for providing me with nanowires and for the insightful discussions we shared. Special thanks to Prof. Maria Messing and Marie for their meticulous TEM characterization of the nanowires, which significantly contributed to a deeper understanding of the nanowires and quantum discs used in my thesis project. I am also grateful to Prof. Bernd Witzigmann for his invaluable theoretical calculations and simulations of the studied photodetectors. Your contributions and insights during our meetings have been immensely valuable. Additionally, I express my gratitude to Dr. Mattias Borg and Heera for the collaboration on the InSb photodetector project. It was truly a pleasure working with both of you. I also extend my sincere appreciation to Prof. Anders Mikkelsen, Prof. Heiner Linke and Vidar for the collaboration on the single nanowire communication project. Our collaboration was full of interesting ideas and meetings, and I am grateful for the opportunity to work with such a team.

To everyone at FTF—Yue, Esra, Asmita, Marie, Elham, Mehran, David, Julia, Pau, Mariia, Max, Harald, Mado, Nils, Patrik, Ruby, Sebastian, Adam and Dan—I extend my heartfelt thanks for making FTF a better place by your knowledge, kindness and friendship. I wish you all the best in your future endeavors. Also, to my close friends at FTF, Antti and Kristi, thank you for the wonderful moments we have shared over the past years. Thank you both for being there for me, for the countless conversations where I could share anything without hesitation. I hope we keep the WhatsApp group *"summer plans (7.5 credits)"* active, and that we continue to create new memories together in the future. Additionally, I extend my gratitude to the cleanroom, IT, and technical personnel—Luke, Ivan, Anders, Håkan, Alexander, Sarah, Natalia, Bengt, Evelina, Anna-Karin, Gerda, Alexandra and Alfons—for their invaluable support, which greatly facilitates our work at FTF.

To my friends outside of academia—Amin and Elena— I want to express my heartfelt appreciation for your support since my arrival in Sweden. Thank you for always being by my side. To Reza and Sara, Babak and Parisa, Mohammad and Shirin, Hassan and Sima, Shiva, Azin, Lina Ekstedt and Fatemeh, I extend my warmest gratitude for the memorable moments we have shared together. Your companionship has been a source of comfort, ensuring that I

never felt homesick. To Saeed, Hooman, and Hamed, despite the distance between us, I have always known that I can count on you. Thank you for being there whenever I needed someone to talk to, whether to share my challenges or moments of happiness.

To my friends at the IK-Dana wrestling club, discovering the club and joining you from day one in Lund has brought me immense happiness. IK-Dana has been a sanctuary where I could leave my worries behind upon entering. What began as plans to hang out and enjoy the sauna after training unexpectedly led to multiple participations in the Swedish championship, thanks to the encouraging energy you all provided. Lars, Mohammadi, and Mats—thank you for warmly welcoming me into the club and for making IK-Dana such a vibrant place for wrestlers. *Mats, your unforgettable shouts of "Hossein, 20 seconds left" during the SM final will always stay with me*. Alexander, thank you for your contagious laughter and uplifting spirit which have consistently brightened our training sessions. *I know you're determined to score a point against me, but don't worry, your moment will come!* Magnus, Justin, David, Lukas, Joakim, Timur, Daniel, and Lauri—I want to express my deepest gratitude for the countless memories we have shared over the years. Wrestling and your friendship have been a big part of my life, making every challenge more bearable. To Reza, Nasri, Mohammad, Erik and Milad—even though you have moved on from IK-Dana, I am thankful for the bonds we have formed and the continuation of our friendship and wrestling adventures in Dalby. Tom and Christoffer, I am thrilled that our friendship goes beyond wrestling. Your support and the countless great times we have shared mean a lot to me. *Let's plan more camping and canoeing trips—just not against the river this time!*

Last but certainly not least, I owe an immeasurable debt of gratitude to my parents and two sisters. Your love, encouragement, and sacrifices have been the bedrock of my journey. Your belief in me, even during the most trying times, has been a source of strength and motivation. This accomplishment is as much yours as it is mine.

Popular scientific summary

The reason that we see objects with distinct colours is the reflection of visible light from those objects. Let us take a red apple as an example. A red apple absorbs all the colors from visible light coming from the sun except red that is reflected by the apple and detected by our eyes. Visible light is only a small portion of the broad spectrum of electromagnetic waves that our eyes can detect. Other electromagnetic waves such as ultraviolet, x-ray and infrared are invisible to us.

One example of infrared light is heat emitted by objects. For instance, our body at room temperature (37 °C) emits infrared radiation with a wavelength of around 9 µm. Imagine having eyes which can detect and see infrared light as well similar to some animals, such as snakes, who can see in darkness by sensing heat. However, as we cannot see infrared light, we need specific detectors to capture and "see" those invisible waves. Historically, scientists have tried diverse ways to detect infrared light for different purposes like night vision, safety and later for complicated technologies such as telecommunication.

One clever way to detect infrared light is by using semiconductor materials, such as silicon, which have a conductivity between that of a conductor and an insulator. These materials show an increased conductivity under illumination of light waves with specific energy. To detect a broad range of wavelengths in the infrared region requires stacks of different thin semiconductor layers grown on top of each other.

Over the last two decades, scientists have drastically improved the technology for fabricating ultrathin layered composite nanomaterials for various optoelectronic applications, one of them being advanced infrared detectors. In this thesis work, I have used a specific type of nanomaterials, known as nanowires, to fabricate infrared detectors. As the name implies, a nanowire is a thin needle-like structure with a diameter of around 100 nanometer (around 500 times thinner than a strand of hair). Further technology improvements enabled scientists to fabricate nanowire-based infrared photodetectors, with enhanced performance compared to traditional detectors, owing to advantages such as higher absorption with less material and flexibility in growing different materials on top of each other.

In my PhD work, I have developed novel high-performance infrared light detectors comprising several millions of standing indium phosphide nanowires, connected in parallel as a single detector. Indium phosphide nanowires can absorb and detect visible light and some parts of the infrared light known as near-infrared light. To extend the detection range to longer wavelengths in the infrared region, ultra-thin discs (quantum discs) of indium arsenide phosphide were axially embedded along the nanowires, similar to a barcode structure. This complex nanowire/quantum discs heterostructure detector can "see" visible to short-wavelength infrared light based on optical interband transitions. Importantly, mid-wavelength to long-wavelength infrared light also can be detected with the same device provided that it is cooled down to low temperatures (below -260 °C). Here the detector signal is generated by intersubband transitions in the quantum discs. Overall, the optoelectronic properties of these detectors are remarkable. The dark current is truly low, while the photocurrent under illumination is very high due to a novel gain mechanism related to hitherto unknown charge carrier traps present in the nanowires.

In the last part of my thesis project, I added another terminal to the above-mentioned detector as a gate contact, wrapped around the nanowires similar to a transistor. This third terminal provides a unique flexibility in controlling the detector's optoelectronic characteristics. The optical detection window, optical gain and response time of the detector can all be adjusted simply by changing the bias applied to the gate contact.

I believe this thesis is a step forward toward high-performance infrared light detectors compatible with commercially viable main-stream silicon technology.

List of the papers

This thesis is based on the following three articles:

I. **Gain and bandwidth of InP nanowire array photodetectors with embedded photogated InAsP quantum discs**
Jeddi, H., Karimi, M., Witzigmann, B., Zeng, X., Hrachowina, L., Borgström, M. T., and Pettersson, H. *Nanoscale*, *13, 6227-6233 (2021).*
I carried out the I-V and spectrally-resolved photocurrent measurements jointly with my co-first author M. Karimi. I contributed to the data analysis, wrote the first draft, and completed the paper with input from the co-authors.

II. **Spectrally tunable broadband gate-all-around InAsP/InP quantum discs-in-nanowire array phototransistors with a high gain-bandwidth product**
Jeddi, H., Witzigmann, B., Adham, K., Hrachowina, L., Borgström, M. T., and Pettersson, H. *ACS Photonics, 10, 1748–1755 (2023).*
I developed the complex device processing, performed all the measurements, contributed to the data analysis and wrote the paper with input from the co-authors.

III. **Enhanced LWIR response of InP/InAsP quantum discs-in-nanowire array photodetectors by photogating and ultra-thin ITO contacts**
Jeddi, H., Adham, K., Zhao, Y., Witzigmann, B., Römer, F., Bermeo, M., Borgström, M. T., and Pettersson, H. *Nanotechnology, 35, 215206 (2024).*
I developed the device processing, performed all the measurements, contributed to the data analysis and wrote the paper with input from the co-authors.

Abbreviations

ALD	Atomic layer deposition
Al_2O_3	Aluminium oxide
AsH_3	Arsine
Au	Gold
BOE	Buffered oxide etchant
SC	Semiconductor
CVD	Chemical vapor deposition
DEZn	Diethylzinc
EDX	Energy dispersive X-ray
EHP	Electron-hole pair
FIR	Far infrared
FTIR	Fourier-transform infrared spectroscopy
GAA	Gate-all-around
H_2SO_4	Sulfuric acid
HCL	Hydrochloric acid
InAsP	Indium arsenide phosphide
InP	Indium phosphide
IR	Infrared
ITO	Indium tin oxide
KI/I_2	Potassium iodide
LED	Light-emitting diode
LWIR	Long-wavelength infrared
MBE	Molecular-beam epitaxy
MCT	HgCdTe
MOVPE	Metalorganic vapor-phase epitaxy
MOSFET	Metal-oxide-semiconductor field-effect transistor
MWIR	Mid-wavelength infrared
NIR	Near-infrared
NP	Nanoparticle
NW	Nanowire
PC	Photocurrent
PH_3	Phosphine
QD	Quantum dot
QDIP	Quantum dot infrared photodetector
QDisc	Quantum disc
QW	Quantum well
QWIP	Quantum well infrared photodetector
RIE	Reactive ion etching
SEM	Scanning electron microscope
SiO_2	Silicon dioxide
STEM	Scanning transmission electron microscopy
SWIR	Short-wavelength infrared
T2SL	Type-2 superlattice
TEM	Transmission electron microscope
TESn	Tetraethyltin
Ti	Titanium
TMA	Trimethylaluminium
TMIn	Trimethylindium
UV	Ultraviolet
UVL	Ultraviolet lithography

1. Introduction

Over the last two decades, III-V nanowires (NWs) have been studied in various optoelectronic applications because of their unique characteristics, including excellent transport properties, tunable direct bandgap, and high absorption using less material compared to their planar counterparts. Moreover, the small footprint of NWs offer lattice mismatch relaxation which has enabled the integration of NW-based devices with mainstream Si technology[1]. Transistors[2-4] based on InP, InGaAs, and InAs as well as solar cells based on InP[5] and light-emitting diodes (LEDs) based on GaAs/AlGaAs core-shell NWs on Si[6] are just a few examples.

The above-mentioned advantages of III-V NWs have also made them outstanding candidates for photodetection purposes. The tunable bandgap of these nanostructures makes it possible to cover a broad spectral range. III-V NWs have been widely used as photodetectors not only in the visible range, but also in the infrared (IR) region from near-infrared (NIR: 0.75 – 1.4 μm) to long-wavelength infrared (LWIR:8 - 15 μm)[7-11]. The development of growth techniques has enabled axial embedding of quantum heterostructures in NWs, which provides a further degree of freedom for tailored interband, and more recently demonstrated intersubband detection of IR via optical transitions involving discrete energy levels[11-13]. However, there are still challenges to overcome along the path toward reproducible, commercially-viable III-V NW-based photodetectors. For instance, it has been shown that a minor change in doping concentration during epitaxial growth of NWs can drastically affect the growth dynamics and the electrical and optical characteristics of the final devices[14-19]. Despite many efforts, control of the doping concentration during NW growth is still demanding, especially in the ternary and quaternary material systems, because of growth kinetics and solubility in the Au seed particle, and the geometrical shape of NWs and their high surface-to-volume ratio[20, 21]. The cylindrical shape of NWs provides an alternative way for tuning the carrier concentration (Fermi level) by adding a conformal gate-all-around (GAA, also referred to as wrap-gate) electrode. Several groups have reported three-terminal NW devices with gate-tunable radial carrier concentrations[22-25].

Broadband photodetectors with high responsivity in the visible to infrared (IR) regions are important elements in various applications such as optical communication, safety, environmental surveillance, industrial quality control, and medical screening[26-28]. Conventionally, Si (0.45 - 1.1 μm), Ge (0.8 - 1.8 μm) and InGaAs (0.8 - 2.6 μm) are the most popular candidates for detection of visible to short-wavelength infrared (SWIR, 1.4 - 3 μm) radiation. The LWIR range has attracted an increasing attention due to thermal emission signatures from objects and living organisms which facilitate a broad range of imaging and night vision capabilities[29, 30]. Today, the most common planar material structures for LWIR detection include HgCdTe (MCT)[31], and quantum structures including InAs/GaSb type-II superlattices[32], InGaAs/GaAs quantum wells (QWs)[33] and InAs/GaAs quantum dots (QDs)[34]. Although there have been many reports of broadband photodetectors based on low-dimensional structures, there is still a demand for developing photodetectors with a fast and sensitive (high gain-bandwidth product) photoresponse. A particularly interesting photodetector type with potentially electrically-tunable optoelectronic characteristics is the three-terminal NW phototransistor. Because processing devices with large arrays of NWs is challenging and time-consuming, all electrically gated phototransistor studies reported to date have been carried out on single NW devices[35-38]. Even though NW array GAA metal-oxide-semiconductor field-effect transistors (GAAMOSFETs) have been investigated for some time, to the best of our knowledge, no studies on related phototransistors have been reported.

This thesis reports on the outstanding optoelectronic performance demonstrated for our recently developed two-terminal photoconductors and three-terminal GAA-phototransistors. For all the devices, the optical material platform is based on large mm^2 arrays of n^+-i-n^+ InP NWs with 20 quantum discs (QDiscs) axially embedded in the i-segment of each nanowire. In two-terminal detectors, the highly doped n-type InP substrate is used as one of the contacts, while a layer of indium tin oxide (ITO) is sputtered as the top contact, connecting typically almost 3 million NWs in parallel. We have studied the temperature-dependent electrical and optical characteristics of the two-terminal photoconductors in dark and under illumination using Fourier transform infrared (FTIR) photocurrent spectroscopy[39]. Additionally, a 980 nm laser diode was used for selective excitation of the QDiscs below the bandgap of InP. The power dependent optical response of the photodetector under laser excitation shows a non-linear behavior which we attribute to a novel photogating mechanism, originating from complex photocarrier dynamics involving two acceptor trap states located at the interface between the NW and the SiO_x cap layer, in good agreement with an advanced real-device model. In addition, the effect of the traps on the bandwidth of the photodetector was investigated at length. Further in-depth characterization at low temperature was carried out to unravel the recently-discovered intriguing photoresponse in the LWIR range resulting from intersubband transitions in the embedded QDiscs. For this, special attention was first devoted to developing smooth and ultrathin (10 nm) ITO top contact layers to mitigate the strong LWIR absorption of ITO. Moreover, the electronic structure of the QDiscs, including strain and defect-induced photogating effects, and optical transition matrix elements, was calculated by an 8-band $\mathbf{k}\cdot\mathbf{p}$ simulation combined with solving drift-diffusion equations to unravel the intriguing physics behind in particular the observed narrow linewidth intersubband signal from the QDiscs.

In the three-terminal detector project, we present a report on growth, device processing, optoelectronic characterization and modeling of state-of-the-art GAA-phototransistors. The detector elements are based on arrays of vertically standing NWs similar to those in the two-terminal detectors. In addition to the substrate and top ITO contacts discussed above, a third buried ITO GAA contact to all i-segments (with QDiscs) of the NWs was implemented. We highlight a possibility to electrically tune the Fermi level in the NWs, and thereby the spectral sensitivity of the detector, and the high gain-bandwidth product.

In what follows, Chapter 2 discusses IR radiation, semiconductor materials, III-V NWs, nanostructures, optical properties of semiconductors, different types of IR photodetectors and their figures of merit, along with the motivation of this project. Chapter 3 presents a summary of the NW growth and device processing details. The key characterization techniques used in this thesis work are then discussed in Chapter 4. The results for the two-terminal photodetectors at room temperature and low temperature are discussed in Chapter 5 and Chapter 6, respectively, while the results for three-terminal photodetectors are discussed in Chapter 7. Finally, the summary and future outlook are presented in Chapter 8.

2. Background and motivation

The basic properties of IR radiation are discussed in this chapter, followed by a brief description of the fundamentals of semiconductors, III-V NWs and nanostructures. Next, state-of-the-art IR photodetectors based on different techniques and their figures of merit are introduced. Finally, the motivation for this thesis project is presented.

2.1. Infrared radiation

Infrared radiation was unknown until 1800, when William Herschel discovered it by studying the spectrum of the sun using a prism and a thermometer. He found out that the highest temperature was obtained when he held the thermometer just outside the red part of the dispersed visible spectrum, a spectral range now referred to as infrared (from the Latin word 'infra' meaning below)[40].

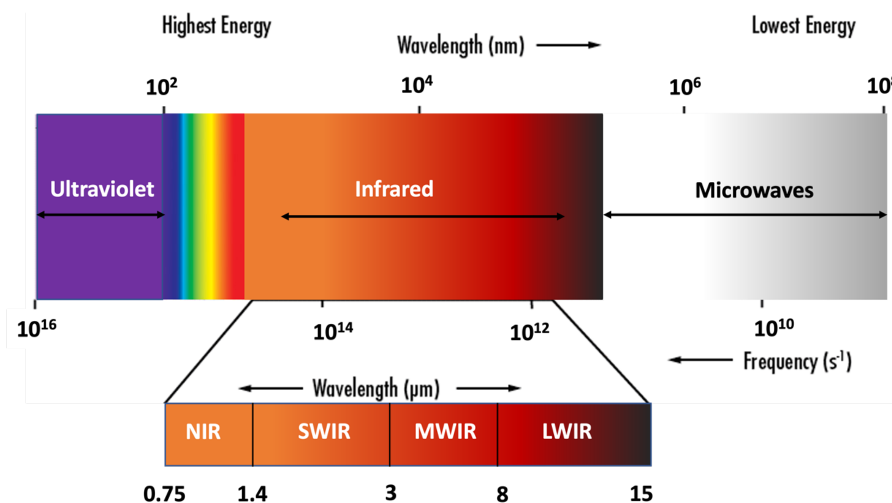

Figure 2.1: Part of the electromagnetic spectrum with a focus on the IR region.

As shown in Fig. 2.1, IR covers the region of the electromagnetic (EM) spectrum between visible light and microwaves, with a wavelength starting from 0.75 µm and stretching to 1 mm. The IR spectrum itself can be divided into five ranges according to the wavelength or energy: near-infrared (NIR) with a wavelength (energy) between 0.75 - 1.4 µm (1.65 - 0.89 eV); short-wavelength infrared (SWIR) with a wavelength (energy) between 1.4 - 3 µm (0.89 - 0.41 eV); mid-wavelength infrared (MWIR) with wavelength (energy) between 3 - 8 µm (0.41 - 0.16 eV); long-wavelength infrared (LWIR) with wavelength (energy) between 8 - 15 µm (0.16 - 0.083 eV); and far infrared (FIR) with wavelength between 15 µm - 1 mm (0.083 - 0.0012 eV)[41].

A black body is an ideal object in thermodynamic equilibrium with its environment which absorbs and emits all wavelengths (zero reflection and transmission). In 1879, Stefan discovered experimentally the relation between thermal radiation from a black body and its temperature[42]. Boltzmann derived the same relation theoretically in 1884[42]. The thermal radiation intensity, U, is given by the Stefan-Boltzmann law $U = \sigma T^4$, where T is the absolute temperature and σ is a constant ($5.67 \times 10^{-8}\, W \cdot m^{-2} \cdot K^{-4}$). Almost ten years later, Wien

proposed his famous displacement law[42] stating that the peak value of the radiation intensity occurs at a specific wavelength which has an inverse relationship with the object's temperature, $\lambda_p = \frac{b}{T}$, where λ_p is the peak wavelength, b is a constant (2.90×10^{-3} m·K) and T is the absolute temperature. Figure 2.2 shows blackbody spectra at different temperatures in agreement with Wien's displacement law. It is clear that as the temperature increases the peak wavelength shifts toward shorter wavelengths (higher energy). While Wien's theory for the spectral intensity of blackbody radiation agreed very well with experimental results for short wavelengths, it drastically failed for long wavelengths. Rayleigh and Jeans developed a classical theory for the spectral intensity of blackbody radiation that correctly predicted the spectral intensity for long wavelengths, but led to an energy output that diverges toward infinity as the wavelength goes to zero, an important erroneous result in physics known as the ultraviolet catastrophe.

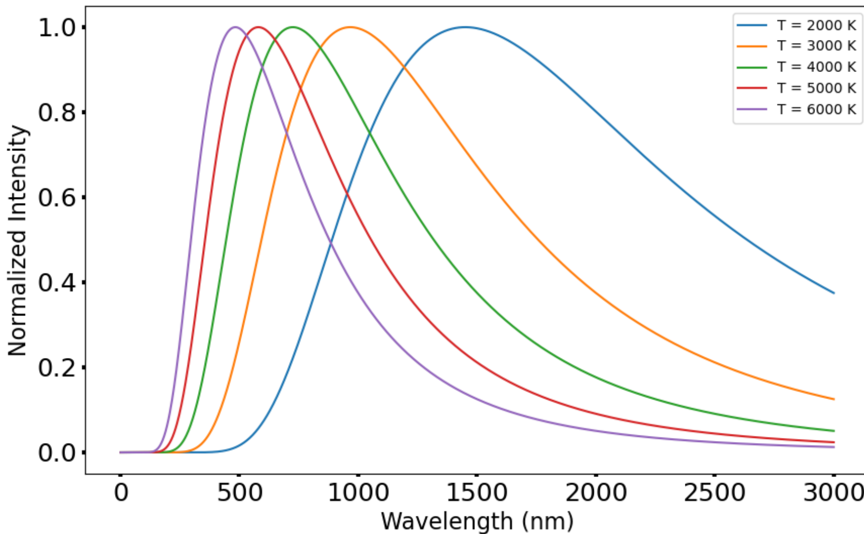

Figure 2.2: Blackbody radiation for different temperatures according to Wien's displacement law.

In 1900, Max Planck resolved the contradictions by developing a new theory based on the quantum properties of electromagnetic radiation[43]. The result is summarized in his famous radiation law (Eq. 2.1),

$$I(\lambda,T) = \frac{2hc^2}{\lambda^5} \frac{1}{\exp\left(\frac{hc}{\lambda k_B T}\right) - 1} \quad , \tag{2.1}$$

where λ is the wavelength, T is the absolute temperature, k_B is Boltzmann's constant ($1.38 \times 10^{-23} J \cdot K^{-1}$) and h is Planck's constant ($6.63 \times 10^{-34} J \cdot s$).

2.2. Semiconductors

Semiconductors (SCs) are crystalline materials with a conductivity between that of a conductor and an insulator. Semiconductors can be made of a single element, e.g., silicon (Si) or germanium (Ge), or with a combination of two elements (binary compounds), three elements (ternary alloys), or more. When many atoms are brought together in a SC, complex energy

bands are formed, of which the two most important are referred to as the valence band and conduction band. Figure 2.3 shows the energy band structure of Si and GaAs, respectively. The electrons populate the conduction band minima with a kinetic energy approximated by a parabola similar to a free electron,

$$E = E_c + \frac{p^2}{2m_e} \quad , \tag{2.2}$$

where m_e is the effective mass of the electron and p is the momentum. A similar relation can be written for holes in the valence band by replacing the effective electron mass by the effective hole mass. The conduction band and valence band are separated from each other by a bandgap, E_g, in which no energy states exist. If the conduction band minimum and the valence band maximum occur at the same crystal momentum, the SC is said to have a direct band gap (as in GaAs). In an indirect bandgap SC (such as Si) the conduction band minimum and the valence band maximum occur at different crystal momenta. In a direct band gap SC, an electron can be excited from the valence band to the conduction band by absorbing a photon with sufficient energy to bridge the band gap. In an indirect band gap semiconductor, this transition requires both a change in momentum and energy. Optical transitions in indirect band gap semiconductors therefore require additional phonons to ensure conservation of both energy and momentum.

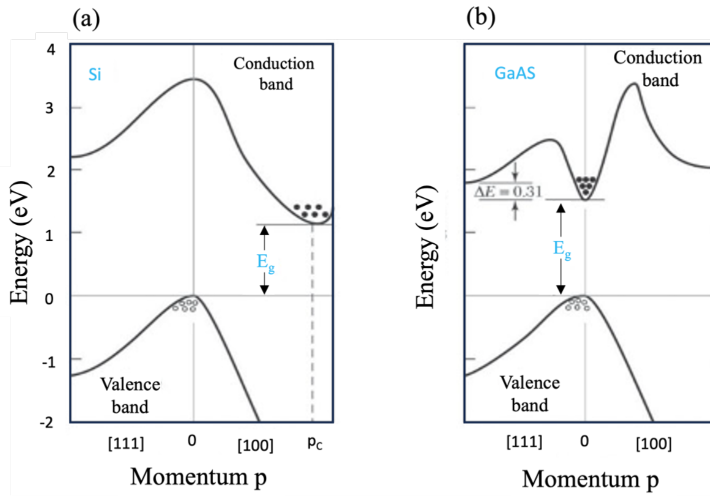

Figure 2.3: Energy band structure of a) Si and b) GaAs [44].

In practice, these complicated band structures can often be replaced by a much simpler schematic energy band diagram (Fig. 2.4 (a)), basically showing the conduction band edge, E_C, and valence band edge, E_V, versus position in e.g., a device. Here, the band gap E_g is given by E_C - E_V. At zero temperature, electrons are bound to the host elements in the lattice and reside in the valence band, leaving the conduction band empty. If enough energy is added by heating or illumination, electrons can bridge the bandgap and start populating the conduction band, leaving behind an equal number of holes in the valence band. The Fermi level is a reference defined as the energy level where the probability of electron occupation is exactly 50%. For an intrinsic SC (without doping) the Fermi level is approximately in the middle of the bandgap.

The probability that an electron occupies an energy level with energy E is given by the Fermi-Dirac distribution function stated in equation 2.3 below.

$$F(E) = \frac{1}{1+e^{(E-E_F)/k_BT}} \quad , \tag{2.3}$$

where k_B is the Boltzmann's constant ($1.38 \times 10^{-23} J \cdot K^{-1}$), T is the absolute temperature and E_F is the Fermi level. The density of states *N(E)* in a SC is defined as the number of allowed energy states (including spin) per energy interval (*dE*) and unit volume. Thus, the electron concentration in the conduction band can be calculated by integrating the product *N(E)·F(E)·dE* from the bottom of the conduction band to the top of the conduction band[44]. Figure 2.4 shows the schematic energy band diagram, density of states, Fermi distribution function, and carrier concentration for an intrinsic bulk SC.

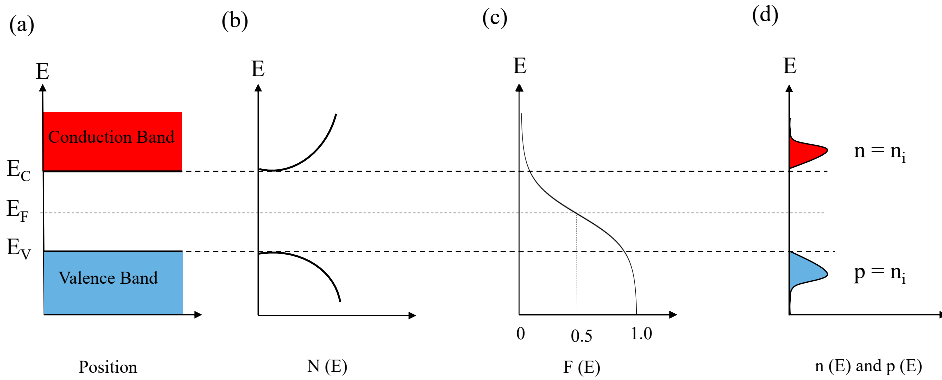

Figure 2.4: a) Schematic energy band diagram, b) density of states, c) Fermi distribution, and d) carrier concentration for an intrinsic SC.

By introducing impurity atoms (dopants) to an intrinsic SC, new energy levels can be formed in the bandgap. Such SCs are referred to as extrinsic (doped). Two distinctly different doping agents exist, called donors and acceptors, that strongly influence the electronic properties of the host SC. A donor (acceptor) doping refers to incorporation of atoms in the host crystal that creates an energy level in the bandgap, close to the conduction (valence) band, which releases mobile electrons (holes) in the SC. Figure 2.5 shows the schematic energy band diagrams of a p-type and an n-type SC with the acceptor energy level (E_a) and donor energy level (E_d), respectively, and the corresponding Fermi level.

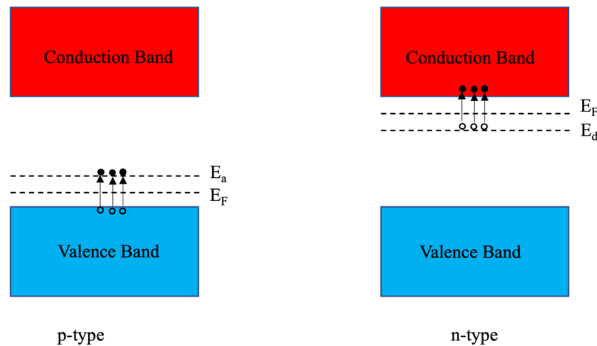

Figure 2.5: Schematic of the energy band diagram for a p-type and an n-type SC.

2.3. Nanostructures

Homoepitaxy refers to epitaxial growth of a SC layer on top of a substrate made of the same SC, while heteroepitaxy refers to epitaxial growth of a SC layer on top of a different SC substrate, or on an epitaxial layer with different composition. Heteroepitaxial growth, combined with subsequent advanced processing technology such as lithography and etching, has facilitated exciting avenues to fabricate low-dimensional nanostructures. Some of these are shown schematically in Fig. 2.6, and briefly described in the following sections. For these nanostructures, the above-mentioned energy-momentum relation and density of states for a bulk material are not valid and new physical models are needed.

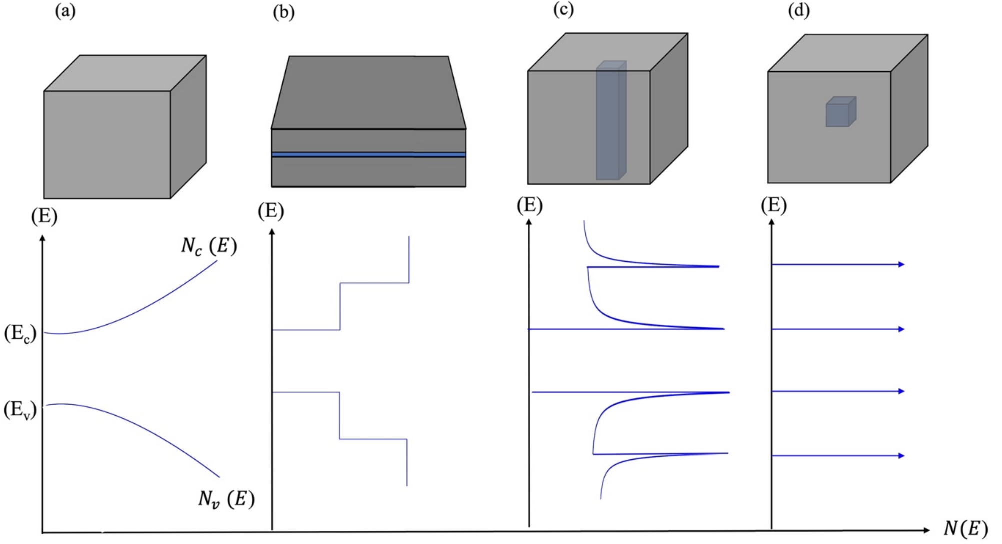

Figure 2.6: Schematic of physical structure and the density of states of a a) bulk SC, b) quantum well, c) quantum wire and d) quantum dot.

2.3.1. Quantum wells

A quantum well (QW), shown in Fig. 2.6 (b), is a heterostructure where a very thin SC layer is sandwiched in between two SC layers with larger band gap. When the thickness, L, of the thin layer is comparable to the de Broglie wavelength ($\lambda_d = h/p$) of an electron, the energy structure will be quantized, resulting in discrete energy levels in both the conduction band and valence band of the QW. In such a heterostructure, electron motion is limited to a 2D surface and Eq. 2.2 needs to be updated. For a sufficiently deep QW, often referred to as a QW with impenetrable walls, the energy structure for electrons (similar for holes) can rather simply be analytically calculated by solving the time-independent Schrödinger equation $(-\frac{\hbar^2}{2m_e}\nabla^2 + V(z))\psi(\boldsymbol{r}) = E\,\psi(\boldsymbol{r})$. The discrete energy levels $\mathcal{E}_n$ for the confined z-direction are given by Eq. 2.4.

$$\mathcal{E}_n = \frac{n^2\pi^2\hbar^2}{2m_e L^2}, \quad n=1, 2, 3.... \tag{2.4}$$

The total energy (Eq. 2.5) is obtained by adding the kinetic energy associated with the free motion of the electrons in the x-y plane of the QW.

$$E(n,\ k_x, k_y) = \mathcal{E}_n + \frac{\hbar^2(k_x^2+k_y^2)}{2m_e}\ , \tag{2.5}$$

where k_x and k_y is the magnitude of the electron wavevector in the x- and y-direction, respectively. The solution to the Schrödinger equation is presented in Fig. 2.7. In contrast to the bulk case, the ground state (n=1) energy is not zero, but shifted by an amount of $\frac{\pi^2\hbar^2}{2m_eL^2}$ with respect to the bottom of the conduction band. The same theory is valid for a hole inside the valence band. As can be noticed in Fig. 2.6 (b), the density of states in a QW is different from that of a bulk semiconductor, increasing in equivalent steps for each new discrete energy level (quantum number n).

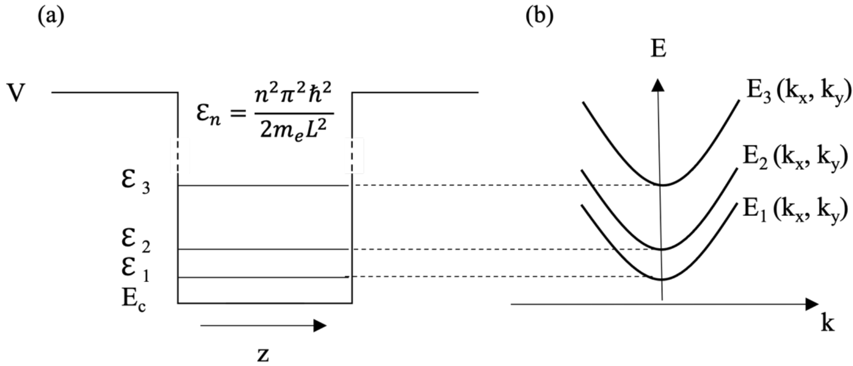

Figure 2.7: Energy structure for an "infinite" QW confined in the z-direction (growth direction). a) The discrete energy levels inside the conduction band and b) the corresponding E-k relation.

For a more realistic finite QW, e.g., a thin layer of GaAs sandwiched in between two layers of AlGaAs (Fig. 2.13), the depth of the well (potential) corresponds to the conduction band offset between GaAs and AlGaAs.

2.3.2. Nanowires

Nanowires are nanostructures with a diameter smaller than around 100 nm. Nanowires are usually referred as 1D structures due to their large length-to-diameter aspect ratio. To obtain a true 1D quantum wire (Fig. 2.6 (c)) confinement, however, the NW diameter has to be comparable to the de Broglie wavelength. Various factors make semiconductor NWs, in particular III-V NWs, of greatest interest for next-generation optoelectronic devices, including high absorption per material volume, tunable electronic parameters via wrap-gating, large flexibility in growth of heterostructures offering complex tunable radial and axial direct bandgap energy landscapes, and potentially defect-free heterogeneous integration with silicon substrates due to strain relaxation. There have been many recent reports on promising NW-based nanophotonic devices including photovoltaic devices[5, 45], LEDs[6], lasers[46, 47], waveguides[48, 49], and photodetectors[10, 11, 50, 51].

Nanowire fabrication is usually categorized into two groups referred to as bottom-up and top-down techniques. In the top-down method, a bulk material is etched with a specific pattern to form the NWs. The diameter and the uniformity of the NWs are limited by the lithography

resolution and the etching characteristics. Moreover, the flexibility in defining complex heterostructures is strongly limited due to issues with defects in lattice-mismatched thin films. In the bottom-up approach, the NWs are epitaxially grown layer by layer. One key advantage here is that heterostructures, or growth on lattice-mismatched substrates, can more easily be pursued due to the small diameter/footprint of the NWs which at least partly relieves the strain. Chemical vapor deposition (CVD), Metalorganic vapor-phase epitaxy (MOVPE) and Molecular-beam epitaxy (MBE) are a few common methods for bottom-up NW growth [52, 53].

In this thesis work the NWs were grown by MOVPE, which is the most common technique for mass production of III-V NWs. Here, seed particles are often used to catalyze the growth and to increase the growth rate in one dimension. Gold nanoparticles (NPs) are usually used because an alloy forms (e.g., Au-In) in the catalyst at growth temperatures around of 400 – 500 °C. Growth takes place by introducing the precursors into the growth chamber by a carrier gas[54]. By changing the precursor and introducing dopants, doped NW heterostructures with different doping profiles in the axial or radial direction can be grown[55]. A detailed discussion of NW growth is presented in Chapter 3.

2.3.3. Quantum dots

A quantum dot , shown in Fig. 2.6 (d), is a nanostructure that is confined in all three directions, where the energy structure in the simplest case is calculated by solving Schrödinger's equation, similar to above, in all three dimensions and simply adding the extracted energies together. The confined energy levels are well separated, and the density of states is represented by delta functions (Fig. 2.6 (d)). An important observation is that the density of states increasingly sharpens with a reduction in dimensionality from bulk SC to QDs. The size of a QD plays an important role for its optical properties. For instance, a blue shift in the band gap emission from QDs is observed when their diameter is decreased[56]. The electronic structure of a QD resembles that of atoms, and QDs are sometimes referred to as artificial atoms[57].

2.4. Optical properties of semiconductors

2.4.1. Interband transitions in bulk semiconductors

An interband transition is known as the transition of an electron between the valence band and the conduction band of a SC, which can be achieved by absorption or emission of a photon. In the case of absorption, an electron is excited from the valence band to the conduction band, leaving behind a hole in the valence band. To calculate the optical transition matrix element for this case, we consider the electric field of a propagating light wave in the **k**-direction with a polarization **e** as a perturbation potential in the Schrödinger equation. The wave function can be written as a product of an envelope function and a Bloch function $\psi(\mathbf{r}) = u(\mathbf{r})e^{i\mathbf{kr}}$. To calculate the interband transition probability, the wave function of the initial state (i) and the final state (f) are inserted into the matrix elements shown below.

$$\langle f|\mathbf{e}.\hat{\mathbf{p}}|i\rangle = \int \psi^*_{f\mathbf{k}'}(\mathbf{r})\,\mathbf{e}.\hat{\mathbf{p}}\,\psi_{i\mathbf{k}}(\mathbf{r})d^3\mathbf{r} = \frac{1}{\Omega}\int u^*_{f\mathbf{k}'}(\mathbf{r})e^{-i\mathbf{k}'\mathbf{r}}\mathbf{e}.\hat{\mathbf{p}}\,u_{i\mathbf{k}}(\mathbf{r})e^{i\mathbf{kr}}d^3\mathbf{r}\ , \quad (2.6)$$

where Ω is the volume of the material introduced for normalization. In quantum mechanics, the momentum operator ($\hat{\mathbf{p}}$) is defined as $-i\hbar\nabla$. So, Eq. 2.6 can be written as below.

$$\langle f|\mathbf{e}.\hat{\mathbf{p}}|i\rangle = \frac{1}{\Omega}\mathbf{e}\int u^*_{f\mathbf{k}'}(\mathbf{r})e^{i(\mathbf{k}-\mathbf{k}')\mathbf{r}}\,[\hbar\mathbf{k}u_{i\mathbf{k}}(\mathbf{r}) + \hat{\mathbf{p}}u_{i\mathbf{k}}(\mathbf{r})]d^3\mathbf{r} \quad (2.7)$$

Since $u^*_{f\mathbf{k}'}$ and $u_{i\mathbf{k}}$ are orthogonal (they are eigenstates of the same Hamiltonian), the first term in the square bracket in Eq. 2.7 will be zero. The second term is zero, unless $\mathbf{k} = \mathbf{k}'$**.** So, the result will be the matrix element of u(**r**). Furthermore, since u(**r**) is periodic it gives the same contribution in each unit cell, wherefore the integral can be reduced to volume of a unit cell.

$$\langle f|\boldsymbol{e}.\hat{\boldsymbol{p}}|i\rangle = \frac{1}{\Omega_{cell}}\int_{cell} u^*_{f\mathbf{k}'}(\boldsymbol{r})\,\boldsymbol{e}.\hat{\boldsymbol{p}}\,u_{i\mathbf{k}}(\boldsymbol{r})\,d^3\boldsymbol{r} = \langle u_f|\boldsymbol{e}.\hat{\boldsymbol{p}}|u_i\rangle \quad (2.8)$$

This describes the transition between two different bands like the valence and conduction band and known as interband transition.

2.4.2. Interband transitions in quantum wells

The wave function in a QW quantized in the z-direction can be written as a product of a Bloch function parallel to the well and a bound state perpendicular to the well.

$$\psi(\mathbf{r},\mathrm{z}) = \frac{1}{\sqrt{A}}\phi(\mathrm{z})e^{i\mathbf{kr}} , \quad (2.9)$$

where A is a normalization factor. Assigning the initial state as *i* and the final state as *f*, the transition matrix element for this case can be written as below.

$$\langle f|\mathbf{e}.\hat{\mathbf{p}}|i\rangle = \frac{1}{A}\int \phi^*_f(\mathrm{z})\,e^{-i\mathbf{k}'\mathbf{r}}\mathbf{e}.\hat{\mathbf{p}}\;\phi_i(\mathrm{z})\,e^{i\mathbf{kr}}d^3\mathbf{r} \quad (2.10)$$

The envelope function $\phi(\mathrm{z})$ is a slowly varying function over a unit cell compared to the Bloch function which varies in each cell. So, $\phi(\mathrm{z})$ can be considered constant for each unit cell and the integral for that can be replaced by a summation over the unit cells.

$$\langle f|\mathbf{e}.\hat{\mathbf{p}}|i\rangle = \frac{1}{A}\sum_j^{cell}\phi^*_f(\mathrm{z}_j)\,\phi_i(\mathrm{z}_j)\int_{cell,j} e^{-i\mathbf{k}'\mathbf{r}}\mathbf{e}.\hat{\mathbf{p}}\;e^{i\mathbf{kr}}d^3\mathbf{r} \quad (2.11)$$

The integral over the unit cell shows the matrix element between the initial (valence band) and the final (conduction band) state of the Bloch function $\langle u_{f0}|\mathbf{e}.\hat{\mathbf{p}}|u_{i0}\rangle$. Also, we can rewrite summation as an integral now.

$$\langle f|\mathbf{e}.\hat{\mathbf{p}}|i\rangle = \langle u_{f0}|\mathbf{e}.\hat{\mathbf{p}}|u_{i0}\rangle\int \phi^*_f(\mathrm{z})\,\phi_i(\mathrm{z})\,d^3\mathbf{r} \quad (2.12)$$

So, the interband transition in a QW is separated into two parts; one part related to the Bloch function and the polarization of the incoming light, and one related to the envelope function. This gives rise to the selection rules according to which only certain transitions are allowed.

i) For a symmetric potential, only transitions between the initial and the final states that have the same parity are allowed.

ii) For the case of an identical QW for electrons and holes ($\Delta E_c = \Delta E_v$), and with the same effective mass, only transitions between the states that have the same quantum number are allowed (Δn =0).

iii) If the well is not identical for the electrons and holes, the transitions with Δn =0 will have the highest probability.

2.4.3. Intersubband transitions in quantum wells

In contrast to interband transitions, intersubband transitions in QWs require the presence of an electric field component along the growth direction. Due to this fact, QWs need to be optically excited at some angle to respond to intersubband radiation. If the impinging light has x-polarization, $\mathbf{e}.\,\widehat{\mathbf{p}}$ will be $-i\hbar\frac{\partial}{\partial \mathrm{x}}$ and will affect just the plane wave with no operation on the envelope function. This means that there will be no intersubband transition for x-y (in-plane) polarization:

$$\langle f|\hat{p}_x|i\rangle = \hbar k_x \langle f\mathbf{k}'|i\mathbf{k}\rangle = 0 \tag{2.13}$$

In contrast, if the incident light is polarized in the **z**-direction (out-of plane), $\mathbf{e}.\,\widehat{\mathbf{p}}$ will be $-i\hbar\frac{\partial}{\partial \mathrm{z}}$ which will affect $\phi(\mathrm{z})$ and the matrix elements can be written as below.

$$\langle f|\hat{p}_z|i\rangle = \frac{1}{A}\int dz \int \phi_f^*(z) e^{i(\mathbf{k}-\mathbf{k}')\mathbf{r}}\, \hat{p}_z\, \phi_i(z)\, d^2\mathbf{r} \tag{2.14}$$

The integral over **r** is zero, except for the case when **k** is equal with $\mathbf{k}'$**.** Therefore, the integral in Eq. 2.14 can be written as follows:

$$\langle f|\hat{p}_z|i\rangle = -i\hbar \int \phi_f^*(z)\frac{\partial \phi_i(z)}{\partial z}\, dz \tag{2.15}$$

This means that the matrix elements for light polarized in **z**-direction is not zero and intersubband transition can thus occur.

2.5. Infrared photodetectors

2.5.1. p-n and p-i-n photodiodes

By bringing an n-type and a p-type SC material into contact, a p-n junction, or diode, is created where the majority carriers from the n-region (electrons) diffuse to the p-region and the majority carriers in the p-region (holes) diffuse to the n-region. This motion of carriers to the other side leaves behind positively (negatively) ionized donors (acceptors) in the n-region (p-region). As a result, a narrow region is created on both sides of the physical junction that is depleted of mobile carriers, a region referred to as the depletion region. The fixed charge from the ionized donors and acceptors forms an electric field pointing from the positive charge (n-side) to the negative charge (p-side). Figure 2.8 (a) shows a schematic of the p-n junction in equilibrium along with its band structure.

This established electric field creates corresponding electron and hole drift currents that at thermal equilibrium balance the diffusion currents discussed above, which results in a constant

Fermi level across the junction and a built-in potential (V_0), as shown in Fig. 2.8 (a). If a negative bias ($V_R < 0$) is applied to the p-side (reverse bias), the depletion region gets wider, the built-in potential is increased (V_0+V_R), and the diffusion currents decrease. In fact, when a large reverse bias is applied, the diffusion of carriers inside the depletion region is negligible. However, minority carriers can still diffuse from the neutral regions to the edges of the depletion region and then drift to the other side. Therefore, there is a saturation (leakage current) which corresponds to the sum of the electron and hole drift currents of minority carriers that diffuse and reach into the depletion region. Conversely, if a positive bias ($V_F > 0$) is applied to the p-side of the junction (forward bias), majority carriers are injected from both sides which results in a narrower depletion region and a reduction of the built-in potential (V_0 -V_F), increasing the diffusion current through the diode. Figures 2.8 (b) and (c) show the energy band diagram and the Fermi level for a p-n junction under reverse and forward bias condition, respectively.

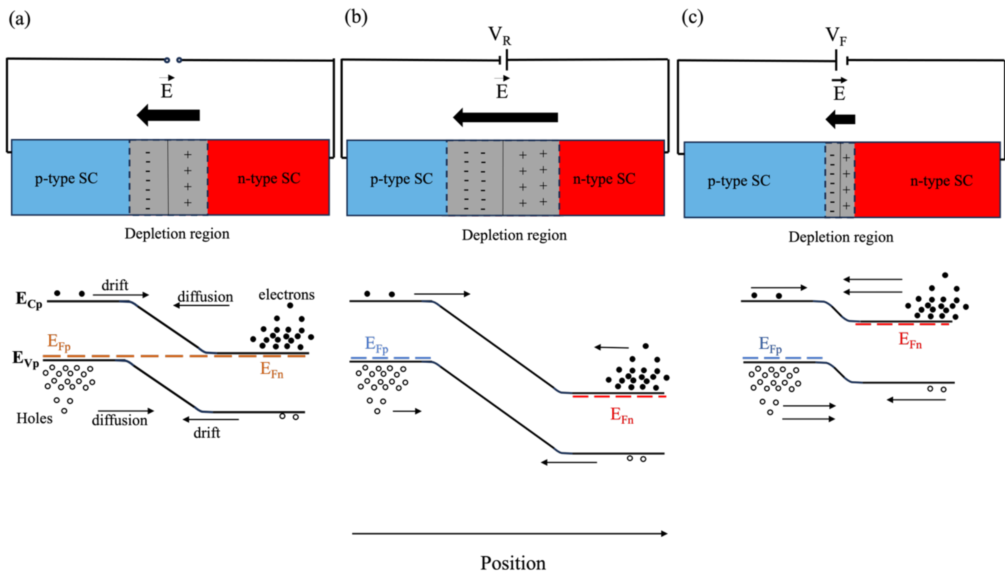

Figure 2.8: Schematics and energy band diagrams for a p-n junction a) in equilibrium, b) under reverse bias and c) under forward bias conditions.

When a p-n junction under reverse bias is illuminated with photons with energies higher than the SC's bandgap, the photons are absorbed and electron-hole pairs (EHP) are generated as shown in Fig. 2.9. The high electric field in the depletion region separates the electrons and holes efficiently before they recombine, resulting in a photocurrent (PC) that can be measured in the external circuit. Under reverse bias, the width of the depletion region is increased, resulting in a higher absorption volume, which is favorable in photodetection applications.

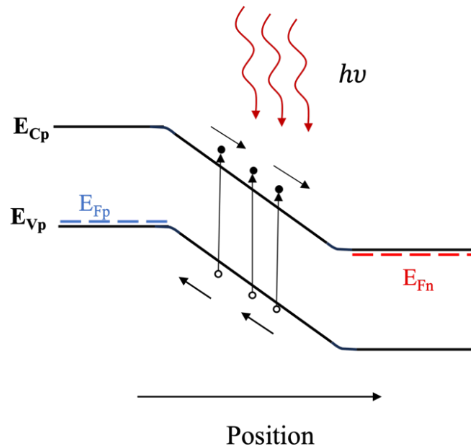

Figure 2.9: Reverse-biased p-n junction under illumination.

The physical principles for a p-i-n photodiode are similar to those of the p-n junction. A thick intrinsic layer is sandwiched between the p-region and n-region (Fig. 2.10 (a)) to increase the absorption volume and thereby the efficiency of the photodiode. Figure 2.10 (b) shows the schematics of a p-i-n junction under illumination.

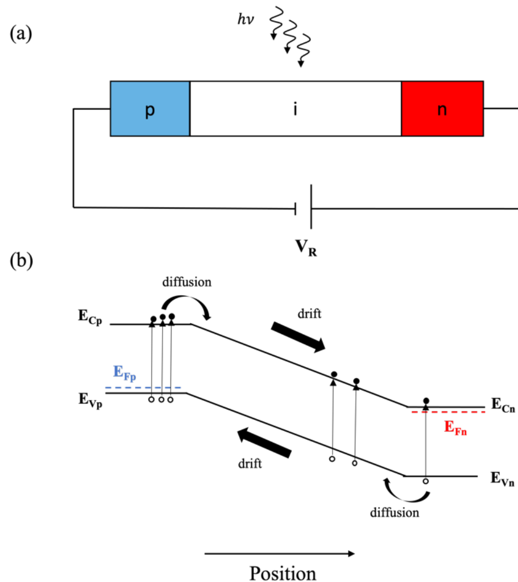

Figure 2.10: Schematics of a p-i-n junction under illumination. a) Physical layout and b) energy band diagram under reverse bias.

Compared to p-n photodiodes, p-i-n photodiodes usually show faster response time (due to lower capacitance), lower dark current (due to the intrinsic region) and slightly lower sensitivity. Nowadays, commercial NIR and SWIR photodiodes are mainly based on Si (450 nm to 1.1 µm), InGaAs (800 nm to 2.6 µm) and Ge (800 nm to 1.8 µm). Generally, photodiodes have advantages like compactness, fast response, broad spectral response, low cost and low noise/dark current, but suffer from degraded performance at higher temperature due to rapidly increasing dark current.

2.5.2. Photoconductors

In essence, a photoconductor is a resistor with a conductivity that increases under illumination. A photoconductor can be fabricated simply by making two contacts on a piece of intrinsic SC. However, for better carrier extraction and performance, the SC is usually highly doped in the contact regions. Figure 2.11 shows an n^+-i-n^+ photoconductor along with its band structure in equilibrium. As can be seen in Fig. 2.11 (b), in contrast to p-n and p-i-n photodetectors, there is no internal electric field in a photoconductor, and so an external bias is needed to operate the photoconductor.

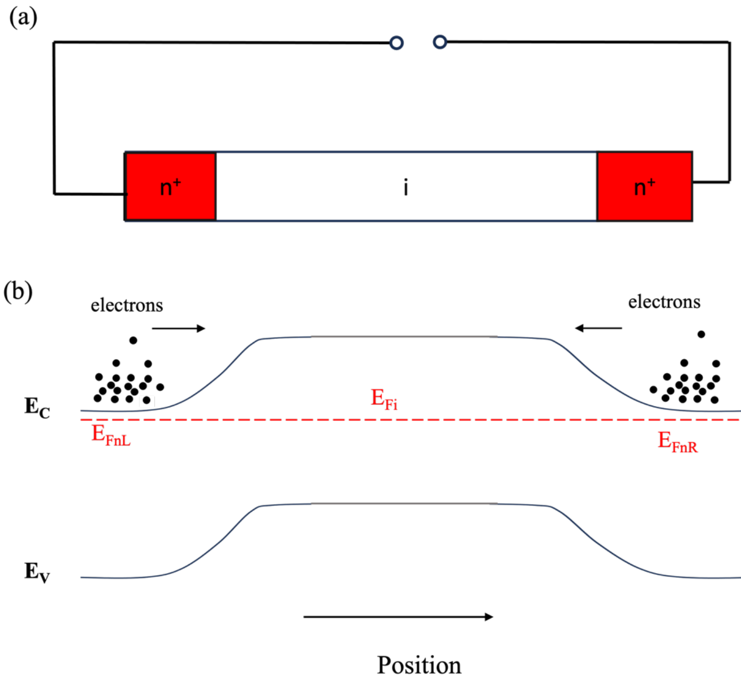

Figure 2.11: Schematics of an n^+-i-n^+ photoconductor in equilibrium. a) Physical layout and b) energy band diagram.

Figure 2.12 (a) shows the n^+-i-n^+ photoconductor under bias and illumination along with its band structure in (b). Impinging photons with higher energy than the SC's band gap can excite electrons from the valence band to the conduction band, leaving behind holes in the valence band which increases the conductivity of the material. The difference in conductivity of the material under illumination and in dark is defined as the photoconductivity ($\Delta\sigma$) given by:

$$\Delta\sigma = q(\mu_e \Delta n + \mu_h \Delta p), \tag{2.16}$$

where Δn and Δp are the excess electron and hole concentrations resulting from the incident light, μ_e and μ_h are the electron and hole mobilities, and q is the elementary charge ($1.6 \times 10^{-19} C$).

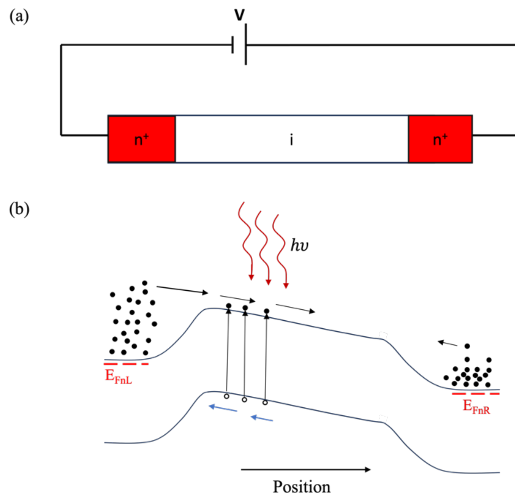

Figure 2.12: Schematics of a biased n^+-i-n^+ photoconductor under illumination. a) Physical layout and b) energy band diagram.

2.5.3. HgCdTe detectors

The tunable bandgap of $Hg_{1-x}Cd_xTe$ (HgCdTe, MCT) alloys, discovered as early as 1959[58], provides a unique freedom in designing detectors in a broad spectral range from SWIR to LWIR. HgTe is a semimetal with a bandgap of 0 eV, while CdTe is a semiconductor with a bandgap of 1.5 eV. By changing the amount of Cd in the alloy, the bandgap can thus at least theoretically be tuned from 0.0 eV to 1.5 eV. Other advantages of MCT alloys include a high absorption coefficient and high operating temperature, properties that have made MCT detectors among the most widely used IR photodetectors so far[59]. However, these detectors suffer from some serious disadvantages. Since HgCdTe is toxic, soft and fragile, special precautions need to be taken during growth and processing. Other challenges in epitaxial growth are the high vapor pressure of Hg, high defect density, and significant surface leakage currents that reduce the device performance. The exact alloy composition is also difficult to control which makes it difficult to fabricate in particular LWIR detectors with a well-defined cut-off wavelength and high yield[58].

2.5.4. Quantum well infrared photodetectors

An alternative device for LWIR detection is the quantum well IR photodetector (QWIP). As explained above, a QW is made of a thin semiconductor layer sandwiched in between two semiconductors with larger bandgap, as shown in Fig 2.13 (a) for the case of an AlGaAs/GaAs QW. Under LWIR illumination, electrons are optically excited from the ground state to the first excited state in the conduction band of the QW, a process known as an intersubband transition (Fig. 2.13 (b)). The excited carrier can subsequently escape into the surrounding semiconductor by thermal emission, assisted by various barrier-lowering mechanisms, including the Poole-Frenkel effect and phonon-assisted tunneling[60], and be driven to the outer circuit by an applied electric field (bias). The spectral sensitivity window, usually in the range of 3 µm (0.4 eV) to 20 µm (0.06 eV)[61], can be tuned by controlling the thickness and composition of the QW, and the height of the barrier (set by the conduction band offset between GaAs and AlGaAs). Today, QW growth is relatively mature, which offers the possibility of mass production of large-size focal plane arrays (FPAs) for imaging purposes. Also, compared

to MCT detectors, QWIPs offer advantages such as lower noise and higher sensitivity to a specific wavelength.

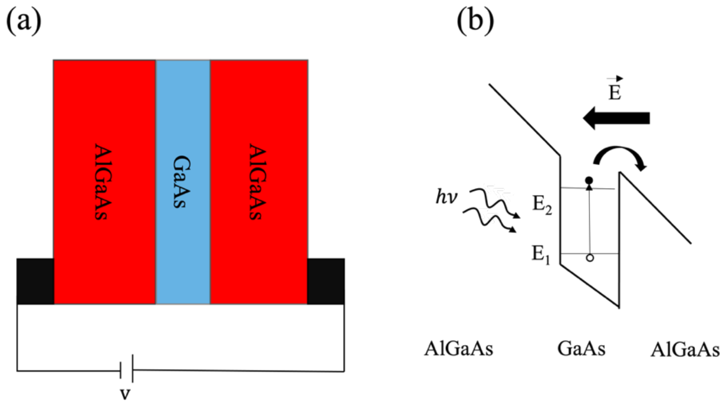

Figure 2.13: a) Schematic physical structure of a QWIP and b) the corresponding schematic conduction band profile of a biased QWIP under illumination. An intersubband transition is indicated with the subsequent escape to the surrounding AlGaAs barrier.

2.5.5. Quantum dot infrared photodetectors

As explained in 2.3.2, when nanostructures are spatially confined in all three dimensions, a QD is formed. Quantum dot IR photodetectors (QDIPs) comprise single- or multiple stacked layers of QDs. They do not suffer from the normal incidence limitation in QWIPs because of the confinement in all three directions which induces non-zero optical matrix elements. Quantum dot layers are usually doped to efficiently populate the ground state with electrons (or holes), thereby improving the intersubband signal. An applied electric field collects the photoexcited charge carriers and drives them to the outer circuit as a PC. Other advantages of QDIPs include a reduced dark current, and longer photocarrier lifetime (reduced electron-phonon scattering). Moreover, due to the three-dimensional confinement and discrete energy levels, a broad spectral detection range can be covered by changing the QDs' size [62, 63].

2.5.6. Type-II superlattice infrared photodetectors

When two semiconductor materials are brought together, the valence bands and conduction bands can align in different ways. One way is the type-II alignment where both the conduction band and the valence band of one semiconductor are located above the conduction band of the other semiconductor. If many thin layers of this structure are grown on top of each other, artificial minibands are created for electrons and holes. Such a structure is called a type-II superlattice (T2SL), and was first proposed as an IR detector in 1987 by Smith and Mailhiot[64]. Figure 2.14 shows the schematic band alignment, minibands and optical transitions in an InAs/GaSb T2SL. Photodetectors based on T2SL structures offer advantages over MCT detectors, such as higher uniformity, stability, and affordability for fabrication of commercial focal plane arrays, especially in the LWIR region[65].

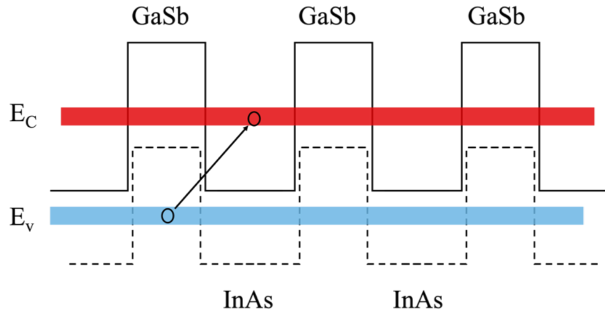

Figure 2.14: Band alignment and formed minibands in an InAs/GaSb T2SL.

2.5.7. Nanowire-based infrared photodetectors

Nanowire IR photodetectors have been studied both as single elements and large arrays on different substrates, including Si[10, 11, 66-68]. A single NW offers a straightforward platform for fundamental device investigations, free from the complexities arising from neighboring NWs or growth non-uniformities[69]. Photodetectors based on single NWs can be realized either with vertically oriented single NWs grown directly on a substrate or by horizontally positioning single NWs on a substrate, typically achieved through manual transfer. However, while horizontally oriented single NW photodetectors have been extensively explored, their vertically oriented counterparts have received comparatively less attention, likely attributed to the challenges associated with vertical processing[70]. Noteworthy are high-performance single NW photodetectors based on materials such as GaN with high responsivity and gain[71, 72], InAs[73], GaSb with broad spectral response[74] and high performance InGaAs[75], among others.

Conversely, vertically standing NW arrays hold significant importance, showcasing exceptional characteristics including enhanced sensitivity, improved absorption with less material volume thanks to robust NW-light coupling, and beneficial optical resonance effects[76]. Vertical NW array photodetectors based on InAs[77], InGaAs[78], GaAsSb[27] and InP with multiple axially embedded InAsP QDiscs [10] are a few examples. Among III-V NWs, InP is one of the most widely studied candidates offering advantageous characteristics e.g., high electron mobility (almost 5 times higher than Si), direct bandgap and low sheet resistance. InP with a direct bandgap of 1.34 eV at room temperature covers the visible and NIR regions. By embedding thin segments (QDiscs) of a lower bandgap SC, e.g. InAsP, in the NWs, and taking advantage of confined energy levels in the QDiscs, the responsivity can be extended to LWIR[11].

Using a heavily-doped substrate as a gate for a horizontal single NW, or employing radial wrap-around gate (GAA) contacts for vertically (or horizontally) oriented single or array NWs, represents an effective strategy for tuning both the spectral responsivity range and electron concentration (Fermi level) within NW detectors. Such three-terminal devices can bring together the advantages of a photodetector and transistor. Due to the time consuming and challenging processing required for fabrication of vertically standing NW array phototransistors, all reported GAA-NW detectors up to recently were single-NW devices[22-24, 79] In the last phase of this thesis, we report on the first three-terminal GAA InP NW phototransistors, with 20 InAsP QDiscs embedded inside the i-segment of each NW. These phototransistors showed interesting properties in terms of more freedom in controlling the electrical and optical properties of the phototransistor. For instance, by changing the gate bias, the photoresponse can be tuned in a way to include or exclude the NIR range which can bring

advantages in many applications where monitoring of the spectral content of a signal is important. These photodetectors are discussed at length in Chapters 5, 6 and 7.

2.6. Figures of merit of photodetectors

Photodetectors are characterized by some key figures of merit which are presented below with an explanation and relevant equations.

2.6.1. Responsivity

Responsivity is one of the most important parameters to quantify a photodetector's performance. It is defined as the ratio between the generated PC (I_{PC}) and input optical power (P_{opt}). The responsivity, R, is calculated by the equation below.

$$R = \frac{I_{PC}}{P_{opt}} = \frac{I_{PC}}{\phi_{ph} \cdot h\nu} \quad , \tag{2.17}$$

where ϕ_{ph} is the photon flux (number of photons reaching the device per second) and $h\nu$ is energy of the impinging photons.

2.6.2. Quantum efficiency

Th internal quantum efficiency ($IQE\ or\ \eta_I$) presents the number of the generated EHPs per absorbed photon, while the external quantum efficiency ($EQE\ or\ \eta_E$) quantifies the number of detected carries in the outer circuit per incoming photon:

$$\eta_E = \frac{\#detected\ carriers}{\#incoming\ photons} = \frac{I_{PC}/e}{\phi_{ph}} \tag{2.18}$$

Generally, for a specific incident photon flux, a percentage is reflected and a percentage is absorbed. EQE takes all the impinging photons into account, while IQE considers just the absorbed photons. Also, there is a direct relation between the number of detected carriers and number of photogenerated carriers. So, one can conclude that EQE includes IQE within itself. While the IQE can be 100%, meaning all the absorbed photons can generate EHPs, the EQE is usually less than 100% due to reflection, scattering and transmission.

2.6.3. Gain

The gain (g) presents the number of detected carriers in the outer circuit per generated EHP. The textbook definition of gain in a photoconductor is the ratio between the minority carrier lifetime and carrier transit time through the detector element. However, this classic definition is not able to explain the origin of very high gain measured experimentally in some photoconductors. Traps and photogating play a crucial role in photoconductors' gain. This is discussed in detail in the next section, and in Chapter 5 when presenting our two-terminal photodetectors. By considering the definition for IQE above, we can rewrite Eq. 2.17 as follows:

$$R = \eta_I g \frac{e\lambda}{hc} \quad , \tag{2.19}$$

where λ is the wavelength, h is Planck's constant and c is the speed of light.

2.6.4. Photogating

In classical textbooks in semiconductor physics, gain in a photoconductor is defined as the ratio between the minority carrier lifetime and carrier transit time through the detector element. While this concept is widely accepted and used[80-82], there is a conflict between some very high gains reported experimentally, in particular in nanoscale photodetectors, and the theoretical prediction[83-85]. The contradiction arises from the fact that the classical theory neglects the strongly non-uniform carrier distribution present under normal operating conditions. In fact, in most photoconductors gain is a result of photogating and feedback of trapped charge carriers on the electrostatic potential distribution in the photodetector[86]. Photogating can be described as a modulation of the device conductance through photo-induced carrier dynamics involving trap states. When carriers are trapped in defects with a certain spatial distribution, a potential (electric field) is formed which behaves like a gate in a MOSFET. In low-dimensional photoconductors such as NWs, with their large surface-to-volume ratio, surface or interface traps can have a profound impact on the observed gain. Fig. 2.15 shows the photogating mechanism in a NW with acceptor surface traps, similar to our investigated two- and three-terminal devices discussed in Chapters 5, 6 and 7. In the dark, electrons are trapped in acceptor-like traps, creating a potential barrier between the n^+- and i-segment, pushing the channel electrons to the NW's center by an electrostatic force which narrows the conductance channel and reduces the dark current. Upon illumination with photons with energy higher than the SC's bandgap, electrons are excited to the conduction band, leaving behind holes in the valence band. These photogenerated holes move towards the NW surface where they can recombine with the trapped electrons which opens the conductance channel and increases the photocurrent. By considering the definition of gain in 2.6.3, it is obvious that photogating will increase a photodetector's gain, as each photogenerated EHP results in several detected electrons in the external circuit. Photogating in various low-dimensional systems was discussed in a recent review article by Fang *et al*[87].

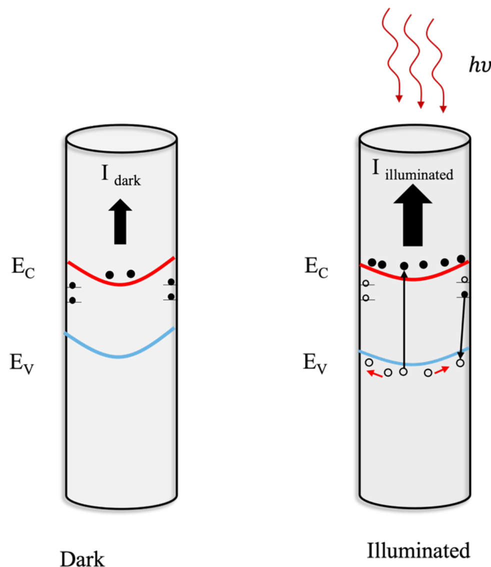

Figure 2.15: Photogating in a NW with acceptor surface traps.

2.6.5. Response time and bandwidth

The response (rise) time of a photodetector is given by the time it takes for the photocurrent to increase from 10% to 90% of the maximum value after a light pulse. The related bandwidth (BW) of a photodetector has an inverse relation with the rise time as shown below.

$$BW = \frac{0.35}{\tau} \tag{2.20}$$

2.6.6. Noise equivalent power and detectivity

The noise equivalent power (*NEP*) is an important figure of merit for a photodetector defined as the optical power at which the detector signal has a signal-to-noise ratio of unity (*SNR*=1), measured with a 1 Hz bandwidth. The related detectivity, *D*, is defined as NEP^{-1}, while the specific detectivity, D^*, also takes the device area (A) and bandwidth (BW) into account as shown below.

$$D^* = NEP^{-1} \cdot \sqrt{A \cdot BW} \tag{2.21}$$

2.6.7. Dark current

As the name implies, dark current refers to the current through a biased photodetector without any illumination. It is crucial for a photodetector to have a low dark current if it is to achieve a high signal-to-noise ratio. Depending on the photodetector's type, the dark current can stem from various sources, such as diffusion, thermal emission, tunneling and surface leakage. Thermal emission, for instance, is a process where carriers can be excited from a confined energy level in a QWIP to the surrounding continuum of energy levels, underlying the generation of dark current. The thermal emission can be decreased by cooling the detector to low temperatures, where trapped electrons will not have sufficient energy to be excited to the continuum. In detectors based on nanostructures such as NWs, surface leakage can be an important source of dark current. Because of this, NWs are usually passivated to mitigate surface current. Other factors such as surface traps and doping profiles can also play a key role in dark current generation. In the NWs studied in this thesis work, a combination of compensational doping and NW/oxide interface traps leads to extremely low dark current levels, as discussed in the results section below.

3. Nanowire growth and device processing

The details of the growth of InP/InAsP NWs, as well as fabrication of two-terminal photoconductors and three-terminal GAA-phototransistors are presented in this chapter.

3.1. Nanowire growth

In this thesis work all NWs were grown by the low-pressure MOVPE method. For growth of n^+- i - n^+ InP NW arrays with axially embedded InAsP QDiscs , first a highly doped n-type InP (111)B wafer was hexagonally patterned with Au NPs using Talbot displacement lithography[88], evaporation of Au and lift-off. The Au NPs, with diameter, thickness, and pitch of 130 nm, 40 nm and 500 nm, respectively, acted as seeds during the growth and set the diameter of the final NWs. The patterned wafer was diced into small pieces (1 × 1 cm^2) and inserted into a low-pressure (100 mbar) Aixtron 200/4 MOVPE growth chamber. The growth started at 400 °C by introducing trimethylindium (TMIn) as the precursor for In, phosphine (PH_3) as the precursor for P and tetraethyltin (TESn) as the n-type doping precursor. Diethylzinc (DEZn) was used as precursor for the Zn doping introduced during growth of the i-segment to compensate for the unintentional residual n-doping. To grow the 20 InAsP QDiscs inside the i-segment of the NWs, PH_3 was replaced by arsine (AsH_3) repeatedly for 1 s or 2 s (determining the QDiscs' thickness), while keeping the TMIn flow switched off. The liquid Au-In seed particles provide the In supply in this case. The TMIn flow was always on during growth of the InP barriers between the QDiscs. Figure 3.1 shows a schematic of the growth process. Figures 3.2 (a) and (b), respectively, show a scanning electron microscopy (SEM) image of a typical as-grown array of NWs and a transmission electron microscopy (TEM) image of a single NW with length of around 2 μm and diameter of 135 nm. The bottom and top 500 nm segments of the NWs are n^+, while the middle 1 μm long segments with QDiscs are nominally intrinsic after adding compensating Zn acceptors.

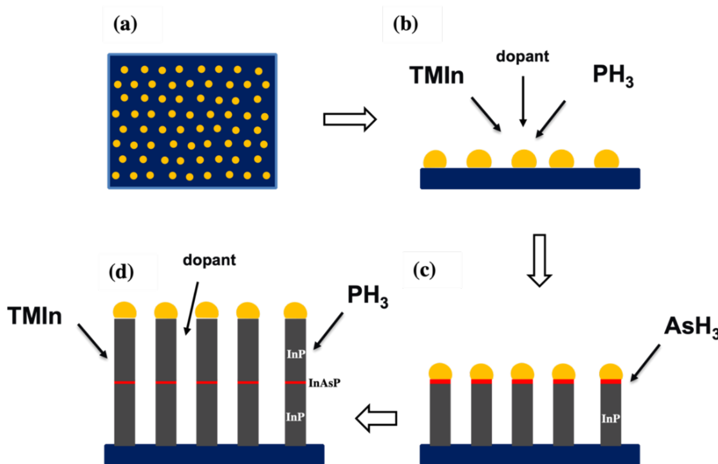

Figure 3.1: Schematics of NW/QDisc growth. a) Highly doped n-type InP (111)B wafer patterned with Au NPs. b) Growth initiated by introducing the precursors into the chamber. c) Switching from growth of InP NWs to InAsP QDiscs and d) switching back to final InP NW growth. Proper dopant precursors (TESn and DEZn) are added during growth of the n^+- segments and i-segment, respectively.

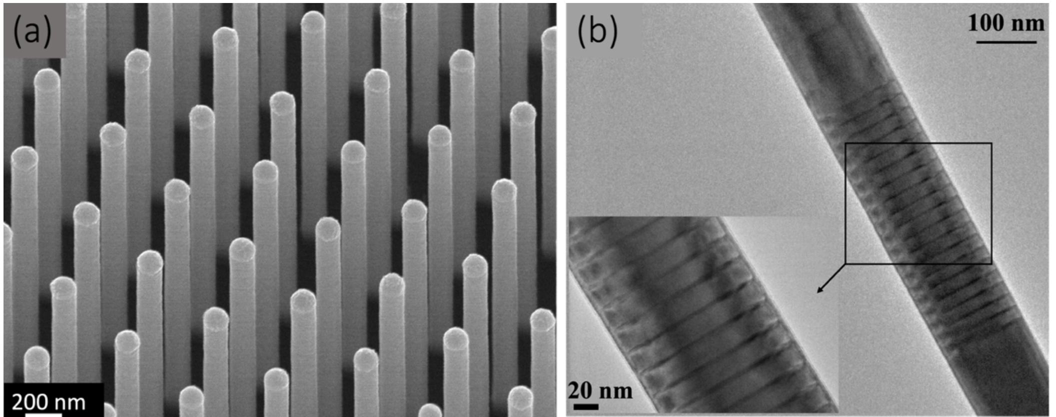

Figure 3.2: a) SEM image of the as-grown NWs with a pitch of 500 nm, a length of 2 µm and a diameter of 135 nm, and b) TEM image of a single NW with a zoomed-in image of QDiscs region in the middle i-segment.

Scanning transmission electron microscopy (STEM) and energy dispersive X-ray (EDX) point-scan profiles recorded along single NWs revealed an average QDisc thickness of 6 nm (for the QDiscs with 1 s growth time) and a composition of 60% As and 40% P ($InAs_{0.6}P_{0.4}$), taken in the middle of the QDiscs. The average separation between the QDiscs was estimated to be around 20 nm, thus excluding any electronic coupling between the QDiscs.

3.2. Device processing

3.2.1. Two-terminal photoconductors

First, a summary of the two-terminal photoconductor fabrication is presented here, followed by details of each step. The processing started with deposition of SiO_x /Al_2O_3 layers around the as-grown NWs, and on the substrate between the NWs using atomic layer deposition (ALD) to isolate the NWs. After planarization by spin coating a layer of photoresist and back-etching until the tips of the NWs were exposed, the next step was to etch the oxide layers and the Au NPs from the tip of the NWs for subsequent top contact formation. Prior to sputtering of the top contact, device areas with various sizes were defined in an ultraviolet lithography (UVL) session and hard baked. Indium tin oxide (ITO) was sputtered on top and around the tips of the bare exposed NWs forming the transparent top contact connecting all NWs in parallel. Finally, a bonding pad was defined on each device in a UVL session followed by evaporation of Ti/Au bi-layer. Figure 3.3 shows an overview of the procedure for processing of two-terminal photoconductors, while a schematic of a fully processed two-terminal device is shown in Fig. 3.4. The steps of processing are presented in Table 1 in the appendix, while each step is described in detail in the following sections.

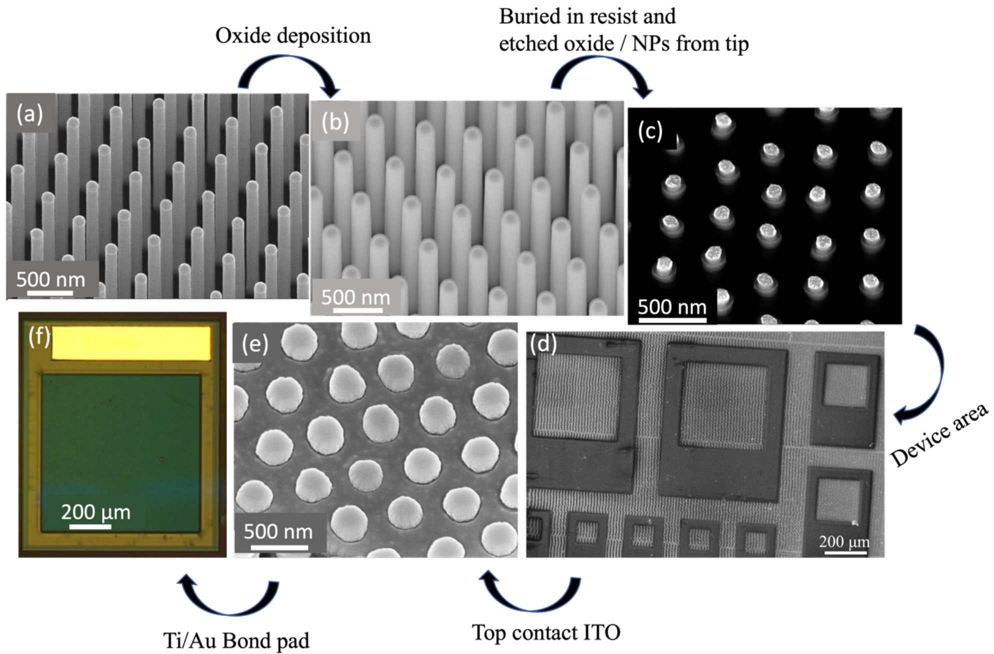

Figure 3.3: An overview of the processing steps for two-terminal NW array photoconductors. a) The as-grown NW array, b) after deposition of oxide layers, c) after burying the NWs in a photoresist layer and etching the oxide and Au NPs from the tips of the NWs, d) after defining the device areas, e) after sputtering of the transparent top contact and f) after definition of the bond pads.

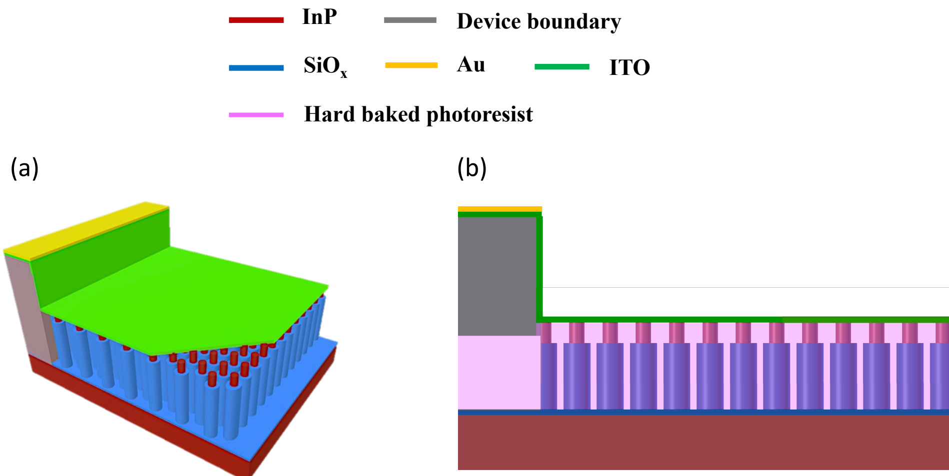

Figure 3.4: a) 3D and b) cross-sectional schematics of a two-terminal photoconductor. The hard-baked photoresist between the top contact and the substrate is left out for clarity in (a), but visible in (b).

For the initial current-voltage (I-V) measurements, the processed sample was glued to a copper disk using silver paint. After choosing the best devices according to the initial I-V characteristics, the sample was mounted on a DIL carrier and the chosen devices were bonded

for more in-depth optoelectronic characterization. Figure 3.5 shows an optical image of a fully processed sample, comprising many two-terminal devices with different sizes.

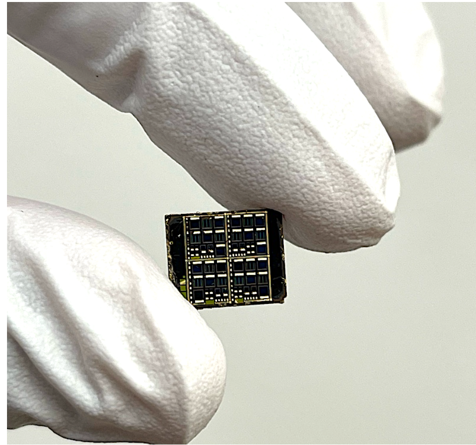

Figure 3.5: Optical image of a fully processed sample with around 100 two-terminal photoconductors with various sizes.

3.2.1.1. Deposition and etching of insulating oxide layers

The first step for two-terminal device processing was deposition of a 30 nm thick SiO_x layer followed by a 5 nm thick Al_2O_3 around the NWs. All oxide depositions were performed in a Savannah ALD using tris(tert-butoxy) silanol and trimethylaluminium (TMA) as the precursor for silicon and aluminum, respectively. The first deposited oxide layer is not pure SiO_2, but SiO_x. The Al_2O_3 was deposited as an adhesive layer to improve the insufficient adhesion of photoresist to SiO_x in the following step. Figure 3.6 shows an SEM image of the NW array after the deposition of the oxide layers.

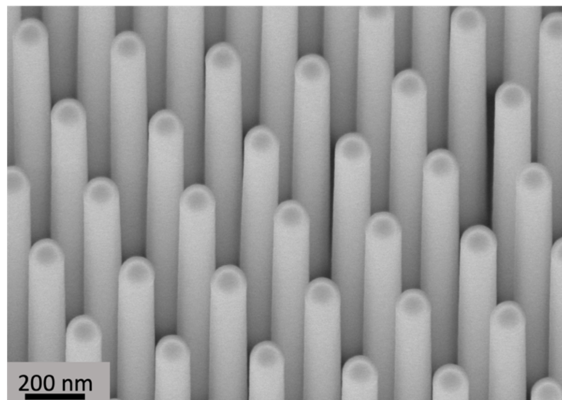

Figure 3.6: SEM image of NWs after deposition of 30 nm SiO_x and 5 nm Al_2O_3 layers around the NWs.

The deposited oxide layers had to be etched from the tips of the NWs to form good ohmic contacts to the subsequently sputtered top ITO contact. This was carried out by burying the NWs in a thick layer of S1818 photoresist (spin coated at 5000 rpm for 60 s), followed by back-

etching using reactive ion etching (RIE) to expose 200 nm of the NW tips. The oxide layers were first etched by stirring the sample slowly in the buffered oxide etchant (BOE) 1:10 for 26 s, followed by a gold etch (KI/I_2 solution) for the same duration to remove the Au NPs. The Au NPs were etched to avoid any absorption/reflection of light in the final device. The etched oxides caused a discontinuity between the NWs and the photoresist which could lead to a non-uniform contact formation during sputtering of the top ITO contact in the subsequent step. Because of this, the resist was removed by acetone, the sample was rinsed, nitrogen dried and covered by a new layer of spun resist, and back etched a second time until the desired length of the NW tips was exposed. Finally, the photoresist was hard baked by placing the sample on a hot plate at room temperature, increasing the temperature to 200 °C and keeping it constant for 15 min. Figure 3.7 shows the exposed bare tips of the NWs after etching the oxide and Au NPs and repeating the spin coating step.

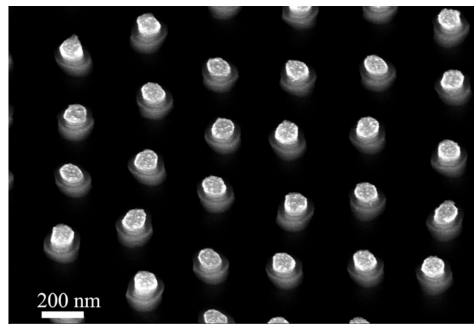

Figure 3.7: SEM image of NW array after etching the oxide layers and Au particles from the tips of the NWs and repeating the spin coating and RIE steps.

3.2.1.2. Definition of device areas

The device areas were defined in a UVL session using an MJB4 mask aligner with a wavelength of 365 nm in constant power (350 W) mode and an intensity of about 22 mW/cm^2. The device areas with various sizes were defined on the sample using a suitable mask. The procedure for UVL is presented in Table 1 in the appendix.

Figure 3.8 shows an SEM image of the sample after defining and hard baking the device areas. The active area in the largest device (not shown here) is 800 × 800 µm^2 (0.64 mm^2). The NWs are standing vertically in hexagonal patterns with a pitch of 500 nm. Each hexagon has a NW in the center and six shared NWs with the six adjacent hexagons which means there are three NWs per 0.65 µm^2, equivalent to around 2.95 million NWs in the largest devices.

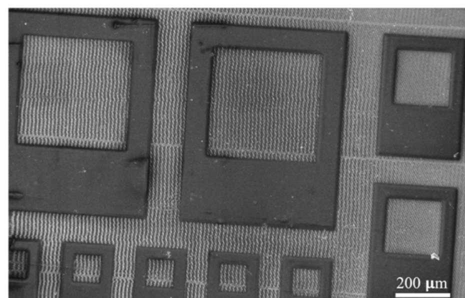

Figure 3.8: The defined and hard-baked device areas with various sizes.

3.2.1.3. Sputtering the top ITO contact

After defining the device areas, the NWs inside the active area of each device needed to be connected in parallel. ITO is a well-known transparent conductive material, highly suitable for this purpose due to its high conductivity and low absorption in a broad wavelength range. An AJA Orion sputter deposition system was used to sputter the ITO contact. Before sputtering, the sample was stirred in H_2SO_4: H_2O (1:10) for 30 s to etch any potential native oxide, rinsed in DI water, dried with N_2 and immediately inserted into the sputtering system. For the photoconductors designed for visible-to-NIR detection, we sputtered 150 nm ITO (resulting in a 30 nm side wall), while we used 50 nm (resulting in a 10 nm side wall) for the LWIR photoconductors. This is due to the strong IR absorption of ITO in the LWIR range. Figure 3.9 shows the NWs inside the device area after depositing ITO as the top contact with two different thickness. After sputtering, the ITO was etched from non-device areas by covering the device areas with a layer of S1813 photoresist in a UVL session. The step-by-step procedure for sputtering and etching the ITO from non-device areas is presented in Table 1 in the appendix.

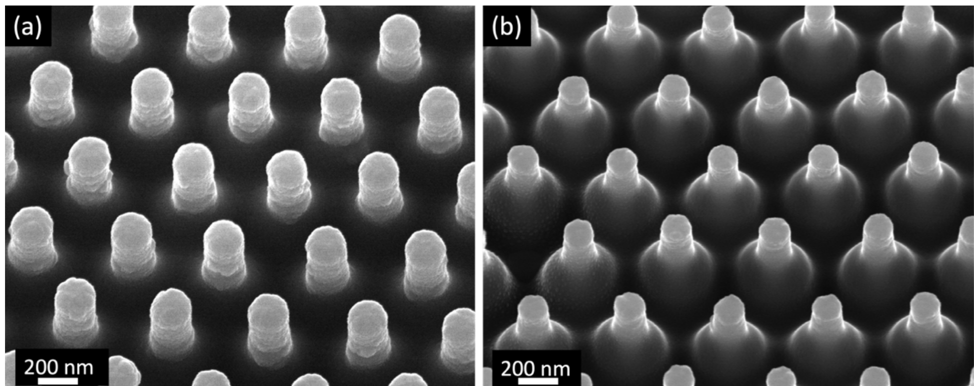

Figure 3.9: The NWs inside the device area after depositing a) 30 nm and b) 10 nm side-wall ITO around the tip of the NWs as the top contact.

3.2.1.4. Definition and evaporation of bond pads

The final step of the two-terminal device processing was defining the bond pads in a UVL session, followed by evaporating 20 nm Ti and 400 nm Au as the bond pads. The step-by-step procedure for UVL and evaporation is presented in Table 1 in the appendix. After UVL, layers of 20 nm Ti and 400 nm Au were evaporated on the sample, then lifted off overnight in acetone and finally the sample was rinsed and dried with nitrogen.

3.2.2. Three-terminal phototransistors

Figures 3.10 (a) and (b) show 3D and cross-sectional schematics of the developed GAA-phototransistor design, with all step-by-step device processing details presented below. The n^+-i- n^+ InP NWs, grown by MOVPE on an n^+-InP (111)B substrate (acting as the source contact), contain 20 InAsP QDiscs in each NW. The transparent global gate contact is fabricated from a buried ITO layer, separated from the substrate by a photoresist layer thick enough to precisely match the vertical position of the individual wrap-gates with the corresponding i-segment of the SiO_x-coated NWs. The top drain ITO contact, separated from the buried gate contact by

another photoresist layer, connects the tips of all NWs in parallel. Finally, the buried gate contact is connected to a bond pad by an etched via hole. Figures 3.10 (c) and (d) show a cross-sectional SEM image of the fully processed phototransistor, and an optical image of the finalized mm^2 detector element.

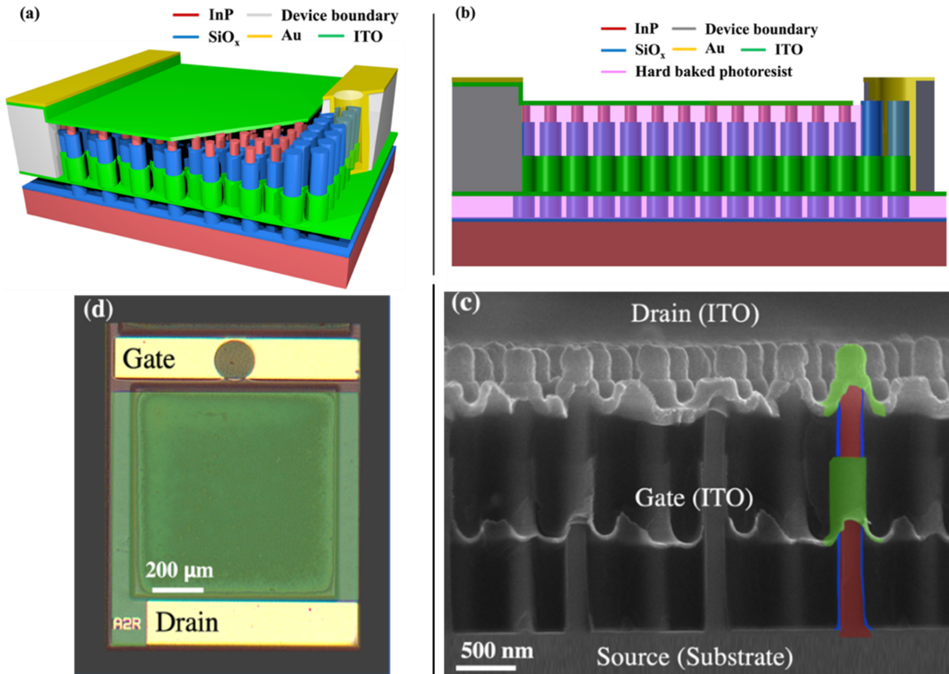

Figure 3.10: a) 3D schematic and b) cross-sectional schematic of the developed GAA-phototransistor with color-coded materials. The hard-baked photoresist, separating the gate from the substrate (source) and top drain contact, is left out for clarity in (a), but visible in (b). c) Cross-sectional SEM image of the fully processed device. For clarity, the SiO_x layer, wrap-gate and drain ITO contacts of a single NW have been color-coded. d) Top-view optical image of the detector. The dark circle in the upper gold gate contact is a via hole extending down to the buried global ITO gate. The top drain ITO contact is color-coded as in (a).

An overview of the processing steps of GAA-phototransistors is shown in Fig. 3.11. Figure 3.11 (a) shows an SEM image of the as-grown NW array. The processing started with deposition of 30 nm SiO_x and 5 nm Al_2O_3 layers using ALD to isolate the NWs. The next step was sputtering of ITO with 30 nm side wall around the i-segments of the oxide-coated NWs to complete the transparent conductive GAA contacts. After defining and hard baking device areas with two bond pads (one for the gate contact and another for the top drain contact) in an UVL session, the oxide layers and the Au particles were etched from the tips of the NWs in the device areas for definition of a low resistance top drain contact (Fig. 3.11 (b)). Fig 3.11 (c) shows the device after sputtering the top contact, connecting all NW tips in parallel, with the rest of the NWs buried in a thick photoresist layer. The cross-sectional SEM image after this step is shown in Fig. 3.11 (d). To access the buried global GAA contact, a via hole was opened in the gate bond pad by a UVL step and etched using RIE until the GAA contact was visible in SEM. Finally, layers of 10 nm Ti and 400 nm Au were evaporated as the contact pads on the pad areas after defining their position in an UVL step (Fig. 3.11 (e)). Figure 3.11 (f) shows the final device mounted and bonded on a DIL carrier. The steps of the three-terminal device processing are summarized in Table 2 in the appendix.

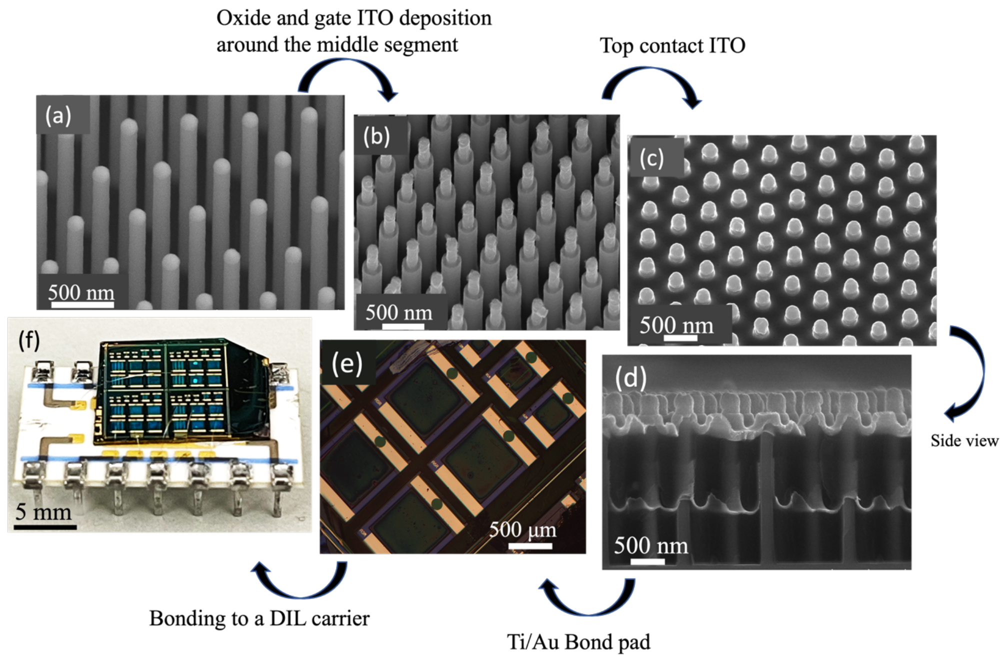

Figure 3.11: (a) to (f). An overview of the processing steps for fabrication of the three-terminal NW array GAA-phototransistors.

3.2.2.1. Deposition of insulating oxide layers

This step was done exactly as explained in Section 3.2.1.1 for the two-terminal devices. Figure 3.12 shows the NW array after deposition of the oxide layers.

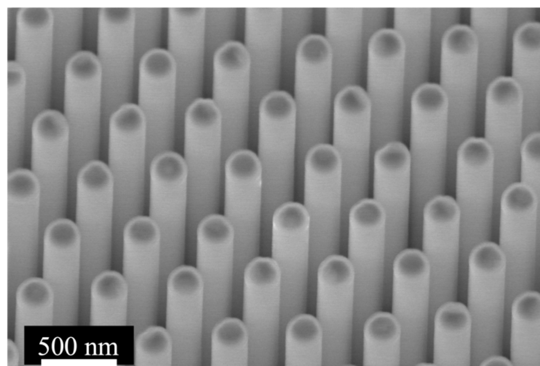

Figure 3.12: SEM image of the NWs after depositing the insulating SiO_x and Al_2O_3 bilayer with thicknesses of 30 nm and 5 nm, respectively.

3.2.2.2. Sputtering the gate ITO layer

Before sputtering the gate ITO layer, it was important to cover the bottom n^+-segments of the NWs. For this, the NWs were buried in S1818 photoresist. This kept the 500 nm long bottom n^+-segments safely buried in resist plus a 100 nm margin inside the i-segments (Fig. 3.13 (a)). After hard baking the resist at 200 °C for 15 min, the gate ITO layer was sputtered with a 30 nm side wall around the NWs using the AJA Orion sputter deposition system discussed in detail in 3.2.1.3. Sputtering of 150 nm ITO resulted in 30 nm NW side wall deposition (Fig. 3.13 (b)). For etching the ITO from the top n^+-segments, the NWs were first buried in S1818 photoresist and then back-etched by RIE until the top 600 nm part of the NWs i.e., the top n^+-segments (500 nm in length) with a 100 nm safety margin were exposed (Fig. 3.13 (c)). The ITO layer was etched from the exposed top parts by stirring the sample slowly in an HCl : H_2O (1:2) solution for 20 s, followed by rinsing in DI water and drying with N_2. Figure 3.13 (d) shows the SEM image of the NW array after etching the ITO from the top n^+-segments. The remaining cap-shaped particles at the tip of the NWs consist of non-etched ITO. As mentioned earlier, 150 nm of ITO sputtering results in a 30 nm NW side wall, but the actual planar deposition at the very tip of the NWs is 150 nm thick and it was therefore not completely etched away. Trying longer etching time in this step could damage the gate as well and because of this, the non-etched ITO was left to be etched in the subsequent steps. The side wall ITO was completely etched from the top n^+-segments in this step. After this step, the resist was removed by stirring the sample in acetone for 2 min followed by rinsing and drying with Nitrogen.

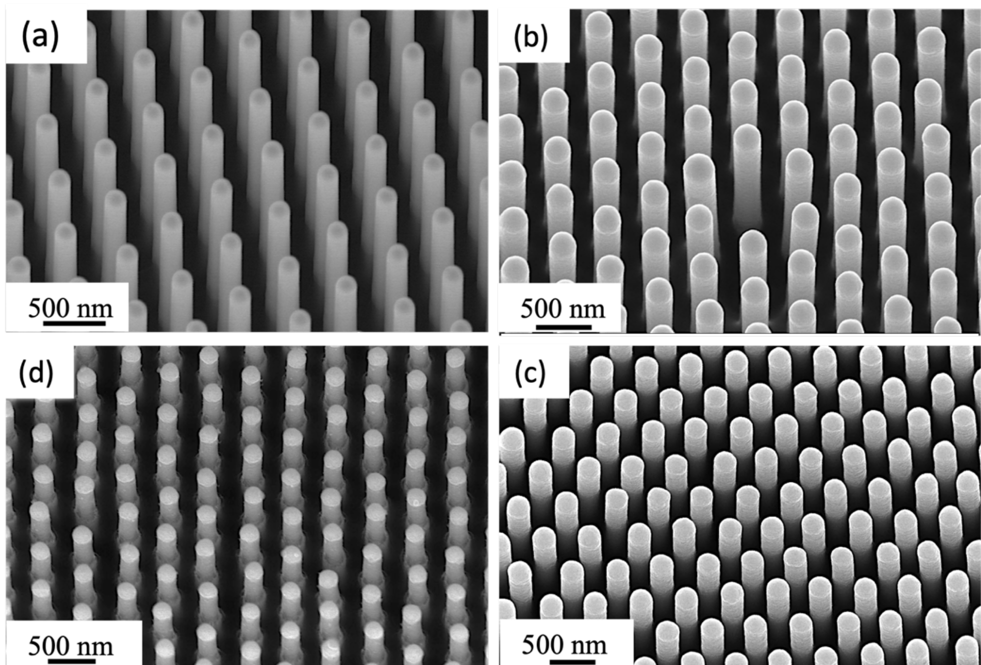

Figure 3.13: SEM images after different processing steps for fabrication of three-terminal NW array GAA-phototransistors. a) NW array with deposited oxide layers and bottom n^+-segments buried in a thick resist, b) NW array after subsequent sputtering of gate ITO with 30 nm side wall, c) exposed top n^+-segments after RIE, while protecting the rest of the NWs with photoresist, and d) NW array after etching the ITO from the top n^+-segments.

3.2.2.3. Definition of device areas

The device areas with various sizes were defined in an UVL step. The steps for UVL are presented in Table 2 in the appendix. Figure 3.14 (a) shows an SEM image of a sample with defined device areas. As noticed, the devices have two bond pads (in contrast to two-terminal devices) used for the ITO gate and ITO top contact, respectively. After hard baking the defined device areas, they were covered with S1818 photoresist in an UVL step, while the non-device areas were left open. The gate ITO was etched from non-device areas using an HCl : H_2O (1:2) solution for 4 min., followed by rinsing in DI water and drying with N_2. This was done to electrically isolate the devices from each other. After the etching process, the photoresist was removed from the device areas using acetone, the sample was rinsed and dried and S1818 photoresist was then once again spun on the sample. The following RIE session exposed 200 nm of the tips of the NWs in the device areas (Fig. 3.14 (b)). This was done to etch the oxide from the tips of the NWs to form good ohmic contacts to the top ITO contact deposited in the next step. Prior to etching the oxide, the residual ITO caps at the tips of the NWs were etched using an HCl : H_2O (1:2) solution for 35 s. After that, the oxide layers and Au NPs were etched from the tips of the NWs with BOE 1:10 for 25 s, followed by a gold etchant (KI/I_2 solution) for 25 s. Following this, the photoresist was washed away with acetone (Fig. 3.14 (c)), the sample was rinsed and dried with N_2, and a new photoresist was spun on the sample with the same recipe to avoid any discontinuity around the NWs because of the etched oxide. Finally, the resist was hard baked at 200 °C for 15 min (Fig. 3.14 (d)). It should be mentioned that the NWs buried in both of the bond pads were protected during the etching steps, and thus had an intact oxide around the top n^+-segments. This was important since the NWs under the gate pad were later used to access to the gate contact with a via hole (Section 3.2.2.5).

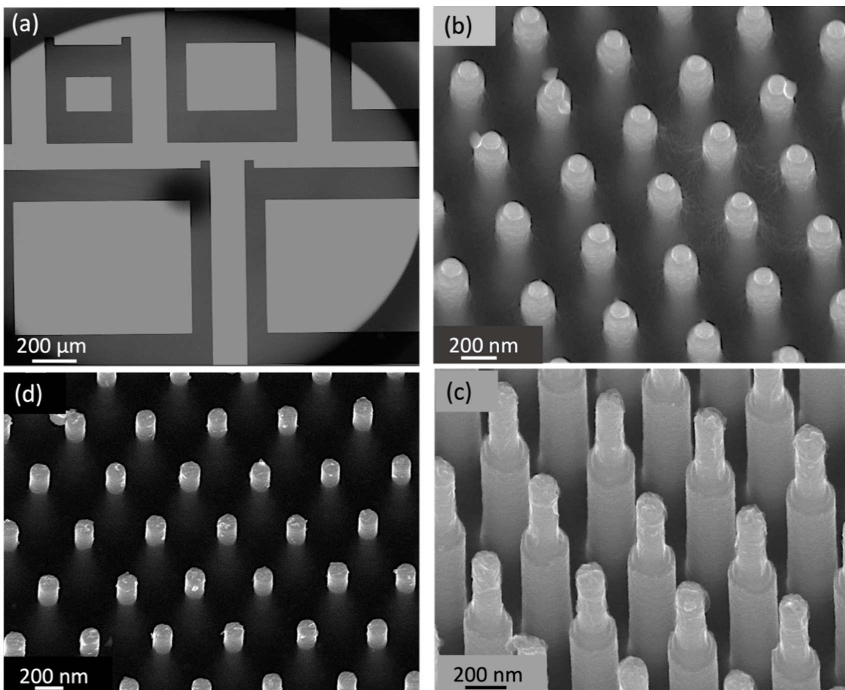

Figure 3.14: SEM images of a sample with a) defined and hard-baked device areas, b) exposed NW tips inside the device area before etching, c) etched residual ITO caps, oxide, and Au NPs from the tips of the NWs and removed resist, and d) after burying the NWs in photoresist and exposing the bare tips.

3.2.2.4. Sputtering the top ITO contact

This step was done exactly as for the two-terminal devices (Section 3.2.1.3), where 150 nm sputtering resulted in a 30 nm NW side wall deposition. Figure 3.15 shows the NWs inside a device area after sputtering the top ITO contact. Since this ITO sputtering connects all the devices together, another UVL step was done to cover the device areas (except the gate pads) and to etch the ITO from the non-device areas (also from the gate pad) using an HCl : H_2O (1:2) solution for 2 min., followed by rinsing in DI water for 1 min. and drying with N_2.

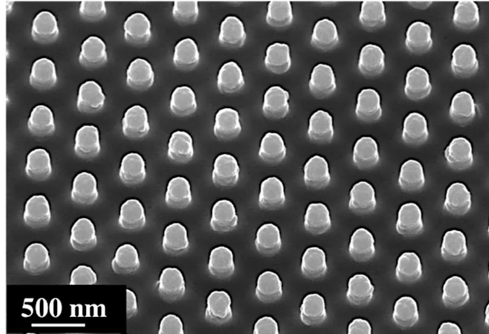

Figure 3.15: SEM image of a sample showing NWs inside a device area after sputtering the top ITO contact.

3.2.2.5. Definition of the via holes

In this step a via hole was opened in the gate pad by an UVL session, followed by a RIE step to access the buried global ITO gate contact. As explained above, the gated NWs still had the oxide around their top n-segments, as they were buried in the pad during the etching step. The UVL procedure for defining the via hole is presented in Table 2 in the appendix. Figure 3.16 shows the defined via hole after development. Finally, the spun resist was removed from the device area using acetone, followed by rinsing and drying the sample with N_2.

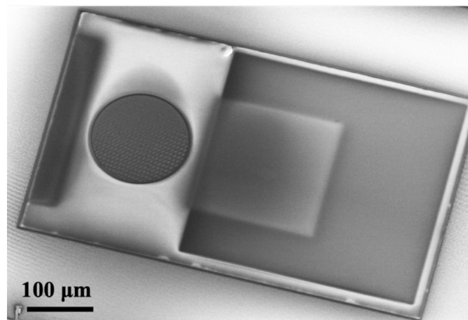

Figure 3.16: Definition of the via hole in the gate pad.

3.2.2.6. Definition and evaporation of bond pads

Similarly to the two-terminal processing scheme, the last step in processing the three-terminal devices was definition and evaporation of bond pads. This step was carried out exactly as explained in Section 3.2.1.4. Figure 3.11 (f) shows an image of the final device mounted on a DIL holder.

4. Characterization techniques

The characterization techniques and tools used in this project are explained in this chapter.

4.1. Probe station measurements

A fully processed two-terminal or three-terminal photodetector sample has 108 and 48 devices, respectively. Thus it is important to choose the best devices with a quick method and focus on them for more in-depth optoelectronic measurements. A probe station system is a quick and useful tool for measuring the I-V characteristics of devices. We used a Cascade 11000B probe station, together with a Keithley 4200-SCS, for the preliminary I-V measurements. The setup is equipped with a 3D micrometer stage, a microscope and four tungsten probes which can conveniently be moved individually with micrometer precision and placed on the selected device's contact pads. The I-V measurements were done in dark and under illumination with light from the microscope lamp. The devices with highest photocurrent and no artifacts in the I-V behavior were chosen for in-depth characterization. Figure 4.1 shows the probe station setup in detail. The setup has the option for measurements in complete darkness. This is done by enclosing the sample in a light-tight box made of eight side walls connected to each other, and a lid mounted on the microscope's lens which could be lowered (Fig. 4.1 (c)). For the measurements under illumination, the light source in the microscope was simply turned on.

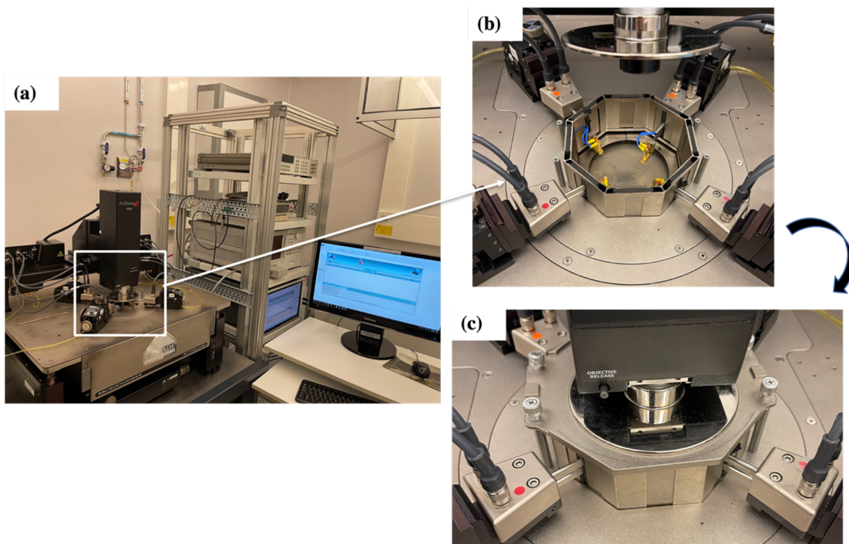

Figure 4.1: Probe station set-up used for primary I-V measurements. a) Complete probe station setup, b) close-up photo of the probes and the light-tight box with the lid attached to the microscope lens in a lifted position, and c) light-tight box after lowering the microscope lens and closing the lid.

4.2. Fourier transform infrared photocurrent spectroscopy

Fourier transform infrared spectroscopy (FTIR) is a very powerful and versatile analytical method which can be used for measuring spectrally-resolved absorption, transmission, and PC. FTIR offers several key advantages, such as very high signal-to-noise ratio and data collection speed due to multiplexed measurements and high optical throughput for a given spectral resolution[89]. The Michelson interferometer is the cornerstone in FTIR spectroscopy. The full

spectrum of light from a broadband source is shone on a beam splitter and split into two beams: one is reflected from a fixed mirror, and the other from a moving mirror. Depending on the moving mirror's exact position, the two beams interfere constructively or destructively when they recombine which results in a modulated beam comprising all wavelengths coded in frequency by the scanning mirror. This modulated beam is focused on the sample (a NW photodetector in our case) where it generates a modulated PC that is amplified by an external current-voltage amplifier. The resulting interferogram is the modulated output voltage versus mirror position, subsequently converted to spectrally-resolved PC using the well-known Fourier transform technique. We used the FTIR model Vertex 80v from Bruker for all spectrally-resolved PC measurements. Figure 4.2 (a) shows a schematic of our FTIR spectrometer, while Fig. 4.2 (b) shows the spectrometer equipped with a dedicated low-noise FTIR pulse tube closed-cycle cryostat (PT-950-FTIR) from Janis/Lake Shore, which was used for low temperature measurements down to about 5 K. In this thesis project, two different light sources and beam splitters were used depending on the wavelength range of interest. A tungsten-halogen lamp was used as the broadband source for NIR measurements along with a CaF_2 beam splitter, while a globar lamp with a KBr beam splitter was used for MIR and LWIR measurements. The modulated PC was amplified using a Keithley 428 current amplifier. Figure 4.3 shows a schematic of the experimental setup and measurement.

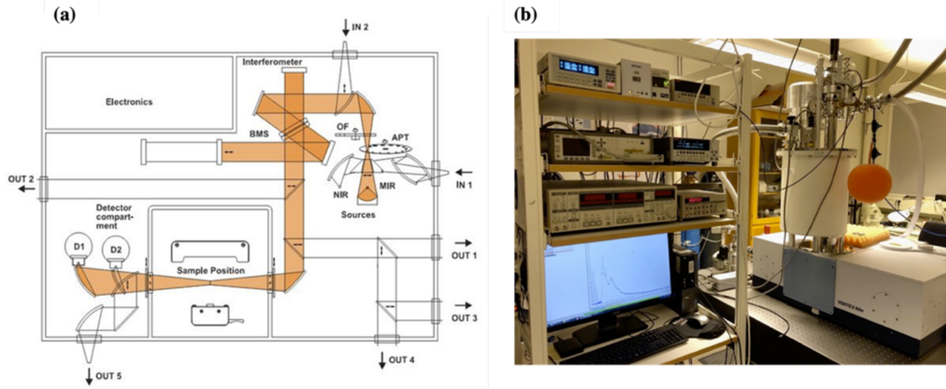

Figure 4.2: a) Schematic of the FTIR spectrometer setup showing the light path involving the internal NIR and MIR sources, beam splitter (BMS) and the sample position where the modulated light reaches the sample mounted inside an integrated cryostat shown in (b). b) Photo of the complete FTIR set-up with integrated cryostat.

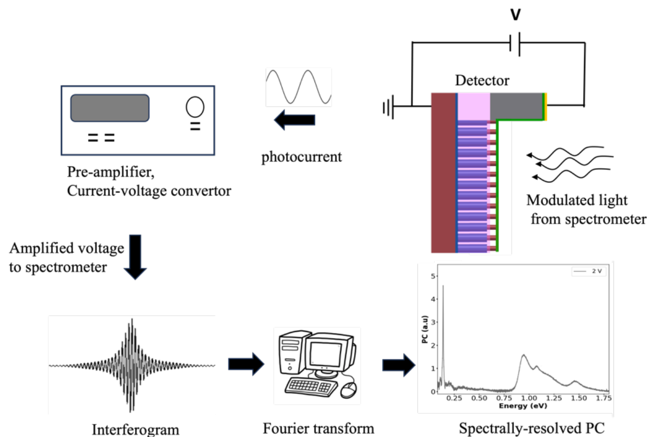

Figure 4.3: Schematic of the experimental setup for the FTIR measurement.

4.3. I-V characterization

Prior to the spectrally-resolved PC measurements described above, in-depth I-V characterization was done with the sample mounted in the cryostat. A Keithley 2636B dual channel source meter was used for collecting the I-Vs in dark and under integrated illumination from the built-in quartz lamp in our FTIR spectrometer. The temperature could be carefully controlled from 300 K down to about 5 K.

4.4. PC measurements by laser

For power-dependent PC measurements using a laser, the internal light source within the FTIR spectrometer was shut off, and an external laser illuminated the sample. To enable this, the sample was positioned towards one of the input windows of the FTIR spectrometer, while the laser was positioned in front of the windows to allow light entry into the spectrometer and onto the sample. To regulate the laser output power to extremely low levels, beyond what could be achieved by simply adjusting the laser diode current, a variable light attenuator was inserted between the laser and the spectrometer, enabling precise control over the desired power level. Modulation of the laser light was achieved either through a wave generator or by introducing an optical chopper between the laser and the sample. When measuring PC at high laser powers, the generated signal could be amplified using a preamp and recorded using an oscilloscope. Conversely, at very low laser powers, a lock-in technique was employed to measure the PC, allowing for sensitive detection and accurate characterization of the sample's response.

5. Photogating effect in two-terminal photoconductors

The photogating effect in NW photodetectors was briefly discussed in section 2.6.4. The discussion below summarizes our investigation of a novel photogating mechanism, hitherto unknown for InP/InAsP NWs, and its effect on the optoelectronic behavior of two-terminal photoconductors based on InP NWs with axially embedded InAsP QDiscs.

5.1. I-V characteristics

The typical I-V characteristics of the two-terminal n^+-i-n^+ photoconductors in dark and under illumination, measured by the Keithley 2636B source meter, are shown in Fig. 5.1. For illumination we used the internal quartz lamp (350 nm – 1µm) in the FTIR spectrometer, as described above. There are two main reasons for the observed low dark current: i) compensation of unintentional n-doping in the i-segment by adding Zn acceptors during growth and ii) electrostatic repulsion from the trapped negative charge at the NW/SiO_x interface, which depletes the NWs radially and increases the potential barrier between the n^+- and i-segments in the NWs. To investigate the detailed transport mechanisms, in-depth simulations were performed as part of this thesis project. All calculations were made using the commercial device simulator *Synopsys Sentaurus*, which solves the continuity equations for electrons and holes, including drift-diffusion currents, together with the Poisson equation. The simulations were performed using a real device model based on genuine device features such as NW dimensions, and the thickness, composition and separation of the QDiscs as measured by TEM characterization. As can be seen in Fig. 5.1, there is a very good agreement between the experimental data and the simulations. In the simulations, two dominant NW/SiO_x interface traps below the conduction band of the InP NW and InAsP QDiscs were found which cause the observed photogating effect. The large effect of the traps on the I-V characteristics can indeed be noticed. The orange trace shows the simulated total current (dark current plus PC) in the absence of traps at the given power density. Interestingly, by comparing to a simulation in dark (not shown), it is evident that the PC without traps is negligible compared to the dark current.

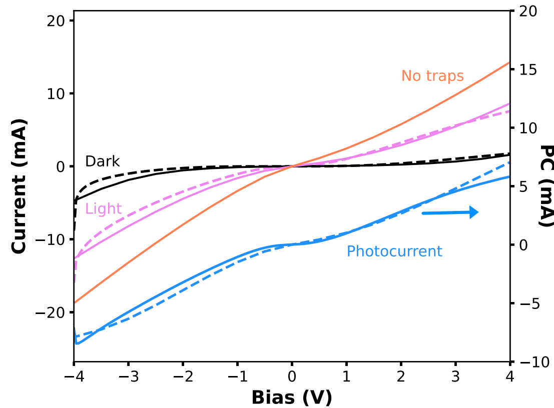

Figure 5.1: I-V characteristics with and without illumination from a broadband quartz lamp. Left axis shows the detector current (in dark: black, under illumination: pink), while the right axis shows the PC (blue), i.e., the detector current under illumination subtracted by the dark current. The dashed lines are experimental data, while the solid lines are simulations.

5.2. Spectrally-resolved PC and responsivity

Figure 5.2 (a) shows the spectrally-resolved PC in the photodetector for two different applied biases under illumination from the quartz lamp, as measured with the FTIR spectrometer. The spectrally-resolved responsivity of the detector (Fig. 5.2 (b)), was calculated from the spectrally-resolved PC. For this conversion, we used NIST-calibrated Si **(**FDS100-CAL**)** and Ge **(**FDG03-CAL**)** photodiodes purchased from Thorlabs. We attribute the responsivity between 0.7 eV and 1.3 eV to interband transitions between the confined energy levels in the QDiscs, while the signal between 1.3 eV and 2.5 eV is attributed to interband transitions in the InP NWs. The peak at around 1.25 eV reflects an interband transition in the QDiscs to a bound state close to the band edge of InP, which leads to a significant PC (and responsivity) increase due to an efficient thermal excitation of the electrons from this bound excited state to the conduction band of the InP NW. The increased PC and responsivity at higher bias is due to a stronger electric field in the i-segment and more efficient extraction of the photogenerated carriers.

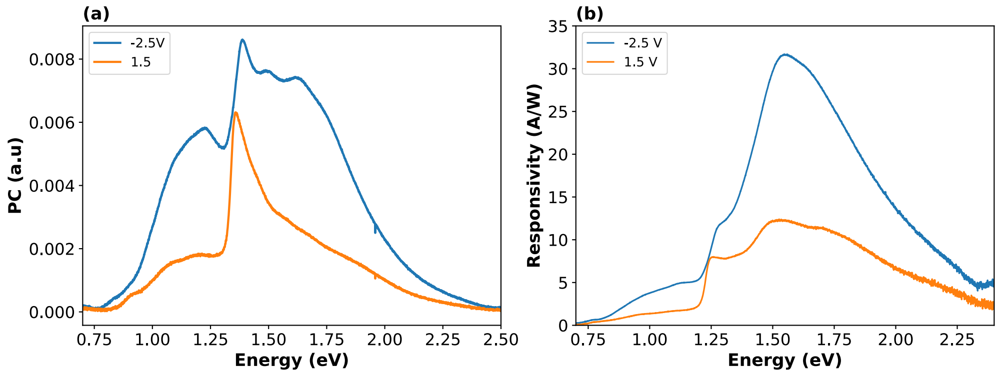

Figure 5.2: Spectrally-resolved a) PC and b) responsivity (converted from corresponding PC data in (a)), measured by FTIR PC spectroscopy.

5.3. Power-dependent responsivity

The PC of the detector was also measured as the laser power was varied. For these measurements, we chose a laser operating at 980 nm, with a photon energy below the bandgap of InP, so as to selectively excite only the QDiscs. The PC and corresponding responsivity (calculated by Eq. 2.17) and gain (calculated by Eq. 2.19 by considering 100% internal quantum efficiency and a wavelength of 980 nm) versus optical power are shown in Fig. 5.3 (a) and Fig. 5.3 (b), respectively. The highly non-linear optical response is attributed to the trap-assisted photogating mechanism. The responsivity amounts to 250 A/W (gain of about 320) @ 20 nW at a bias of 3.5 V, which reduces to 0.2 A/W (gain of about 0.2) @ 20 mW.

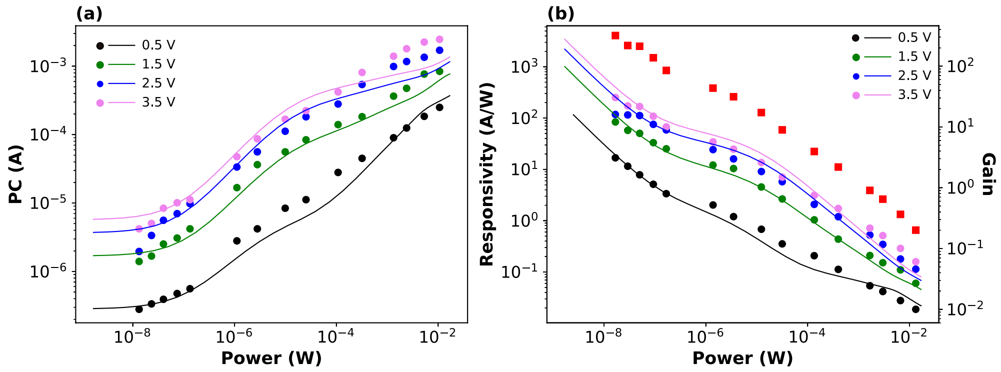

Figure 5.3: a) Measured (dots) and calculated (solid lines) PC for 980 nm laser excitation versus optical power and bias. The experimental data were collected by a standard lock-in technique. b) Extracted responsivity from data in (a) (left axis) and corresponding gain (red squares, right axis) at a bias of 3.5 V.

The high responsivity and corresponding high gain shown in Fig. 5.3 (b) stem from the mentioned photogating effect. The acceptor states at the NW/SiO_x interface are filled with electrons in dark conditions which creates a radial electrostatic force, similar to the gate effect in a MOSFET. This repulsive force pushes the electrons to the center of the NWs and QDiscs, while depleting the surface, as shown in Fig. 5.4 (a). This works in favor of a low dark current since it leads to an increased blocking barrier for electrons between the n^+- and i-segments in the NWs (Fig. 5.4 (b)). Under 980 nm illumination, the photogenerated holes are attracted to the negatively charged electrons trapped at the interface and recombine. This neutralization of the acceptors lowers the blocking barrier, which leads to a strongly enhanced electron current injection which increases the electron density in the i-segment by two orders of magnitude. The radial gating voltage along the i-segment after illumination with 980 nm is shown in the bottom plot of Fig. 5.4 (b), where the maximum voltage change ΔV_g reaches 0.34 V @1.5 V bias and 4.4 mW/cm^2 power density.

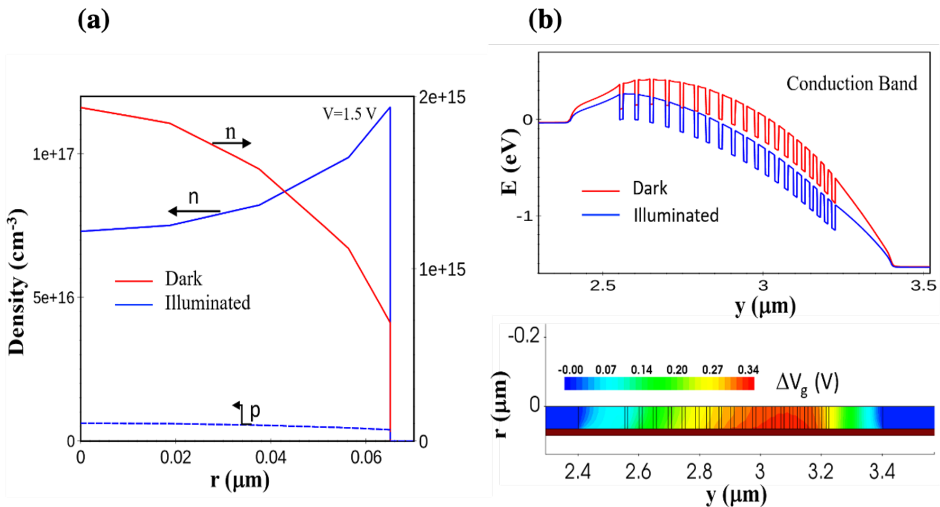

Figure 5.4: a) Radial carrier density in the second QDisc from the left in (b) in dark and under irradiation (980 nm, 4.4 mW/cm^2). b) Calculated band diagram along the center of a NW with 20 QDiscs at a bias of 1.5 V in dark and under illumination. The color plot below shows the corresponding radial variation in gating potential along the i-segment (QDisc region) of a NW. The center of the NW is at 0, while the thick brown horizontal line marks the SiO_x cap layer.

The electronic properties of the interface traps were investigated in more detail by studying the power dependence of the detector's total current. The total current (dark current plus PC) versus optical power is presented in Fig. 5.5 for four different situations. In general, the PC versus optical power relation can be expressed as $I_{PC} \sim P^{\alpha}$, where $\alpha<1$ signals the presence of a photogating effect in contrast to the case of $\alpha=1$ for a standard photoconductor[87]. From the experimental data (red dots), two different slopes can be noticed. A slope of $\alpha = 0.7$ at power levels around 10^{-6} W, and another slope of $\alpha=0.45$ at 10^{-3} W indicate contributions from at least two different acceptor traps to the photogating mechanism. The colored lines in Fig. 5.5 show simulations for four cases: without traps, traps at 140 meV, traps at 190 meV below the conduction band edge and traps at both levels at the same time. In the case without traps, there is no observed photogating effect. The detector has a high dark current, keeping the total current constant even for increasing optical power. Only at the highest laser powers does the excess carrier density lead to a significant PC. Adding interface acceptor traps reduces the dark current due to radial depletion, as discussed above. According to standard Shockley-Read-Hall theory, the recombination efficiency depends on the trap energy, with deeper traps (i.e., closer to mid-bandgap) having the highest recombination rate. Therefore, at lower optical power levels (i.e., low hole densities), the traps at 190 meV below the conduction band edge are dominant in the photogating effect, while the traps at 140 meV induce a gating signature from about 10^{-5} W. Both trap levels create a distinct slope in the current versus laser power dependence. When the gating effect from both traps are considered, a remarkably good agreement between the experimental data and simulations over six orders of magnitude in optical power is achieved.

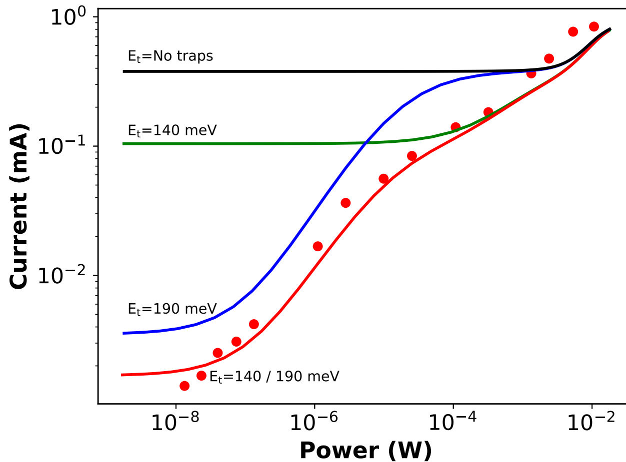

Figure 5.5: Total detector current (PC plus dark current) versus optical power at 980 nm excitation and 1.5 V bias. Red dots show measured data. The solid, colored lines show the simulated total current without traps (black), when introducing a trap level E_t at 140 meV (green) or 190 meV (blue) below the conduction band and, when including both traps (red).

5.4. Frequency response

Finally, the photoconductor was illuminated by a modulated output of the 980 nm laser to investigate the frequency response. This was done by applying a sinusoidal input signal to the laser driver unit. The recorded modulated PC is shown in Fig. 5.6 (a) which was measured using AC laser excitation with an amplitude of 0.4 mW oscillating at 100 kHz around a DC power level of 2.5 mW. Figure 5.6 (b) shows the normalized PC amplitude versus modulation frequency f, e.g., $PC(f) / PC(f_0)$, with f_0=10 Hz, plotted together with the simulated small-signal

response with and without the interface traps. Since no parasitic device effects were considered in the simulations, the cut-off frequency for the case with traps is determined by the lifetime of the trapped carriers, which amounts to about 20 µs (cut-off at 50 kHz), while the device's bandwidth extends to 100 MHz without traps. The cut-off frequency obtained from the experimental data amounts to around 10 kHz. The PC signal decreases roughly linearly with log (f) up to about 100 kHz and the PC response at higher frequencies is strongly affected by the cut-off frequency of about 175 kHz of the current amplifier (Keithley 428) in addition to modulation limitations of the laser driver unit (Thorlabs LDC 205C). From this plot can be estimated that the maximum operating frequency of the detector at least stretches into the MHz region.

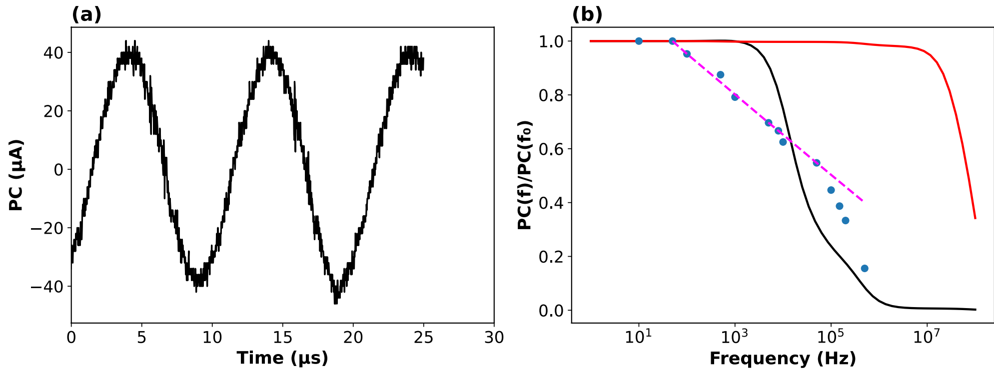

Figure 5.6: a) Recorded PC signal with modulated laser excitation at 100 kHz and 0.9 V applied bias. b) Normalized frequency response of the detector (blue dots), plotted together with the simulated response without traps (solid red trace) and including the two traps at 140 meV and 190 meV below the conduction band (solid black trace), respectively. The pink dashed line is drawn as a guide for the eye.

6. LWIR response of two-terminal photodetectors

In this chapter, the LWIR response of the two-terminal photodetectors at low temperature is discussed along with the corresponding simulations. An ultra-thin top ITO contact, 10 nm side wall around the tip of the NWs, combined with the novel photogating mechanism facilitates an improved LWIR normal incidence sensitivity in contrast to traditional planar QWIPs. The electronic structure of the QDiscs, including strain and defect-induced photogating effects, and optical transition matrix elements were calculated by an 8-band **k·p** simulation along with solving drift-diffusion equations to unravel the physics behind the generation of narrow linewidth intersubband signals observed from the QDiscs.

6.1. I-V characteristics

I-V characteristics of a 0.64 mm^2 two-terminal photoconductor in dark and under illumination at 300 K are shown in Figure 6.1 (a). The total photodetector current, including both dark current and PC, was measured under illumination from the built-in quartz lamp in the evacuated (0.1 mbar) FTIR spectrometer. Similar to the device discussed in the previous chapter, we observed a very small dark current which again is attributed to the successful compensation doping using Zn in the i-segment of the NWs and also to the acceptor-like trap states located at the interface between the NW and the SiO_x isolation shell. In dark, these traps are filled with electrons which in effect pushes away the electrons to the center of the NWs and reduces the radial width of the electron channel in the NWs. Under illumination, the photogenerated holes are attracted to the interface where they recombine with the negatively charged traps which opens the electron channel. This photogating mechanism leads to the very high responsivity and gain discussed in depth in section 2.6.4, and also in the previous chapter dealing with our two-terminal photodetectors operated at room temperature. The cryostat integrated with the FTIR, shown in Fig. 4.2 (b), was used to measure the dark current in the photodetector as a function of temperature, cooling down from 300 K. A stainless-steel cap was used to cover and protect the sample from any dark current generation by black body radiation from the surrounding spectrometer. Figure 6.1 (b) shows that the dark current strongly decreases with temperature to the measurement limit of our system (around10 fA) already at 200 K, which shows the strong combined effect of the Zn doping in the i-segment and photogating.

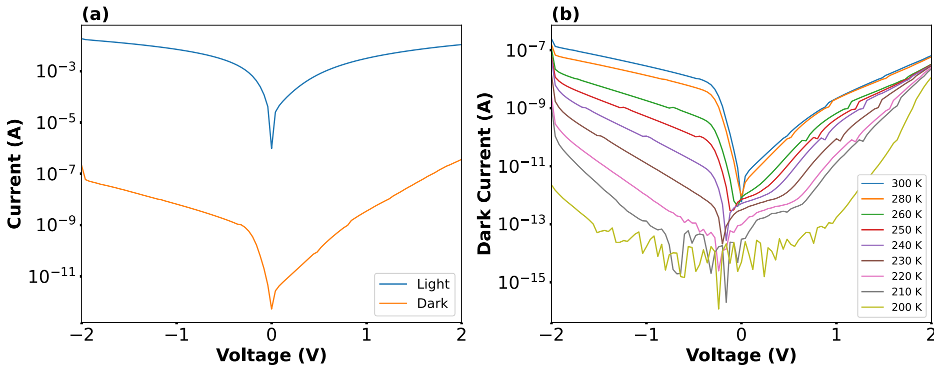

Figure 6.1: a) I-V characteristics in dark and under illumination at 300 K. b) Temperature dependence of the dark current.

6.2. Spectrally-resolved responsivity

Fig. 6.2 (a) shows the spectrally-resolved responsivity of the photodetector at room temperature, converted from PC measurements using calibrated photodiodes as explained before. Clearly, the responsivity is strongly increased at larger biases which can be explained by more efficient photocarrier extraction. Figure 6.2 (b) shows the spectrally-resolved responsivity at 6 K. The spectral features observed below the bandgap of InP in the inset plots of both Figs. 2 (a) and 2 (b) are attributed to interband transitions in the InAsP QDiscs, in excellent agreement with the simulations discussed below.

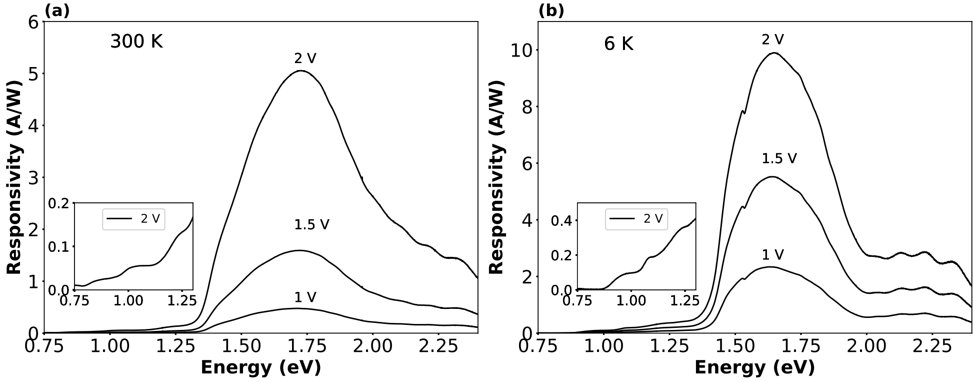

Figure 6.2: Spectrally-resolved responsivity at a) 300 K and b) 6 K at three different biases. The spectral features observed in the inset plots of both (a) and (b) reflect interband transitions in the InAsP QDiscs.

To be able to measure the spectrally-resolved PC for LWIR at low temperature, the built-in globar light source in our spectrometer was used which offers a much higher photon flux in the LWIR range compared to the quartz lamp. In Fig. 6.3 (a), not only the above-mentioned interband peaks are visible, but also a sharp peak at around 135 meV (9.2 μm) is noticeable which reflects an intersubband transition between the ground state and the first excited state in the conduction band of the QDiscs. It can be noticed that the shape and magnitude of the interband peaks in Fig. 6.3 (a) are not same as in Fig. 6.2 (b), which is due to the unnormalized spectrum in Fig. 6.3 (a) with respect to photon flux. The spectral distribution of the photon flux from the globar light source is quite different from that of the quartz lamp. In addition, the beam splitter in the FTIR was changed from CaF_2 to KBr when switching to the globar light source to avoid LWIR absorption by the beam splitter which also affects the photon flux impinging on the sample. For better understanding, the band diagram and the possible optical transitions are shown in the inset of Fig. 6.3 (a). Figure 6.3 (b) shows a zoomed-in part of the spectrum in Fig. 3(a), focusing on the MWIR-LWIR range, now properly normalized to the photon flux. This normalization in MIR-LWIR region was performed by measuring the photon flux with a built-in pyroelectric deuterated L-alanine doped triglycene sulphate (DLaTGS) detector.

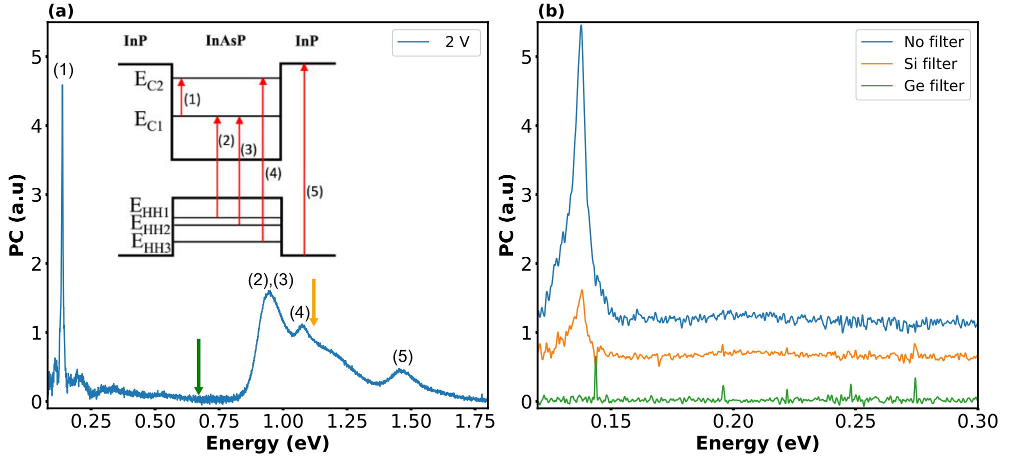

Figure 6.3: a) Spectrally-resolved normal incidence PC at 6 K recorded in a broad spectral range, revealing both intersubband and interband PC. The interband transitions 2 and 3 cannot be resolved separately here. b) Zoomed-in spectra showing the intersubband PC, normalized with respect to the photon flux. The band gap energies for the Ge and Si filters used are indicated as green and orange arrows in (a).

Similar spectrally-resolved measurements using the globar light source were carried out using Ge and Si filters placed in front of the sample, blocking the interband light. The spectra are shown in Fig. 6.3 (b). Evidently, the intersubband transition completely disappear by using the Ge filter, while the Si filter strongly reduces the intersubband peak. To explain the physics behind these phenomena, one needs to relate the transmission of the filters with the optical transitions in the detector. The Ge filter with a bandgap of 0.66 eV (shown by a green arrow in 6.3 (a)) blocks all interband excitations in both QDiscs and NWs which interestingly results in a completely lost intersubband PC signal. On the other hand, using a Si filter (bandgap indicated by the orange arrow in 6.3 (a)) only blocks all excitations in InP, resulting in a reduced intersubband signal. The Ge and Si filters have around 55 % and 30% transmission at 9 µm, respectively, so the intersubband signal is expected to be reduced by only a factor of two to three. This reveals that there is a clear relation between the sharp intersubband and the interband transitions, and that the interband pumping process is crucial for observing an intersubband signal. This can be explained by the photogating effect. Under interband illumination the conduction channel in the NWs gets wider and more electrons are injected into the i-segment of the NWs and captured into the ground state of the QDiscs. Additionally, optical interband transitions in the QDiscs can directly feed the ground state of the QDiscs with electrons. The increased electron population in the QDiscs, combined with the developed ultrathin ITO top contact discussed below, leads to a strongly enhanced intersubband PC.

6.3. Electronic structure of embedded quantum discs

An 8-band $\mathbf{k}\cdot\mathbf{p}$ simulation along with a drift-diffusion transport solver at T = 300 K was used to calculated and analyze the electronic structure of a symmetric 2D NW/QDisc structure with only 6 QDiscs, shown in Fig. 6.4 (a). The reason for choosing 6 QDiscs in the simulation instead of 20 was that simulating a larger number of QDiscs showed unstable numerical convergence in the strongly depleted intrinsic region. A 3D simulation at low temperature of the full structure was beyond the computational capabilities. To ensure that the simulation results were relevant to the real case, the reduced physical model was scaled in a consistent way to ensure that all extracted physical parameters were accurate and directly comparable to

the experimental data. Figure 6.4 (a) shows the radial trace of the calculated strain tensor for the developed model. The QDiscs are under compressive strain, which varies in the radial direction. In contrast to a biaxial approximation for an infinite layered system, there is strain release towards the NW surface. Moreover, the InP barriers between the QDiscs exhibit tensile strain (approx. 0.5 %). Both effects lead to a reduction of total strain energy, and therefore significantly improved crystal quality in the nanostructure. The **k·p** method is applied to each of the six individual QDiscs along three vertical cuts through the structure at different radii (r = 1 nm, 30 nm, and 60 nm), indicated by the three arrows at the top of the schematic of the NW in Fig. 6.4 (a). Thus, a total of 18 **k·p** problems are solved for the complete system. Figure 6.4 (b) displays the conduction band profile along a NW at V= 0 V in the NW center and close to the NW surface, respectively. Due to the strain-induced band edge shifts, and the electron traps at the NW/oxide interface (discussed briefly above), the conduction band is warped, leading to a deeper radial confinement potential at the NW surface.

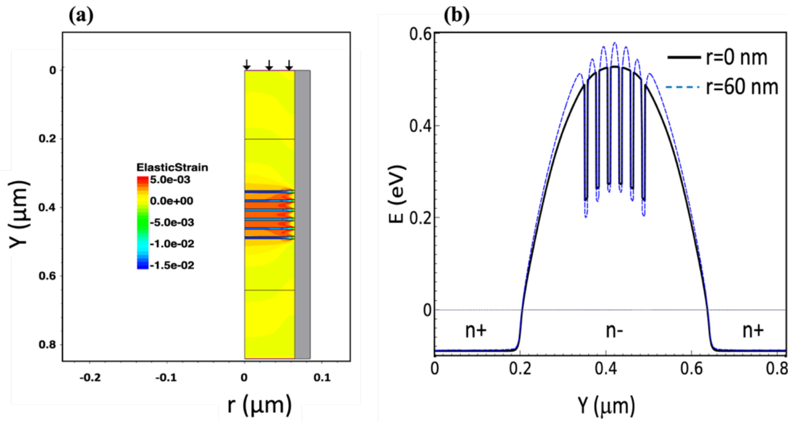

Figure 6.4: a) Calculated radial trace of the strain tensor for the developed NW model; the QDiscs show compressive strain, and the barriers tensile strain. The arrows at the top indicate the radial positions where subband calculations have been performed for the QDiscs. The grey-colored stripe to the right indicates the SiO_x shell around the NW and b) conduction band profile at 0 V bias along the NW center (r=0 nm, solid black line) and close to the NW surface (r=60 nm, dashed blue line)

The subband dispersions from the **k·p** calculation are shown in Fig. 6.5. Also, the polarization-resolved matrix elements for interband and intersubband transitions have been extracted. For this calculation, a voltage V = 0.8 V at the contacts was chosen, which introduces an electric field across the QDiscs in the reduced simulation structure similar to that at V = 2.0 V applied in the experiments. Matrix elements for interband transitions with non-zero entries are the following: for in-plane polarization neglecting excitonic shifts, $E_{C1} - E_{HH1}$ (0.90 eV), $E_{C1} - E_{HH2}$ (0.95 eV), and $E_{C2} - E_{HH3}$ (1.10 eV). In an ideal QW, the transitions involving states with different parity would not be allowed. However, according to our previous studies on similar devices, our detectors exhibit a photonic crystal effect, which gives rise to a longitudinal electric field component along the NWs, enabling the intersubband transition possible[11]. These calculated transition energies are in good agreement with the experimental data shown in Figs. 6.2 (a) and 6.3 (a). For a direct comparison with the low-temperature data, a thermal Varshni-type blue-shift of 120 meV should be added[90]. The calculated intersubband transition matrix element between E_{C1} and E_{C2} is due to the non-zero entries of matrix elements only for the out-of plane polarization of the incoming radiation. The calculated transition energy of 130 meV is in good agreement with the experimental results in Fig. 6.3. This calculated

intersubband energy needs to be red shifted for a direct comparison with the low-temperate experimental data; a thermal red shift for intersubband transitions of 8 meV has been reported for cooling down from 300 K to 4 K[91].

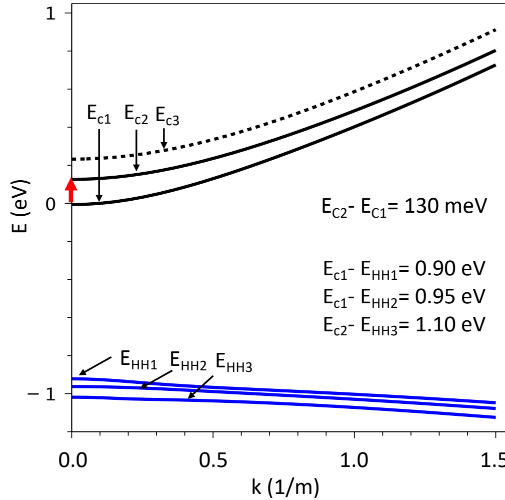

Figure 6.5: Band dispersion relations from an 8-band **k·p**-simulation of a single QDisc, showing the relevant interband and intersubband transitions also discussed in Figs. 6.2 and 6.3. The intersubband transition from E_{C1} to E_{C2} is shown with a red arrow at k=0.

Conventionally, the selection rules for QWs, similar to the present QDiscs, require out-of plane polarization for intersubband transitions in contrast to the in-plane conditions in our experiments. In the first report by us on intersubband transitions in QDiscs[11], we proposed that our NW detectors display a photonic crystal effect which results in a longitudinal electric field component along the NWs. Interestingly, the intersubband PC decreases when the sample is rotated from normal incidence conditions, in contrast to the mentioned selection rules for QWs. This is attributed to a decreasing electron concentration in the ground state of the QDiscs under tilted conditions due to the decreased interband pumping and photogating effect, as discussed above. Simulations show that the electron density in the QDiscs in dark at V = 0.8 V and T = 300 K (which creates a similar bias as 2 V in the experiments) is only about 2×10^{15} cm^{-3}. Under interband excitation, this concentration increases by at least two orders of magnitude. The variation of the intersubband transition energy in our simulations due to inhomogeneities in the structure (local electric field, strain, and charge density) is within 5 meV, which in part explains the narrow FWHM of about 5 meV in the experiments (in fact, similar to typical high-quality planar quantum well IR photodetectors[92]). Interestingly, the electron energy level E_{C3} in Fig. 6.5 only occurs in the vicinity of the NW surface, where the QDisc potential is warped resulting in a deeper confinement potential (see Fig. 6.4 (b)) and an additional bound electron state.

6.4. Characterization of ultra-thin ITO layers

Improved processing, especially the development of an ultra-thin ITO top contact, underlies the significantly improved signal-to-noise ratio (SNR) of the sharp intersubband peak. ITO shows strong absorption in the LWIR region wherefore it is typically not used as transparent contacts in this spectral range. We investigated the transmission of ITO layers with various thickness, sputtered onto an undoped silicon substrate, as shown in Fig. 6.6 (a). Clearly, 150 nm

of ITO, which was used in our previous processing, exhibits a drastic absorption in the LWIR range. In the current processing scheme, we have instead used 50 nm thick ITO top contact layers with almost three times higher transmission at around 9 µm. This nominal 50 nm sputtering results in merely 10 nm thick side wall deposition of ITO around the tips of the NWs as can be seen in Fig. 3.9 (b). The sheet resistance of this thin ITO layer is another important factor for the performance of the detector. We used the familiar four-point probe technique to measure the sheet resistance of sputtered ITO layers with different thicknesses. The well-known textbook formula $R_s = 4.53236\ \frac{\Delta V}{I}$ was used to calculate the sheet resistance, where I is the applied current to the outer two probes and ΔV is the measured voltage between the two inner probes. Figure 6.6 (b) shows the sheet resistance of ITO layers versus thickness. The sheet resistance of the ITO layer increases from 55 Ω/sq for 150 nm to 220 Ω/sq and 2500 Ω/sq for 50 nm and 10 nm thickness, respectively.

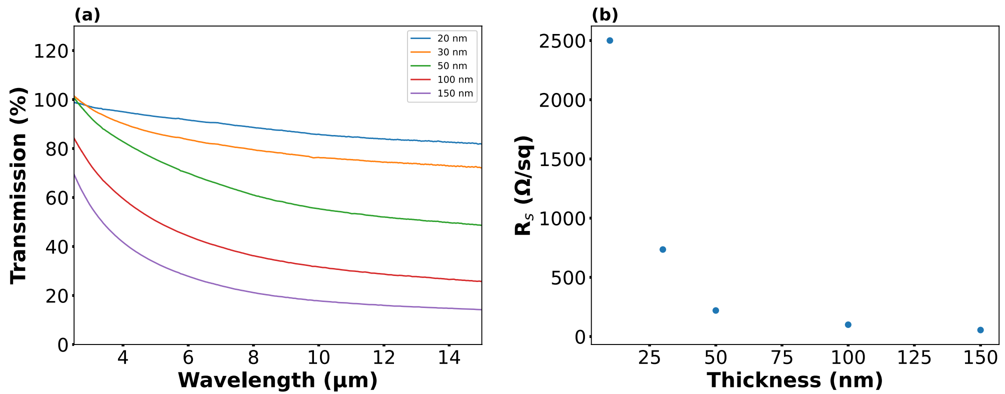

Figure 6.6: a) Transmission spectra of ITO layers with different thickness deposited on an undoped silicon substrate. The spectra are normalized to the transmission of the bare substrate. b) Sheet resistance of ITO versus thickness, measured by the four-probe technique.

7. Room-temperature GAA-phototransistors

This chapter presents and discusses the findings of thorough electrical and optical characterization conducted on the three-terminal GAA-phototransistor. Additionally, extensive simulations were performed to enhance our comprehension of the complex optoelectronic behaviors. The main conclusions from the simulations are also added to this chapter.

7.1. I-V characterization

To investigate the impact of the gate on the performance of the three-terminal devices, we analyzed the output characteristics of the phototransistor both in dark (Fig. 7.1 (a)) and under illumination (Fig. 7.1 (b)). The drain-source photocurrent (PC_{DS}) in (b) was obtained by subtracting the dark current from the total phototransistor current measured under illumination using our FTIR spectrometer's built-in halogen-tungsten lamp. The transistor behavior is clearly observed with a gate-controlled dark current (I_{DS}) and PC_{DS} extending over several orders of magnitude. To comprehend the asymmetric trends in the I_{DS} and PC_{DS} traces, one must consider the potential difference between the NWs and the wrap gate under positive and negative V_{DS}. For example, at $V_{GS} = 0.0$ V and a negative V_{DS} (with the source grounded and negative bias applied to the top ITO drain contact), an inward electric field leads to electron accumulation in the NWs, resulting in a substantial increase in drain-source current. Conversely, at $V_{GS} = 0.0$ V and a positive V_{DS}, the outward electric field depletes the NWs, reducing the current. In these devices, similar to the two-terminal devices, the low I_{DS} observed for positive V_{DS} indicates successful compensation of residual unintentional n-type doping during the growth of the nominally intrinsic i-segment, thereby significantly improving the phototransistor performance.

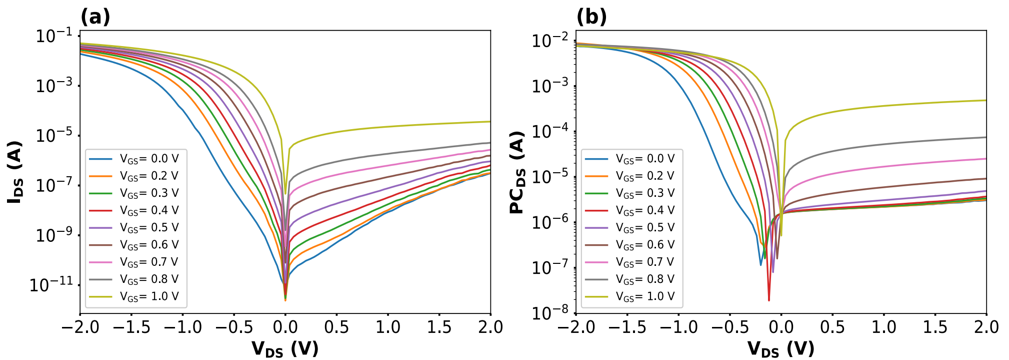

Figure 7.1: Phototransistor output characteristics a) in the dark and b) under illumination (after subtracting the dark current) for different V_{GS}.

7.2. Spectrally-resolved, bias-tunable responsivity

The spectrally-resolved PC_{DS} of the phototransistor was measured using FTIR PC spectroscopy for various applied V_{GS} (Fig. 7.2 (a)). To facilitate a comparison between different applied V_{GS}, the spectra were normalized to the peak PC_{DS} value. It is evident that there is a single onset at around 1.3 eV for $V_{GS} = 0.0$ V, attributed to the optical interband transition in the InP NWs. With increasing gate bias, new spectral features emerge around 0.7 eV and 1.15 eV. These new features are associated with optical interband transitions between the ground and first excited electron and heavy hole states in the InAsP QDiscs. The final excited electron state in the

QDiscs is close to the band edge of InP, allowing excited electrons to be thermally emitted to the conduction band of the InP NWs. The spectrally-resolved PC_{DS} was converted to spectrally-resolved responsivity, as shown in Fig. 7.2 (b) using NIST-calibrated Si (FDS100- CAL) and Ge (FDG03-CAL) photodiodes, purchased from Thorlabs.

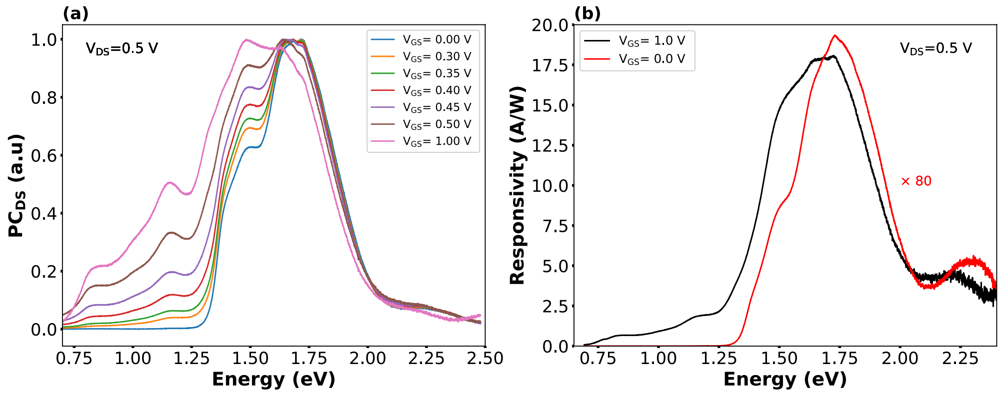

Figure 7.2: a) Spectrally-resolved PC_{DS} at different V_{GS}. The spectra have been normalized to a peak value of 1.0. b) Calibrated phototransistor responsivities at V_{GS} = 0.0 and 1.0 V, respectively, extracted from (a). The V_{GS} = 0.0 V trace has been multiplied by 80.

7.3. Modeling results and transistor characteristics

To comprehend the underlying physics governing the optoelectronic behavior of the current GAA-phototransistor, in-depth simulations of carrier transport dynamics have been conducted. These simulations utilized a radially symmetric 2D geometry of a single NW. Similar to the two-terminal photodetector, all simulations were performed using the commercial device simulator *Synopsys Sentaurus*, which solves the continuity equations for electrons and holes, incorporating drift-diffusion currents, along with the Poisson equation. The dimensions of the NW and also the thickness and composition of the QDiscs were determined from TEM and EDX investigations of the NWs. Key simulation parameters, such as doping profile of different segments, band offset between the InP NWs and InAsP QDiscs, Shockley-Read-Hall recombination lifetimes, densities, and energy positions of identified interface traps, were all derived from the analysis of the two-terminal photodetectors.

As explained in Chapter 5, we attribute the novel discovered photogating effect in the two-terminal photodetectors to acceptor-type NW/SiO_x interface traps located 140 and 190 meV below the conduction band edge. In the current GAA-phototransistors, the global gate contact surrounding the i-segment in each NW controls the electron concentration in the NW and governs the dynamic photocarrier interactions along with the trapped interface charges.

Figure 7.3 (a) displays the output characteristics of the phototransistor at V_{GS} = 0.0 V in both dark and illuminated conditions, revealing a good agreement between the experimental and the theoretical data, except for a discrepancy at higher V_{DS} attributed to the nonlinear leakage current through the wrap-gates, which was not considered in the simulations. In Fig. 7.3 (b), the calculated conduction band profile along the NW axis is depicted in both dark and illuminated states for V_{DS} = 0.5 V and two different gate biases: V_{GS} = 0.0 V and V_{GS} = 1.0 V, respectively. In the dark condition at V_{GS} = 0.0 V the NW experiences strong depletion (slightly

inverted to p-type) due to the GAA-contact, resulting in virtually no electric field across the i-segment of the NW, thus operating in a diffusion-driven subthreshold mode. The carrier dynamics can be further understood from the phototransistor transfer characteristics at $V_{DS} = 0.5$ V, as shown in Figure 7.3 (c). In the dark, a threshold bias of around 0.3 V is required to overcome the NW depletion. Figure 7.3 (d) illustrates the calculated positive charge on the ITO gate and the negative charge stored in the NW/SiO_x interface traps in the same gate area under both dark and illuminated conditions. At gate biases below 0.3 V, the interface trap states remain mostly empty and inactive (well above the Fermi level). By increasing the gate bias above 0.3 V, the phototransistor is successively biased into an on-state drift mode manifested by a strongly increased dark current and trapped interface charge. Figure 7.3 (b) demonstrates that at $V_{GS} = 1.0$ V, a substantial electric field along the NW is established, setting the phototransistor in a fully drift mode operation.

In Fig. 7.3 (b), the dashed and solid black lines illustrate the corresponding conduction band under illumination for both gate biases ($V_{GS} = 0.0$ V and $V_{GS} = 1.0$ V). In the subthreshold regime, the photocurrent PC_{DS} is governed by the photogating effect, where the photogenerated holes accumulate on the NW surface, shielding the gate and locking the quasi-Fermi level close to the conduction band. This results in an almost gate-independent PC_{DS} up to 0.6 V (Fig. 7.3 (c)). It is noteworthy that the subthreshold regime under illumination is dependent on the optical power and can be shifted to a lower gate bias by reducing the optical power. The exponential increase of PC_{DS} with V_{GS} above 0.6 V resembles phototransistor operation. This rise in PC_{DS} in the phototransistor mode is accompanied by an increase in the integrated trapped electron density (Fig. 7.3 (d)), effectively counteracting the gate control.

With the discussion above, the observed bias-tunable, spectrally-resolved PC_{DS} in Fig. 7.2 (a) becomes more comprehensible. In the subthreshold region (V_{GS} below 0.3 V), where there is no electric field along the i-segment of the NW, optically generated electron-hole pairs in the InAsP QDiscs and their associated InP barriers are primarily trapped in the QDiscs' potential, leading to minimal contribution to PC_{DS}. However, above $V_{GS} = 0.3$ V, an electric field is present, enabling the extraction of the photogenerated carriers in both the InP barriers and the InAsP QDiscs. The optical transitions in the QDiscs involve the ground state and first excited electron and heavy hole states in the QDiscs, which covers the spectral range of 0.7 to 1.6 eV. The excited carriers can then escape from the QDiscs' bound state into the InP continuum state via thermal emission, facilitated by various barrier-lowering mechanisms, such as the Poole-Frenkel effect and phonon-assisted tunneling [60], and subsequently be driven to the outer circuit by an applied electric field.

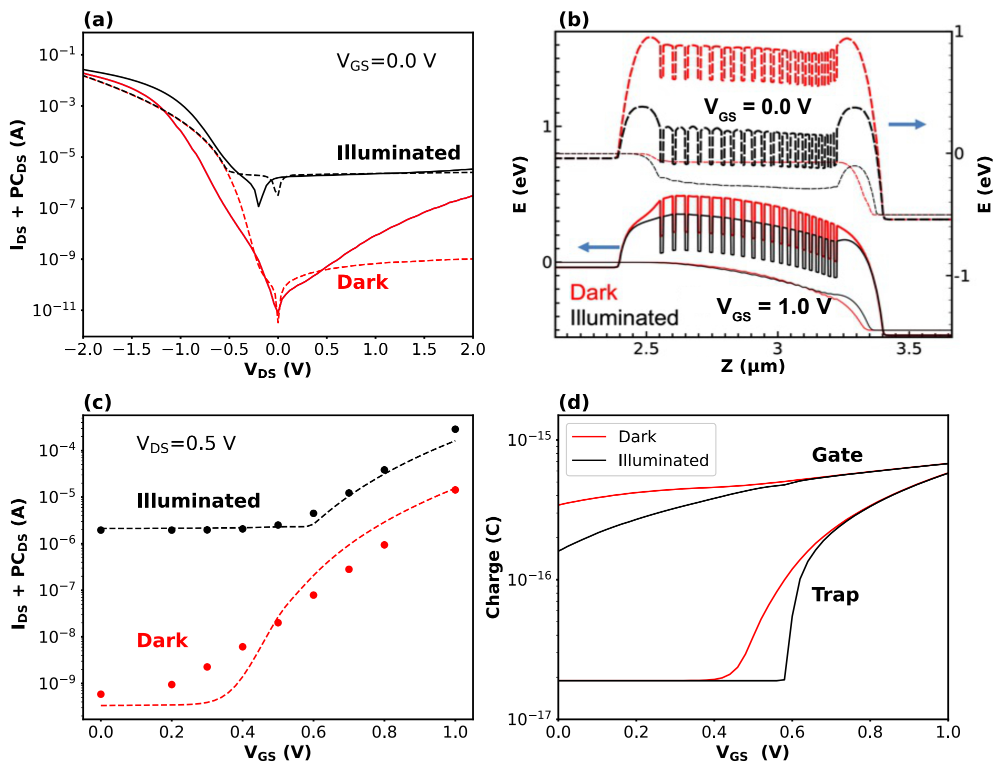

Figure 7.3: a) Phototransistor output (I_{DS} + PC_{DS}) characteristics at V_{GS} = 0.0 V. Solid and dashed lines are the experimental and simulated data, respectively. b) Conduction band profiles in the NW QDisc region along the NW for V_{DS} = 0.5 V. Top curves (dashed) for V_{GS} = 0.0 V, and bottom curves (solid) for V_{GS} = 1.0 V. The thin lines are the respective quasi-Fermi levels. c) Phototransistor transfer characteristics at V_{DS} = 0.5 V. The dots are experimental data, while the dashed lines are from simulations. d) Calculated positive gate charge and integrated (negative) interface electron density in the gate region versus V_{GS} in the dark and under illumination.

7.4. Time-response measurements

To be able to calculate the gain and bandwidth of the GAA-phototransistor, time-response measurements were carried out using a 638 nm laser diode (Cobolt 06-MLD) with a 10 Hz square wave at various optical powers. The recorded transient PC_{DS} with a constant V_{DS} =0.5 V and two gate biases of V_{GS} =0.2 V and V_{GS} =1.0 V are shown in Fig 7.4 (a) and (b), respectively. The gate biases were chosen in accordance with the mentioned diffusion and drift modes. The noticeable fast oscillatory behavior of the transient measurements is due to optical switching of the phototransistor from an off-state to an on-state, including charging various device capacitors. The zoomed-in parts of the time-resolved PC_{DS} measurement with a laser power of 3 mW are shown in Fig 7.4 (c) and (d) which correspond to the rise and fall time of 4 µs and 10 µs, respectively. Using Eq. 2.20, the bandwidths were calculated to be 350 kHz and 90 kHz for V_{GS} = 0.2 V and V_{GS} = 1.0 V, respectively. It should be mentioned here that the measured rise time and the bandwidth of the phototransistor is strongly influenced by the deployed current-voltage amplifier (Keithley 428), with a stipulated rise time of a few µs. The bandwidth of the phototransistor is also affected by the carrier dynamics including the interface traps. As discussed above, in the diffusion mode (low gate bias) the trap states are mainly empty and

inactive, leading to a fast photoresponse and higher bandwidth. On the other hand, in the drift mode (high gate bias), the traps are filled with electrons and the phototransistor is controlled by a combined effect of charges in the interface traps and on the gate. The photogating mechanism due to the trapped electrons in the interface states prolongs the transient time, resulting in a lower bandwidth.

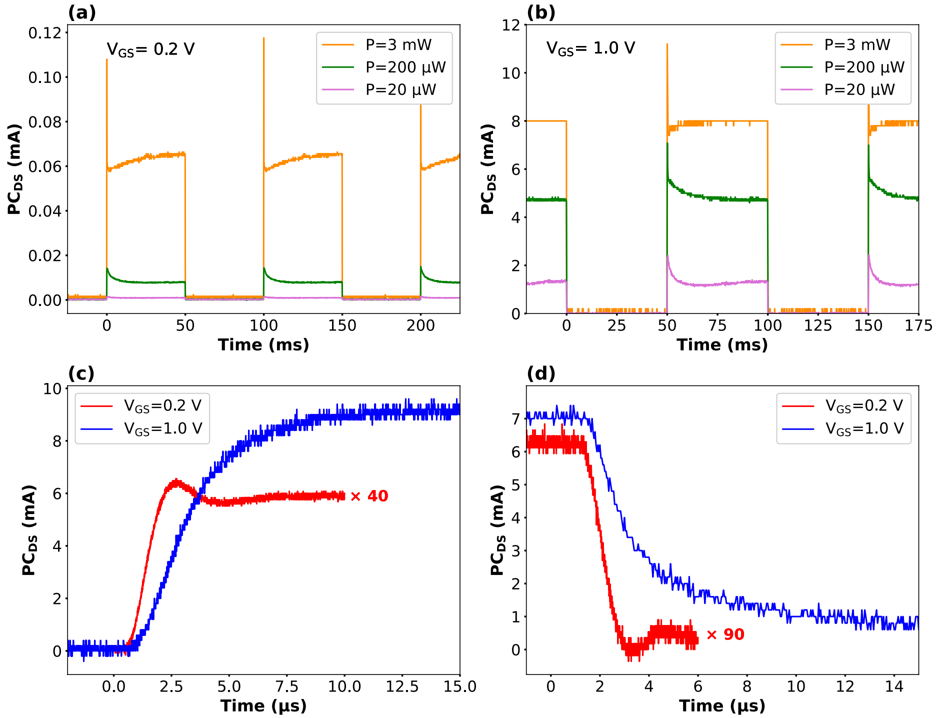

Figure 7.4: a) Transient PC_{DS} recorded at three different 638 nm laser powers with $V_{DS} = 0.5$ V and a) $V_{GS} = 0.2$ V and b) $V_{GS} = 1.0$ V, respectively. c) Rise and d) fall trends of the GAA-phototransistor under 3 mW laser excitation at $V_{DS} = 0.5$ V.

7.5. Power-dependence

Figure 7.5 (a) shows the power-dependent PC_{DS} measured at two different gate biases. At $V_{GS} = 0.2$ V, the PC_{DS} increases almost linearly with increasing laser power from 20 µW to 4 mW, while it shows a flat behavior at $V_{GS} = 1.0$ V. The responsivity was calculated from Eq. 2.17, while the gain was calculated from Eq. 2.19, assuming 100% internal quantum efficiency and a wavelength of 638 nm. The extracted responsivity and gain from the data in Fig. 7.5 (a) are shown in Fig. 7.5 (b).

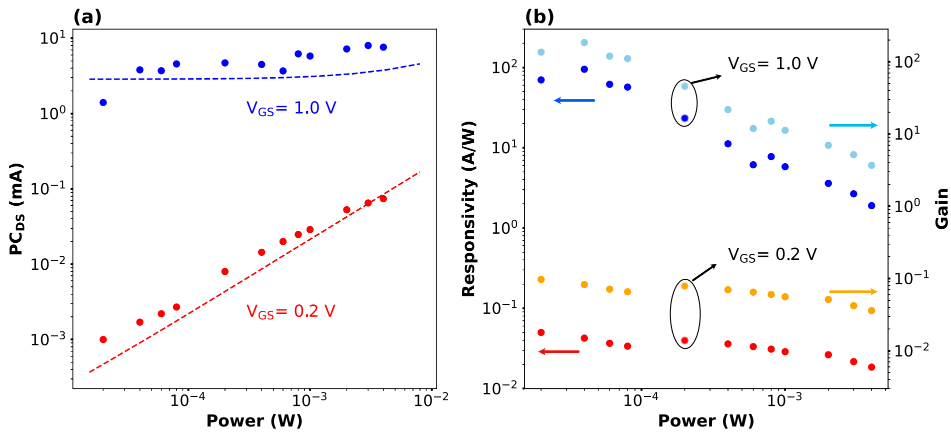

Figure 7.5: a) Dependence of PC_{DS} on optical power at $V_{DS} = 0.5$ V. The dashed colored traces are simulated data. b) Extracted responsivity (red/dark blue) and corresponding gain (orange/light blue) from (a). The upper (lower) sets of data are for $V_{GS} = 1.0$ V (0.2 V), as indicated in the figure.

An *NEP* of about 5 pW was extracted using a 638 nm laser and a chopper/lock-in amplifier setup, operating at 20 Hz. Considering the calculated *NEP* and Eq. 2.21, the specific detectivity was found to be $D^* = 2 \times 10^{10} \frac{(cm^2 Hz)^{1/2}}{W}$ at $V_{DS} = 0.5$ V and $V_{GS} = 1.0$ V.

8. Summary and outlook

In this thesis project, we developed and investigated two-and three-terminal broadband IR photodetectors based on millions of vertically standing InP NWs with 20 InAsP QDiscs embedded inside each NW. This was done in three different sub-projects presented below.

Investigation of novel photogating mechanism in two-terminal photodetectors
First, we did an in-depth investigation of the novel photogating effect in two-terminal NW photodetectors. From room-temperature optoelectronic characterization, combined with advanced theoretical modeling, two hitherto unknown acceptor-like traps were found at the NW/oxide interface. These traps act as the gate in a MOSFET where electrons can be trapped or released in dark and under illumination, resulting in a low dark current and very high gain/responsivity.

Realization and characterization of the first three-terminal NW array phototransistor.
In the second phase of this thesis work, we developed a three-terminal photodetector where a buried transparent wrap-gate around the NWs was added to the intricate structure. This facilitates a radial control of the carrier concentration in the NWs and QDiscs by more than two orders of magnitude. The transfer characteristics revealed two different transport regimes. In the subthreshold regime, the photodetector operates in a diffusion mode with a distinct spectral onset at the bandgap of InP. At larger gate biases, the phototransistor is set in a drift mode with a strong spectral contribution from the InAsP QDiscs. Besides the unexpected spectral tunability, the detector exhibits a state-of-the-art responsivity with a gain-bandwidth product of around one MHz. The experimental results for both detector types were in very good agreement with a real-device model.

Enhanced LWIR detection by photogating and ultra-thin ITO contacts
In the last phase we investigated the optical response of similar two-terminal photodetectors at low temperature. Spectrally-resolved measurements at 6 K, combined with theoretical calculations, revealed and elucidated the details around intriguing interband and intersubband signals involving discrete states in the embedded QDiscs. In particular we observed a fairly strong and quite narrow LWIR PC signal at around 0.135 eV (9.2 μm), originating from a transition between the ground state and first excited state in the QDiscs. In this work, we also developed the processing of ultra-thin top ITO contacts for significantly enhance LWIR transmission.

Summarized, this thesis work has been very exciting! The work has led to the development of a novel NW detector platform with high potential for realizing commercially viable competitive broadband photodetectors with electrically tunable photoresponse. There is still room for further investigations. For instance, what is the true nature of the trap states? Is it possible to tailor the trap state dynamics to remove the photogating effect for ultrafast response suitable for optical communication? Or optimize the photogating effect for maximum gain to realize detectors with single photon detection capability? How about developing semipersistent photoresponse for fabrication of optical synapses or artificial retinas, mimicking biological memory or vision functionality? Also, using an ultrathin buried ITO gate contact would further enhance the intersubband signal and possibly facilitate novel exciting research around bias-tunable electron-photon interactions in nanoscale systems.

References

1. Wook Shin, H.; Jun Lee, S.; Gun Kim, D.; Bae, M.-H.; Heo, J.; Jin Choi, K.; Jun Choi, W.; Choe, J.-w.; Cheol Shin, J., Short-wavelength infrared photodetector on Si employing strain-induced growth of very tall InAs nanowire arrays. *Scientific reports* **2015,** *5* (1), 1-8.

2. Han, N.; Wang, F.; Hou, J. J.; Yip, S. P.; Lin, H.; Xiu, F.; Fang, M.; Yang, Z.; Shi, X.; Dong, G., Tunable Electronic Transport Properties of Metal-Cluster-Decorated III–V Nanowire Transistors. *Advanced Materials* **2013,** *25* (32), 4445-4451.

3. Andrić, S.; Lindelöw, F.; Fhager, L. O.; Lind, E.; Wernersson, L.-E., Lateral III–V Nanowire MOSFETs in Low-Noise Amplifier Stages. *IEEE Transactions on Microwave Theory and Techniques* **2021,** *70* (2), 1284-1291.

4. Kilpi, O. P.; Hellenbrand, M.; Svensson, J.; Lind, E.; Wernersson, L. E., Vertical nanowire III–V MOSFETs with improved high-frequency gain. *Electronics Letters* **2020,** *56* (13), 669-671.

5. Wallentin, J.; Anttu, N.; Asoli, D.; Huffman, M.; Åberg, I.; Magnusson, M. H.; Siefer, G.; Fuss-Kailuweit, P.; Dimroth, F.; Witzigmann, B.; Xu, H. Q.; Samuelson, L.; Deppert, K.; Borgström, M., InP nanowire array solar cells achieving 13.8% efficiency by exceeding the ray optics limit. *Science* **2013,** *339* (6123), 1057-1060.

6. Tomioka, K.; Motohisa, J.; Hara, S.; Hiruma, K.; Fukui, T., GaAs/AlGaAs core multishell nanowire-based light-emitting diodes on Si. *Nano letters* **2010,** *10* (5), 1639-1644.

7. Zhang, H.; Wang, W.; Yip, S.; Li, D.; Li, F.; Lan, C.; Wang, F.; Liu, C.; Ho, J. C., Enhanced performance of near-infrared photodetectors based on InGaAs nanowires enabled by a two-step growth method. *Journal of Materials Chemistry C* **2020,** *8* (47), 17025-17033.

8. Ren, D.; Azizur-Rahman, K. M.; Rong, Z.; Juang, B.-C.; Somasundaram, S.; Shahili, M.; Farrell, A. C.; Williams, B. S.; Huffaker, D. L., Room-temperature midwavelength infrared InAsSb nanowire photodetector arrays with Al2O3 passivation. *Nano Letters* **2019,** *19* (5), 2793-2802.

9. Anyebe, E. A.; Sandall, I.; Jin, Z.; Sanchez, A. M.; Rajpalke, M. K.; Veal, T. D.; Cao, Y.; Li, H.; Harvey, R.; Zhuang, Q., Optimization of self-catalyzed InAs Nanowires on flexible graphite for photovoltaic infrared photodetectors. *Scientific Reports* **2017,** *7* (1), 1-9.

10. Karimi, M.; Jain, V.; Heurlin, M.; Nowzari, A.; Hussain, L.; Lindgren, D.; Stehr, J. E.; Buyanova, I. A.; Gustafsson, A.; Samuelson, L.; Borgström, M.; Pettersson, H., Room-temperature InP/InAsP quantum discs-in-nanowire infrared photodetectors. *Nano letters* **2017,** *17* (6), 3356-3362.

11. Karimi, M.; Heurlin, M.; Limpert, S.; Jain, V.; Zeng, X.; Geijselaers, I.; Nowzari, A.; Fu, Y.; Samuelson, L.; Linke, H.; Borgström, M.; Pettersson, H., Intersubband quantum disc-in-nanowire photodetectors with normal-incidence response in the long-wavelength infrared. *Nano letters* **2018,** *18* (1), 365-372.

12. Lahnemann, J.; Ajay, A.; Den Hertog, M. I.; Monroy, E.; Chou, S.; Lin, Y.; Tseng, P.; Tu, L.; Fortuna, F.; Zagonel, L.; Kociak, M.; Stephan, O., Near-infrared intersubband photodetection in GaN/AlN nanowires. *Nano letters* **2017,** *17* (11), 6954-6960.

13. Rigutti, L.; Tchernycheva, M.; Bugallo, A. D. L.; Jacopin, G.; Julien, F.; Songmuang, R.; Monroy, E.; Chou, S.; Lin, Y.; Tseng, P., GaN/AlN quantum disc single-nanowire photodetectors. *physica status solidi (a)* **2010,** *207* (6), 1323-1327.

14. Zeng, X.; Mourão, R. T.; Otnes, G.; Hultin, O.; Dagytė, V.; Heurlin, M.; Borgström, M. T., Electrical and optical evaluation of n-type doping in InxGa (1− x) P nanowires. *Nanotechnology* **2018,** *29* (25), 255701.

15. Wu, Q.; Liu, N.; Zhang, Y.; Qian, W.; Wang, X.; Hu, Z., Tuning the field emission properties of AlN nanocones by doping. *Journal of Materials Chemistry C* **2015,** *3* (5), 1113-1117.

16. Ojha, S. K.; Kasanaboina, P. K.; Lewis Reynolds Jr, C.; Rawdanowicz, T. A.; Liu, Y.; White, R. M.; Iyer, S., Incorporation of Be dopant in GaAs core and core–shell nanowires by molecular beam epitaxy. *Journal of Vacuum Science & Technology B, Nanotechnology and Microelectronics: Materials, Processing, Measurement, and Phenomena* **2016,** *34* (2), 02L114.

17. Hudait, M.; Modak, P.; Krupanidhi, S., Si incorporation and Burstein–Moss shift in n-type GaAs. *Materials Science and Engineering: B* **1999,** *60* (1), 1-11.

18. Arab, S.; Yao, M.; Zhou, C.; Daniel Dapkus, P.; Cronin, S. B., Doping concentration dependence of the photoluminescence spectra of n-type GaAs nanowires. *Applied Physics Letters* **2016,** *108* (18), 182106.

19. Lindgren, D.; Hultin, O.; Heurlin, M.; Storm, K.; Borgström, M. T.; Samuelson, L.; Gustafsson, A., Study of carrier concentration in single InP nanowires by luminescence and Hall measurements. *Nanotechnology* **2015,** *26* (4), 045705.

20. Kim, W.; Güniat, L.; Fontcuberta i Morral, A.; Piazza, V., Doping challenges and pathways to industrial scalability of III–V nanowire arrays. *Applied Physics Reviews* **2021,** *8* (1), 011304.

21. Sun, Z.; Hazut, O.; Huang, B.-C.; Chiu, Y.-P.; Chang, C.-S.; Yerushalmi, R.; Lauhon, L. J.; Seidman, D. N., Dopant diffusion and activation in silicon nanowires fabricated by ex situ doping: A correlative study via atom-probe tomography and scanning tunneling spectroscopy. *Nano letters* **2016,** *16* (7), 4490-4500.

22. Storm, K.; Nylund, G.; Borgström, M.; Wallentin, J.; Fasth, C.; Thelander, C.; Samuelson, L., Gate-induced Fermi level tuning in InP nanowires at efficiency close to the thermal limit. *Nano letters* **2011,** *11* (3), 1127-1130.

23. Jönsson, A.; Svensson, J.; Fiordaliso, E. M.; Lind, E.; Hellenbrand, M.; Wernersson, L.-E., Doping Profiles in Ultrathin Vertical VLS-Grown InAs Nanowire MOSFETs with High Performance. *ACS applied electronic materials* **2021,** *3* (12), 5240-5247.

24. Sharma, S. K.; Kumar, P.; Raj, B.; Raj, B., In1− xGaxAs double metal gate-stacking cylindrical nanowire MOSFET for highly sensitive photo detector. *Silicon* **2022,** *14* (7), 3535-3541.

25. Lü, W.-F.; Dai, L., Impact of work-function variation on analog figures-of-merits for high-k/metal-gate junctionless FinFET and gate-all-around nanowire MOSFET. *Microelectronics Journal* **2019,** *84*, 54-58.

26. Li, L.; Wang, D.; Zhang, D.; Ran, W.; Yan, Y.; Li, Z.; Wang, L.; Shen, G., Near-infrared light triggered self-powered mechano-optical communication system using wearable photodetector textile. *Advanced Functional Materials* **2021,** *31* (37), 2104782.

27. Li, Z.; Trendafilov, S.; Zhang, F.; Allen, M. S.; Allen, J. W.; Dev, S. U.; Pan, W.; Yu, Y.; Gao, Q.; Yuan, X., Broadband GaAsSb nanowire array photodetectors for filter-free multispectral imaging. *Nano Letters* **2021,** *21* (17), 7388-7395.

28. Liu, S.; Zhang, X.-d.; Gu, X.; Ming, D., Photodetectors based on two dimensional materials for biomedical application. *Biosensors and Bioelectronics* **2019,** *143*, 111617.

29. Schneider, H.; Liu, H. C., Quantum well infrared photodetectors. **2007**.

30. Rogalski, A., Quantum well photoconductors in infrared detector technology. *Journal of Applied Physics* **2003,** *93* (8), 4355-4391.

31. Wang, Y.; Gu, Y.; Cui, A.; Li, Q.; He, T.; Zhang, K.; Wang, Z.; Li, Z.; Zhang, Z.; Wu, P., Fast uncooled mid-wavelength infrared photodetectors with heterostructures of van der Waals on epitaxial HgCdTe. *Advanced Materials* **2022,** *34* (6), 2107772.

32. Ting, D. Z.; Soibel, A.; Höglund, L.; Nguyen, J.; Hill, C. J.; Khoshakhlagh, A.; Gunapala, S. D., Type-II superlattice infrared detectors. In *Semiconductors and Semimetals*, Elsevier: 2011; Vol. 84, pp 1-57.

33. Yang, H.; Zheng, Y.; Tang, Z.; Li, N.; Zhou, X.; Chen, P.; Wang, J., MBE growth of high performance very long wavelength InGaAs/GaAs quantum well infrared photodetectors. *Journal of Physics D: Applied Physics* **2020,** *53* (13), 135110.

34. Ren, A.; Yuan, L.; Xu, H.; Wu, J.; Wang, Z., Recent progress of III–V quantum dot infrared photodetectors on silicon. *Journal of Materials Chemistry C* **2019,** *7* (46), 14441-14453.

35. Hu, L.; Liao, Q.; Xu, Z.; Yuan, J.; Ke, Y.; Zhang, Y.; Zhang, W.; Wang, G. P.; Ruan, S.; Zeng, Y.-J.; Han, S.-T., Defect reconstruction triggered full-color photodetection in single nanowire phototransistor. *ACS Photonics* **2019,** *6* (4), 886-894.

36. Li, B.; Yan, X.; Zhang, X.; Luo, Y.; Lu, Q.; Ren, X., Controllable photoresponse behavior in a single InAs nanowire phototransistor. *Applied Physics Letters* **2017,** *111* (11), 113102.

37. Dhyani, V.; Jakhar, A.; Das, S., Diameter-dependent photoresponse with high internal gain in a back gated single Si nanowire phototransistor. *Journal of Physics D: Applied Physics* **2019,** *52* (42), 425103.

38. Chen, Y.; Sun, J.; Qiu, W.; Wang, X.; Liu, W.; Huang, Y.; Dai, G.; Yang, J.; Gao, Y., Deep-ultraviolet SnO2 nanowire phototransistors with an ultrahigh responsivity. *Applied Physics A* **2019,** *125* (10), 1-7.

39. Dutta, A., Fourier transform infrared spectroscopy. *Spectroscopic methods for nanomaterials characterization* **2017**, 73-93.

40. Rogalski, A., History of infrared detectors. *Opto-Electronics Review* **2012,** *20* (3), 279-308.

41. Photonics, R., RP Photonics Encyclopedia. *Chirp", Publication date unknown, Available online: http://www.rp-photonics.com/chirp.html* **2018**.

42. Ranganath, G., Black-body radiation. *Resonance* **2008,** *13* (2), 115-133.

43. Planck, M., *The theory of heat radiation*. Blakiston: 1914.

44. Sze, S. M., *Semiconductor devices: physics and technology*. John wiley & sons: 2008.

45. Pal, B.; Sarkar, K. J.; Banerji, P., Fabrication and studies on Si/InP core-shell nanowire based solar cell using etched Si nanowire arrays. *Solar Energy Materials and Solar Cells* **2020,** *204*, 110217.

46. Ho, J.; Tatebayashi, J.; Sergent, S.; Fong, C. F.; Ota, Y.; Iwamoto, S.; Arakawa, Y., A nanowire-based plasmonic quantum dot laser. *Nano letters* **2016,** *16* (4), 2845-2850.

47. Bao, Q.; Li, W.; Xu, P.; Zhang, M.; Dai, D.; Wang, P.; Guo, X.; Tong, L., On-chip single-mode CdS nanowire laser. *Light: Science & Applications* **2020,** *9* (1), 1-5.

48. Gu, Z.; Liu, S.; Sun, S.; Wang, K.; Lyu, Q.; Xiao, S.; Song, Q., Photon hopping and nanowire based hybrid plasmonic waveguide and ring-resonator. *Scientific reports* **2015,** *5* (1), 1-8.

49. Singh, R. R.; Singh, A.; Gautam, A.; Priye, V. In *Vertical silicon nanowire-based optical waveguide for DNA hybridization biosensor*, Quantum Sensing and Nano Electronics and Photonics XVI, SPIE: 2019; pp 308-314.

50. Pettersson, H.; Trägårdh, J.; Persson, A. I.; Landin, L.; Hessman, D.; Samuelson, L., Infrared photodetectors in heterostructure nanowires. *Nano Letters* **2006,** *6* (2), 229-232.

51. Sarkar, K.; Devi, P.; Kim, K.-H.; Kumar, P., III-V nanowire-based ultraviolet to terahertz photodetectors: Device strategies, recent developments, and future possibilities. *TrAC Trends in Analytical Chemistry* **2020,** *130*, 115989.

52. Hobbs, R. G.; Petkov, N.; Holmes, J. D., Semiconductor nanowire fabrication by bottom-up and top-down paradigms. *Chemistry of Materials* **2012,** *24* (11), 1975-1991.

53. Wolfsteller, A.; Geyer, N.; Nguyen-Duc, T.-K.; Kanungo, P. D.; Zakharov, N.; Reiche, M.; Erfurth, W.; Blumtritt, H.; Kalem, S.; Werner, P.; Gösele, P., Comparison of the top-down and bottom-up approach to fabricate nanowire-based silicon/germanium heterostructures. *Thin Solid Films* **2010,** *518* (9), 2555-2561.

54. Dick, K. A., A review of nanowire growth promoted by alloys and non-alloying elements with emphasis on Au-assisted III–V nanowires. *Progress in Crystal Growth and Characterization of Materials* **2008,** *54* (3-4), 138-173.

55. LaPierre, R.; Chia, A.; Gibson, S.; Haapamaki, C.; Boulanger, J.; Yee, R.; Kuyanov, P.; Zhang, J.; Tajik, N.; Jewell, N.; Rahman, K., III–V nanowire photovoltaics: review of design for high efficiency. *physica status solidi (RRL)–Rapid Research Letters* **2013,** *7* (10), 815-830.

56. Baskoutas, S.; Terzis, A. F., Size-dependent band gap of colloidal quantum dots. *Journal of applied physics* **2006,** *99* (1).

57. Arbiol, J.; De La Mata, M.; Eickhoff, M.; i Morral, A. F., Bandgap engineering in a nanowire: self-assembled 0, 1 and 2D quantum structures. *Materials today* **2013,** *16* (6), 213-219.

58. Rogalski, A.; Martyniuk, P.; Kopytko, M., Type-II superlattice photodetectors versus HgCdTe photodiodes. *Progress in Quantum Electronics* **2019,** *68*, 100228.

59. Rogalski, A., HgCdTe photodetectors. In *Mid-infrared Optoelectronics*, Elsevier: 2020; pp 235-335.

60. Katzenmeyer, A. M.; Léonard, F.; Talin, A. A.; Wong, P.-S.; Huffaker, D. L., Poole−Frenkel effect and phonon-assisted tunneling in GaAs nanowires. *Nano letters* **2010,** *10* (12), 4935-4938.

61. Razeghi, M., *Technology of quantum devices*. Springer: 2010.

62. Liu, H.; Gao, M.; McCaffrey, J.; Wasilewski, Z.; Fafard, S., Quantum dot infrared photodetectors. *Applied Physics Letters* **2001,** *78* (1), 79-81.

63. Coe-Sullivan, S., Quantum dot developments. *Nature Photonics* **2009,** *3* (6), 315-316.

64. Smith, D.; Mailhiot, C., Proposal for strained type II superlattice infrared detectors. *Journal of Applied Physics* **1987,** *62* (6), 2545-2548.

65. Kwan, D.; Kesaria, M.; Anyebe, E. A.; Huffaker, D., Recent trends in 8–14 μm type-II superlattice infrared detectors. *Infrared Physics & Technology* **2021,** *116*, 103756.

66. Guan, Y.; Cao, G.; Li, X., Single-nanowire silicon photodetectors with core-shell radial Schottky junction for self-powering application. *Applied Physics Letters* **2021,** *118* (15), 153904.

67. Spies, M.; Monroy, E., Nanowire photodetectors based on wurtzite semiconductor heterostructures. *Semiconductor Science and Technology* **2019,** *34* (5), 053002.

68. Wei, W.; Bao, X.-Y.; Soci, C.; Ding, Y.; Wang, Z.-L.; Wang, D., Direct heteroepitaxy of vertical InAs nanowires on Si substrates for broad band photovoltaics and photodetection. *Nano letters* **2009,** *9* (8), 2926-2934.

69. Li, Z.; He, Z.; Xi, C.; Zhang, F.; Huang, L.; Yu, Y.; Tan, H. H.; Jagadish, C.; Fu, L., Review on III–V semiconductor nanowire array infrared photodetectors. *Advanced Materials Technologies* **2023,** *8* (13), 2202126.

70. Li, Z.; Allen, J.; Allen, M.; Tan, H. H.; Jagadish, C.; Fu, L., Review on III-V semiconductor single nanowire-based room temperature infrared photodetectors. *Materials* **2020,** *13* (6), 1400.

71. González-Posada, F.; Songmuang, R.; Den Hertog, M.; Monroy, E., Room-temperature photodetection dynamics of single GaN nanowires. *Nano letters* **2012,** *12* (1), 172-176.

72. Zhang, X.; Liu, Q.; Liu, B.; Yang, W.; Li, J.; Niu, P.; Jiang, X., Giant UV photoresponse of a GaN nanowire photodetector through effective Pt nanoparticle coupling. *Journal of Materials Chemistry C* **2017,** *5* (17), 4319-4326.

73. Miao, J.; Hu, W.; Guo, N.; Lu, Z.; Zou, X.; Liao, L.; Shi, S.; Chen, P.; Fan, Z.; Ho, J. C., Single InAs nanowire room-temperature near-infrared photodetectors. *ACS nano* **2014,** *8* (4), 3628-3635.

74. Luo, T.; Liang, B.; Liu, Z.; Xie, X.; Lou, Z.; Shen, G., Single-GaSb-nanowire-based room temperature photodetectors with broad spectral response. *Science bulletin* **2015,** *60* (1), 101-108.

75. Tan, H.; Fan, C.; Ma, L.; Zhang, X.; Fan, P.; Yang, Y.; Hu, W.; Zhou, H.; Zhuang, X.; Zhu, X., Single-crystalline InGaAs nanowires for room-temperature high-performance near-infrared photodetectors. *Nano-micro letters* **2016,** *8*, 29-35.

76. LaPierre, R.; Robson, M.; Azizur-Rahman, K.; Kuyanov, P., A review of III–V nanowire infrared photodetectors and sensors. *Journal of Physics D: Applied Physics* **2017,** *50* (12), 123001.

77. Li, Z.; Azimi, Z.; Li, Z.; Yu, Y.; Huang, L.; Jin, W.; Tan, H. H.; Jagadish, C.; Wong-Leung, J.; Fu, L., InAs nanowire arrays for room-temperature ultra-broadband infrared photodetection. *Nanoscale* **2023,** *15* (23), 10033-10041.

78. Chiba, K.; Yoshida, A.; Tomioka, K.; Motohisa, J., Vertical InGaAs nanowire array photodiodes on Si. *ACS Photonics* **2019,** *6* (2), 260-264.

79. Ko, W. S.; Bhattacharya, I.; Tran, T.-T. D.; Ng, K. W.; Adair Gerke, S.; Chang-Hasnain, C., Ultrahigh responsivity-bandwidth product in a compact InP nanopillar phototransistor directly grown on silicon. *Scientific Reports* **2016,** *6* (1), 1-11.

80. Jie, J.; Zhang, W.; Jiang, Y.; Meng, X.; Li, Y.; Lee, S., Photoconductive characteristics of single-crystal CdS nanoribbons. *Nano letters* **2006,** *6* (9), 1887-1892.

81. Lopez-Sanchez, O.; Lembke, D.; Kayci, M.; Radenovic, A.; Kis, A., Ultrasensitive photodetectors based on monolayer MoS 2. *Nature nanotechnology* **2013,** *8* (7), 497-501.

82. Yin, Z.; Li, H.; Li, H.; Jiang, L.; Shi, Y.; Sun, Y.; Lu, G.; Zhang, Q.; Chen, X.; Zhang, H., Single-layer MoS2 phototransistors. *ACS nano* **2012,** *6* (1), 74-80.

83. Konstantatos, G.; Badioli, M.; Gaudreau, L.; Osmond, J.; Bernechea, M.; De Arquer, F.; Gatti, F.; Koppens, F. H., Hybrid graphene–quantum dot phototransistors with ultrahigh gain. *Nature nanotechnology* **2012,** *7* (6), 363-368.

84. Matsuo, N.; Ohno, H.; Hasegawa, H., Mechanism of high gain in GaAs photoconductive detectors under low excitation. *Japanese journal of applied physics* **1984,** *23* (5A), L299.

85. Munoz, E.; Monroy, E.; Garrido, J.; Izpura, I.; Sánchez, F.; Sánchez-Garcıa, M.; Calleja, E.; Beaumont, B.; Gibart, P., Photoconductor gain mechanisms in GaN ultraviolet detectors. *Applied physics letters* **1997,** *71* (7), 870-872.

86. Dan, Y.; Zhao, X.; Chen, K.; Mesli, A., A photoconductor intrinsically has no gain. *Acs Photonics* **2018,** *5* (10), 4111-4116.

87. Fang, H.; Hu, W., Photogating in low dimensional photodetectors. *Advanced science* **2017,** *4* (12), 1700323.

88. Coulon, P.-M.; Damilano, B.; Alloing, B.; Chausse, P.; Walde, S.; Enslin, J.; Armstrong, R.; Vézian, S.; Hagedorn, S.; Wernicke, T.; Massies, J.; Zuniga-Perez, J.; Weyers, M.; Michael, K.; Shields, P. A., Displacement Talbot lithography for nano-engineering of III-nitride materials. *Microsystems & Nanoengineering* **2019,** *5* (1), 52.

89. Bacsik, Z.; Mink, J.; Keresztury, G., FTIR spectroscopy of the atmosphere. I. Principles and methods. *Applied spectroscopy reviews* **2004,** *39* (3), 295-363.

90. Lee, C.-Y.; Wu, M.-C.; Shiao, H.-P.; Ho, W.-J., Temperature dependence of photoluminescence from InAsP/InP strained quantum well structures grown by metalorganic chemical vapor deposition. *Journal of crystal growth* **2000,** *208* (1-4), 137-144.

91. Larrabee, D.; Khodaparast, G.; Kono, J.; Ueda, K.; Nakajima, Y.; Nakai, M.; Sasa, S.; Inoue, M.; Kolokolov, K.; Li, J., Temperature dependence of intersubband transitions in InAs/AlSb quantum wells. *Applied Physics Letters* **2003,** *83* (19), 3936-3938.

92. Maier, T.; Schneider, H.; Liu, H.; Walther, M.; Koidl, P., Two-photon QWIPs for quadratic detection of weak mid-infrared laser pulses. *Infrared physics & technology* **2005,** *47* (1-2), 182-187.

Appendix

Table 1: Overview of processing steps for fabrication of two-terminal photoconductors.

<table>
<tr><th colspan="2">Consecutive processing steps</th><th>Description</th></tr>
<tr><td colspan="2">Atomic layer deposition (ALD)</td><td>30 nm SiO_x + 5 nm Al_2O_3</td></tr>
<tr><td colspan="2">Planarization</td><td>Spinning S1818 photoresist at 5000 rpm for 60 s followed by soft baking at 115 °C for 90 s</td></tr>
<tr><td colspan="2">Back etching of resist</td><td>RIE until the tip of the NWs are exposed</td></tr>
<tr><td colspan="2">Etching oxide / Au</td><td>26 s in BOE 1:10 followed by 26 s in gold etchant (KI/I_2), followed by rinsing in DI water and drying with N_2</td></tr>
<tr><td colspan="2">Deposition of new resist</td><td>Removing the old resist by acetone, rinsing in DI water, drying with N_2, spinning a new resist with the same recipe followed by RIE until the bare tips of the NWs are exposed</td></tr>
<tr><td colspan="2">Hard baking of resist</td><td>Placing the sample on a hot plate at room temperature, increasing the temperature to 200 °C and keeping it constant for 15 min</td></tr>
<tr><td colspan="2">Definition of device areas</td><td>• Spinning S1828 photoresist at 3500 rpm for 60 s
• Soft baking at 115 °C for 90 s
• UV exposure for 24 with a suitable mask
• 2 min development with MF 319
• Rinsing with DI water and drying with N_2</td></tr>
<tr><td colspan="2">Hard baking device areas</td><td>Placing the sample on a hot plate at room temperature, increasing the temperature to 200 °C and keeping it constant for 15 min</td></tr>
<tr><td colspan="2">Etching native oxide and sputtering the ITO top contact</td><td>• Stirring the sample in H_2SO_4 : H_2O (1:10) for 30 s, followed by rinsing in DI water for 1 min and drying with N_2
• Loading the sample immediately into the sputter and sputtering of 150 nm ITO which results in 30 nm sidewall around the tips of the NWs</td></tr>
<tr><td rowspan="2">Etching ITO from non-device areas</td><td>Covering device areas</td><td>• Spinning S1813 photoresist at 3000 rpm for 60 s
• Soft baking at 115 °C for 90 s
• UV exposure for 8 s with a suitable mask
• 2 min development in MF 319 followed by rinsing in DI water and drying with N_2</td></tr>
<tr><td>Etching</td><td>Stirring the sample in HCl : H2O 1:2 solution for 2 min followed by rinsing with DI water and drying with N_2</td></tr>
<tr><td colspan="2">Definition of bond pads</td><td>• Removing the resist from the previous step
• Spinning a layer of MaN 490 photoresist (6000 rpm for 60 s)
• Soft baking at 90 °C for 110 s
• 32 s UV exposure with a suitable mask
• Development in Ma-D 332S for 2 min, followed by rinsing in DI and drying with N_2
• Evaporation of 20 nm Ti and 400 Au, followed by overnight lift-off in acetone and rinsing with IPA</td></tr>
</table>

Table 2: Overview of processing steps for fabrication of three-terminal phototransistors.

Consecutive processing steps		Description
ALD		30 nm SiO_x + 5 nm Al_2O_3
Gate ITO	Resist spin coating	Spinning S1818 photoresist at 5000 rpm for 60 s followed by soft baking at 115 °C for 90 s
	Back etching of resist	RIE until just 600 nm of the NWs from bottom is covered by the resist
	Hard baking of resist	Placing the sample on a hot plate at room temperature, increasing the temperature to 200 °C and keeping it constant for 15 min.
	Definition of ITO gate contact	Sputtering of 150 nm ITO which results in 30 nm sidewall around the NWs
Etching gate ITO from top n-segments	Resist spin coating	Spinning S1818 photoresist at 5000 rpm for 60 s followed by soft baking at 115 °C for 90 s
	Back etching of resist	RIE until 600 nm of the NWs is exposed
	Etching ITO from NW tips	Stirring the sample slowly in an HCl : H_2O (1:2) solution for 20 s, followed by rinsing in DI water and drying with N_2
	Removing the old resist	Stirring the sample in acetone for 2 min., followed by rinsing in DI and drying with N_2
Device area definition and hard bake		• Spinning S1828 photoresist at 3500 rpm for 60 s • Soft baking at 115 °C for 90 s • UV exposure for 24 s with a suitable mask • 2 min. development in MF 319 followed by rinsing in DI water and drying with N_2 • Placing the sample on a hot plate at room temperature, increasing the temperature to 200 °C and keeping it constant for 15 min.
Etching the gate ITO from non-device areas	Covering the device areas	• Spinning S1813 photoresist at 3000 rpm for 60 s • Soft baking at 115 °C for 90 s • UV exposure for 8 s with a suitable mask • 2 min. development in MF 319 followed by rinsing in DI water and drying with N_2
	Etching	Stirring the sample in HCl : H_2O (1:2) solution for 4 min., followed by rinsing in DI water and drying with N_2
Removing the covering resist from device areas		Stirring the sample in acetone for 2 min. followed by rinsing in DI

<table>
<tr><td colspan="2">Etching the residual gate ITO, oxides and Au NPs</td><td>Spinning S1818 photoresist at 5000 rpm for 60 s followed by soft baking at 115 °C for 90 s
RIE until 600 nm of the NWs is exposed
Stirring the sample in H_2O (1:2) solution for 35 s, followed by stirring 25 s in BOE 1:10 and 25 s in gold etchant (KI/I_2)</td></tr>
<tr><td colspan="2">Deposition and hard baking of new resist</td><td>Removing the previous resist by acetone, rinsing in DI water, drying by N_2, spinning a new resist with same recipe followed by RIE until the tips of the NWs are exposed
Placing the sample on a hot plate at room temperature, increasing the temperature to 200 °C and keeping it constant for 15 min.</td></tr>
<tr><td colspan="2">Top contact ITO</td><td>Sputtering 150 nm ITO which results in 30 nm sidewall around the NWs</td></tr>
<tr><td rowspan="2">Etching the top ITO from non-device areas and one of the pads</td><td>Covering the device area with resist</td><td>Spinning S1813 photoresist at 3000 rpm for 60 s
Soft baking at 115 °C for 90 s
UV exposure for 8 s with a suitable mask
2 min. development with MF 319
Drying with N_2</td></tr>
<tr><td>Etching the top ITO from non-device areas</td><td>Stirring the sample in HCl : H_2O 1:2 solution for 2 min. followed by rinsing in DI water and drying with N_2</td></tr>
<tr><td colspan="2">Removing the covering resist from device areas</td><td>Stirring the sample in acetone for 2 min. followed by rinsing in DI.</td></tr>
<tr><td colspan="2">Formation of via hole</td><td>Spinning S1828 at 3000 rpm for 60 s
Soft baking at 115 °C for 90
A 50 s UV exposure using a suitable UVL mask
Development in MF319 for 2 min., followed by rinsing in DI water and drying with N_2
RIE to etch the hard-baked device areas until the gate ITO around the i-segments of the NWs buried in the pads are visible</td></tr>
<tr><td colspan="2">Definition of bond pads</td><td>Removing the resist from the previous step
Spinning a layer of MaN 490 photoresist (6000 rpm for 60 s)
32 s of UV exposure with a suitable mask
Development in Ma-D 332S for 2 min., followed by rinsing in DI and drying with N_2
Evaporation of 10 nm Ti and 400 Au, followed by overnight lift-off in acetone, rinsing with IPA and drying with N_2</td></tr>
</table>

Printed by Media-Tryck, Lund 2024 NORDIC SWAN ECOLABEL 3041 0903

InP/InAsP Quantum Discs-in-Nanowire Array Photodetectors

Imagine having eyes which can detect and see infrared light, similar to how some animals, such as snakes, can see in darkness by sensing heat. However, as we cannot see infrared light, we need specific detectors to capture and "see" those invisible waves. Historically, scientists have tried diverse ways to detect infrared light for different purposes like night vision, safety, and later for complicated technologies such as telecommunication. This thesis discusses the development of novel infrared light detectors comprising several millions of standing indium phosphide nanowires, connected in parallel as a single detector.

LUND UNIVERSITY

Division of Solid State Physics
Department of Physics
Faculty of Engineering

ISBN 978-91-8104-083-8